THERMAL BIMORPH MICRO-CANTILEVER BASED NANO-CALORIMETER FOR SENSING OF ENERGETIC MATERIALS

A Dissertation

by

SEOKWON KANG

Submitted to the Office of Graduate Studies of
Texas A&M University
in partial fulfillment of the requirements for the degree of

DOCTOR OF PHILOSOPHY

May 2012

Major Subject: Mechanical Engineering

Thermal Bimorph Micro-Cantilever Based Nano-Calorimeter for Sensing of Energetic Materials

THERMAL BIMORPH MICRO-CANTILEVER BASED NANO-CALORIMETER FOR SENSING OF ENERGETIC MATERIALS

A Dissertation

by

SEOKWON KANG

Submitted to the Office of Graduate Studies of
Texas A&M University
in partial fulfillment of the requirements for the degree of

DOCTOR OF PHILOSOPHY

Approved by:

Chair of Committee,	Debjyoti Banerjee
Committee Members,	Eric L. Petersen
	Molly M. Gentleman
	Victor M. Ugaz
Head of Department,	Jerald A. Caton

May 2012

Major Subject: Mechanical Engineering

ABSTRACT

Thermal Bimorph Micro-Cantilever Based Nano-Calorimeter for Sensing of Energetic Materials. (May 2012)

Seokwon Kang, B.S., Hanyang University;

M.S., Korea Advanced Institute of Science and Technology (KAIST)

Chair of Advisory Committee: Dr. Debjyoti Banerjee

The objective of this study is to develop a robust portable nano-calorimeter sensor for detection of energetic materials, primarily explosives, combustible materials and propellants. A micro-cantilever sensor array is actuated thermally using bi-morph structure consisting of gold (*Au: 400 nm*) and silicon nitride (Si_3N_4*: 600 nm*) thin film layers of sub-micron thickness. An array of micro-heaters is integrated with the microcantilevers at their base. On electrically activating the micro-heaters at different actuation currents the microcantilevers undergo thermo-mechanical deformation, due to differential coefficient of thermal expansion. This deformation is tracked by monitoring the reflected ray from a laser illuminating the individual microcantilevers (i.e., using the optical lever principle). In the presence of explosive vapors, the change in bending response of microcantilever is affected by the induced thermal stresses arising from temperature changes due to adsorption and combustion reactions (catalyzed by the gold surface). A parametric study was performed for investigating the optimum values by varying the thickness and length in parallel with the heater power since the sensor

sensitivity is enhanced by the optimum geometry as well as operating conditions for the sensor (e.g., temperature distribution within the microcantilever, power supply, concentration of the analyte, etc.). Also, for the geometry present in this study the nano-coatings of high thermal conductivity materials (e.g., Carbon Nanotubes: CNTs) over the microcantilever surface enables maximizing the thermally induced stress, which results in the enhancement of sensor sensitivity. For this purpose, CNTs are synthesized by post-growth method over the metal (e.g., Palladium Chloride: $PdCl_2$) catalyst arrays pre-deposited by Dip-Pen Nanolithography (DPN) technique. The threshold current for differential actuation of the microcantilevers is correlated with the catalytic activity of a particular explosive (combustible vapor) over the metal (*Au*) catalysts and the corresponding vapor pressure. Numerical modeling is also explored to study the variation of temperature, species concentration and deflection of individual microcantilevers as a function of actuation current. Joule-heating in the resistive heating elements was coupled with the gaseous combustion at the heated surface to obtain the temperature profile and therefore the deflection of a microcantilever by calculating the thermally induced stress and strain relationship. The sensitivity of the threshold current of the sensor that is used for the specific detection and identification of individual explosives samples - is predicted to depend on the chemical kinetics and the vapor pressure. The simulation results showed similar trends with the experimental results for monitoring the bending response of the microcantilever sensors to explosive vapors (e.g., Acetone and 2-Propanol) as a function of the actuation current.

DEDICATION

To my wife Jeong-Eun, my sweet angel Hailey and beloved parents for their endless support.

ACKNOWLEDGEMENTS

First of all, I would like to express my sincerest gratitude to my advisor, Dr. Debjyoti Banerjee, for providing me with an incredible opportunity to participate in interesting and meaningful research projects. Also, I am grateful for his efforts and time to offer an excellent research as well as important career advices.

I would like to thank my committee members, Dr. Eric L. Petersen, Dr. Molly M. Gentleman, and Dr. Victor M. Ugaz, for their guidance and support throughout the course of this research.

I would like to acknowledge the support from the Defense Advanced Projects Agency: Micro/Nano-Fluidics Fundamental Focus Center (DARPA-MF^3), Concentrated Solar Power (CSP) program from the Department of Energy (DOE), NanoMEMS Research LLC, NanoInk Inc., ADA Technologies Inc., and the Qatar National Research Foundation (QNRF).

Finally, thanks to my parents and my older brother for their encouragement and support throughout my lifetime, my wife for her patience and love, and my lab-mates Dr. Vijaykumar Sathyamurthi, Dr. Navdeep Singh, Dr. Saeil Jeon, Dr. Donghyun Shin, Dr. Seunghwan Jung, Mr. Byeongnam Jo, Mr. Jiwon Yu, Mr. Nicholas Niedbalski, and Mr. Scott W. Hansen for believing in me and being there for me whenever I needed. Special thanks to Dr. Anu Kaul at JPL, Dr. Juan Noveron, at UT-El Paso, and Mr. Hongjoo Yang for the CNTs synthesis experiments, Dr. Mary Amasia and Dr. Marc Madou at

UCI for the CD microfluidics thermal modeling as well as Mr. Mathew R. Lane for the explosive sensor development.

I am grateful to everyone who has helped me in some way or another throughout this entire duration.

NOMENCLATURE

Greek

Φ_v	Viscous dissipation [N/m^2-s]
α	Thermal diffusivity [m^2/s]
β	Temperature exponent
	Thermal expansion coefficient [K^{-1}]
γ	Surface energy [J/m^2]
δ_T	Thermal boundary layer [m]
ε	Lennard-Jones energy parameter [J/mol]
ε / k_b	Lennard-Jones energy [K]
μ	Dynamic viscosity [kg/m-s]
ν	Kinematic viscosity [m^2/s]
	Poisson's ratio
ρ	Density [kg/m^3]
	Electrical resistivity [Ωm]
σ	Hard-sphere collision diameter [$\AA$]
σ_f	Residual film stress [Pa]
σ_s	Surface stress [Pa]
ω	Driving frequency [Hz]

Uppercase

A	Area [m^2]
A_r (or A_s)	Pre-exponential factor [s^{-1}]
C	Molar concentration [mol/m^3 or mol/m^2]
D	Diffusion coefficient [m^2/s]
E	Young's modulus [Pa]
E_r (or E_s)	Activation energy [J/mol]
F	Driving force [N]
F_i	Initial feed of species i [mol]
G	Shear modulus [Pa]
Gr	Grashof number
H	Enthalpy [J/mol]
I	Applied current [A]
L	Characteristic length [m]
	Length of microcantilever [m]
M	Molecular weight [g/mol]
N_s	Number of species
Nu	Nusselt number
P	Perimeter of the surface [m]
Pr	Prandtl number
Q	Heat generation by electrical power [W]
	Quality factor

R	Ideal gas constant (8.3145 [$J/mol\text{-}K$] or 0.082051 [$atm/mol\text{-}K$])
	Rate of reaction [$mol/m^3\text{-}s$ or $mol/m^2\text{-}s$]
	Resistance [Ω]
	Tip radius [m]
Ra	Rayleigh number
S	Entropy [$J/mol\text{-}K$]
	Sensitivity [A^{-1}]
	Surface area [m^2]
T	Absolute temperature [K]
V	Molar volume [m^3/mol]
	Diffusional volumes
	Volume [m^3]
X	Conversion
Y	Mass fraction

Lowercase

b	Damping coefficient [$N\text{-}s/m$]
c_p	Specific heat [$J/kg\text{-}K$]
e	Euler-number (2.7183)
f	Tip-sample interaction force [N]
f_n	Natural frequency [Hz]
g	Acceleration due to gravity (9.81 [m/s^2])

h	Convective heat transfer coefficient [W/m^2-K]
	Planck constant (6.6256×10^{-34} [Js])
k	Rate constant [s^{-1}] for volumetric or surface reaction
	Stiffness [N/m]
	Thermal conductivity [W/m-K]
k_b	Boltzmann constant (1.38×10^{-23} [J/K])
l	Length of microcantilever [m]
m	Mass of microcantilever [kg]
n	Number of molecules
p	Pressure [Pa, atm, or $mmHg$]
q	Volumetric heat generation or heat flux [W/m^3]
r	Radius of dot [m]
t	Thickness of microcantilever [m]
	Time [sec]
v	Writing speed or velocity [m/s]
w	Width of microcantilever or line feature [m]
x	Distance [m]
y	Mole fraction
	Vertical location or Height [m]
z	Deflections in normal direction [m]

Sub- or superscripts

Au	Gold layer
L	Lateral
N	Normal (or flexural)
SiN	Silicon nitride layer
TS	Tip-sample interaction
c	Cantilever
i	i^{th} species or reaction
s	Substrate
	Surface
v	Volumetric
0	Initial
eff	Effective
eq	Equivalent

Acronyms

CFD	Computational Fluid Dynamics
CNTs	Carbon Nanotubes
CVD	Chemical Vapor Deposition
EDS	Energy Dispersive X-Ray Spectrometer
FEA	Finite Element Analysis
JPL	Jet Propulsion Laboratory

MWNTs	Multi-Walled Carbon Nanotubes
NASA	National Air and Space Agency
PECVD	Plasma-Enhanced Chemical Vapor Deposition
PVD	Physical Vapor Deposition
RH	Relative Humidity
SAM	Self-Assembly Molecules
SEM	Scanning Electron Microscopy
SWNTs	Single-Walled Carbon Nanotubes
VOCs	Volatile Organic Compounds

TABLE OF CONTENTS

CHAPTER Page

Page

LIST OF FIGURES

FIGURE Page

FIGURE Page

FIGURE Page

FIGURE Page

FIGURE Page

FIGURE Page

FIGURE Page

LIST OF TABLES

CHAPTER I

INTRODUCTION

A. General Concepts

1. Cantilever-Based Sensors

A sensor (or transducer) can be defined as "the primary element of a measuring chain which converts the input variable into a signal suitable for measurement" [1]. Generally it is an element which transforms energy from one form to a usable output (i.e. electronic signal). Various forms of energy are used in sensing applications, namely: mechanical, thermal, electrical, magnetic, radiant, chemical etc. In these sensing applications, the signals are mutually related by complex functional relationships. For instance, in this study the "thermal" energy generated by a "chemical" reaction is converted to the "mechanical" response (as shown in Figure 1). Hence, in these sensing platforms the stability and ease of measurement of the signals are of paramount importance.

Micro-cantilever based sensing platforms are considered attractive for their one dimensional bending response and their ease of analysis [2]. The development of microelectronics fabrication techniques has enabled the fabrication of miniaturized devices. These techniques were primarily developed for microfabrication of silicon-

---

This dissertation follows the style of ASME Journal of Heat Transfer.

based electronic devices such as transistors, diodes, and other circuit elements. However, the materials that are used in microelectronics, such as aluminum, silicon dioxide, silicon nitride, polycrystalline and crystalline silicon, also, possess outstanding mechanical properties [3]. Apart from these materials, polymers are frequently used for their high sensitivity to the temperature variations and low Young's modulus materials. However, polymer cantilevers have a major drawback such as less sensitivity to explosives (e.g., *~5 sec* for TNT at *0.2 ppb* concentration) [4].

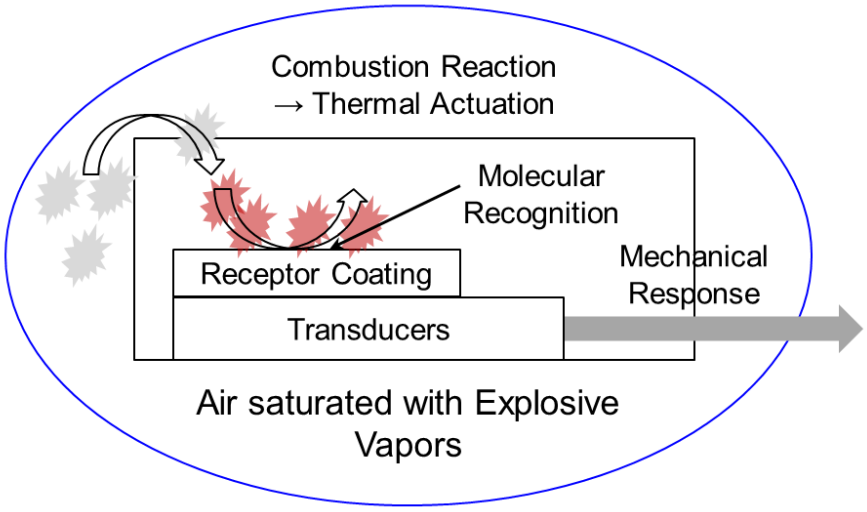

Fig. 1. Schematic representation of the sensing mechanism proposed in this study [5]*.

Also, many of these sensors require the integration with electrical power or the use of electrical signals for read-out. So, the usage as well as the application of micrometric mechanical structures (i.e. microcantilevers) has proliferated in the area of

* Reprinted with permission from "Cantilever Transducers as a Platform for Chemical and Biological Sensors" by N.V. Lavrik, M.J. Sepaniak, P.G. Datskos, 2004, *Rev. Sci. Instrum.*, 75(7), pp. 2229-2253, Copyright 2004 by American Institute of Physics.

Micro-Electro-Mechanical Systems (MEMS). Miniaturization of these sensors enables reduction in operating power consumption as well as high sensitivity (e.g., ~attogram sensitivity) [6]. In addition, the microcantilevers possess fast thermal actuation characteristics in contrast to that of macro-scale size devices.

Microcantilever-based sensors (or calorimeters) are highly sensitive to the transduction of physical or chemical or mechanical property based signals (i.e., nano-meter range), quantities (i.e., Pico-litter range), and have fast responses. Thus microcantilevers have been widely studied as chemical and biological sensors [2] in which static bending induced by differential surface stress or changes in resonant frequency upon mass uptake are monitored (as shown in Figure 2). Various examples of this type of sensing platform include:

- Surface stress: temperature changes (exothermic reactions), formation of Self-Assembled Monolayers (SAMs), DNA hybridization, Prostate Specific Antigen (PSA) concentration, etc. [5-27]
- Force at the apex: properties of biomolecules, DNA strands separation, *Van der Waals force*, etc. [28-30]
- Mass change: particles flux, PSA detection, etc. [31-36]

In general, the static bending is caused by either surface stresses or external force according to the above classifications. On the other hand, the resonance characteristics depend upon the mass change as well as viscoelastic properties of the medium

surrounding microcantilevers. Figure 2 depicts the transduction mechanisms for static and dynamic modes.

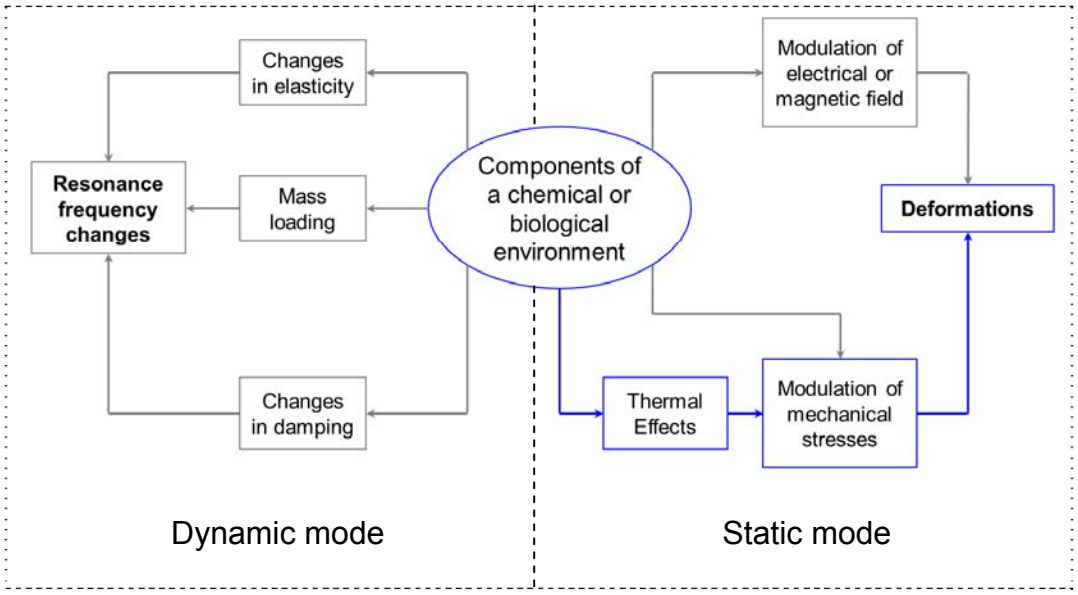

Fig. 2. Signal conversion mechanism in microcantilever-based transducers [5]*.

2. Readout Methods

One of the primary applications of micro-fabricated cantilevers is their use as scanning probes for Atomic Force Microscopy (AFM) to image the topography and the frictional properties of a surface through the measurement of changes in torsional and lateral deflections by friction [37]. In an AFM platform, the nano-scale deflections are typically monitored using the "optical detection (lever) method". This technology was

* Reprinted with permission from "Cantilever Transducers as a Platform for Chemical and Biological Sensors" by N.V. Lavrik, M.J. Sepaniak, P.G. Datskos, 2004, *Rev. Sci. Instrum.*, 75(7), pp. 2229-2253, Copyright 2004 by American Institute of Physics.

developed in 1988 [38]. This method is based on the detection of the change in position of a laser beam reflected by the free end of the cantilever. However, a drawback of this sensing platform is that it is not very robust (due to the requirement for continuous alignment of the laser beam). Hence, this requires a bulky optical setup which results in lack of portability, difficulties in miniaturization, and high manufacturing costs.

In an effort to eliminate the need for an optical system to enhance the sensitivity, alternative techniques include: piezoresistive [39-41], capacitive [31], piezoelectric [42], and polymeric [43-44] detection. These detection methods can be completely integrated into a chip, with the consequent advantages associated with size reduction. In addition, measurements are more stable with these sensors and using these methods. Also more robust devices can be obtained. Moreover, using integrated hardware based signal conditioning techniques the sensitivity of these sensor platforms can be enhanced.

3. Sensitivity

A careful choice of the beam dimensions has to be made in order to fabricate devices with the required resolution and sensitivity for each individual application. In general, the overall sensitivity is determined by the design sensitivity as well as the measurement sensitivity [45-46]. The Stoney equation [47] reveals the fundamentals of the surface stress-induced deflections in microcantilevers. In Stoney equation, as the length-to-width ratio increases, the clamping effects become less influential [48]. In

other words, the cantilever undergoes a rigid-body deformation away from the clamp, then the deflections (Δz) are strongly dependent on Poisson's ratio as follows:

$$\Delta z = \frac{4(1-\nu)\Delta\sigma_s}{E} \cdot \left(\frac{l}{t}\right)^2 \tag{1.1}$$

where ν is the Poisson's ratio, E is Young's modulus [Pa], $\Delta\sigma_s$ is the surface stress [Pa], t and l, are the thickness [m] and length [m] of microcantilever, respectively.

Hence, larger deflections can be achieved by reducing the bending stiffness (i.e., lowering the Young's modulus, increasing the length or decreasing the thickness). Also, the measurement sensitivity can be enhanced by improving the signal-to-noise ratio, which means the resonant frequency of the microcantilever should be made as high as possible. The resonant frequency (f_n) for a rectangular profile microcantilever is given by [49]:

$$f_n = \frac{1}{2\pi} \cdot \sqrt{\frac{E}{\rho}} \cdot \frac{t}{l^2} \tag{1.2}$$

where ρ is the mass density [kg/m^3] of the cantilever material. From equation (1.1) and equation (1.2), it is observed that any attempt to increase the deflections will decrease the resonant frequency. In other words, the mathematical expressions for the deflection and the resonant frequency display an inverse relationship [45-46]. Thus, the sensitivity is defined as:

$$\Delta z \cdot f_n = \frac{2(1-\nu)\Delta\sigma_s}{\pi\sqrt{E\rho}} \cdot \frac{1}{t} \tag{1.3}$$

B. Explosive Sensing

Explosive detection methods are classified into two groups: bulk explosives detection and trace explosives detection [50]. In bulk explosives detection method, physical or chemical properties of explosives are monitored remotely using various imaging techniques. On the other hand, the residues of explosives or a tiny amount of explosives can be detected by tracing the physical transport of vapor or particulates of explosives based on microfluidics or MEMS technologies [50-51].

Traditionally, in civilian and military operations, trained dogs are used to detect explosive materials. In military operations other trained animals/ insects (such as dolphins and bees) have also been used for explosives detection (in exotic environments such as in marine environments). To obviate practical issues concerning the usage of animals to detect explosives, automated procedures involving multiple types of electronic sensors ("electronic-nose" for air borne sensors and "electronic-tongue" for water based sensors) have been designed to replace the trained animals. Various electronic noses include the usage of fiber optics and beads, polymeric films, gold nanoclusters, surface acoustic waves (SAW), and micro-electromechanical systems (MEMS). In this study, micro-electromechanical systems were used as an electronic nose to detect explosives. Primarily, extensive experimental attention has been given to microcantilever-based explosives sensing applications in the past decade [4, 50-57]. This idea comes from the endeavor to mimic bomb-sniffing dogs, so we usually refer to the technology as electronic or artificial "noses". Ultimately, this technique provides very

fast and robust screening method for direct chemical identification of explosives in real time. An electronic nose is typically composed of an electrical power system, a chemical sensing system, and a response detection system.

C. Bimorph Micro-Cantilevers

1. Design Consideration

Proper estimate for the temperature profile of the microcantilever is a key factor in determining the response of the nano-calorimeter platform for chemo-mechanical sensing of explosives. The proposed numerical model is derived from the conservation of the energy fluxes. The energy fluxes arise from heat generation due to exothermic chemical reactions and heat loss by conduction-convection at the cantilever surface in the presence of explosive vapor mixture in air. To initiate the catalytic oxidation, the microcantilever surface is heated by joule heating using micro-heater that is integrated with the microcantilever at their base. In this study, both the catalytic surface (or heterogeneous) reaction on metal (i.e., *Au*) film as well as species transport by diffusion and gaseous (or homogeneous) reaction models are solved simultaneously. In particular, the *Au* catalysis enables ultra-lean oxidation. This means the sensor can be used to detect combustible vapor at very low concentrations (i.e. Pico-molar concentration) [58]. The reactants diffuse toward the catalyst surface and the highest value for the product concentration is at the surface (as shown in Figure 3). Accordingly, the products diffuse

away due to the concentration gradient [59]. The thermal response of microcantilevers caused by chemical reactions is determined by competing effects of chemical kinetics and thermal diffusion.

The dashed line in Figure 4 represents the heat loss in the absence of explosive vapor. Also, the curve of sigmoid shape shows the variation in heat generation due to catalytic oxidation, which is also a function of the catalyst temperature. The intersection point, T_{K1}, is the temperature change due to reactions on the surface at the steady-state. For a given concentration of reactants at this point on the microcantilever, the surface temperature is characterized by the kinetic-controlled regime (depending on the activation energy of catalytic surface reaction). The temperature of explosives and air mixture is initially at ambient temperature. Hence, to activate the volumetric reaction higher temperature is required (auto-ignition temperature). In other words, due to the fact that the activation energy of catalytic oxidation is lower than that of the homogeneous reaction (as shown in Figure 5) the oxidation (or combustion) reactions can be initiated at a lower energy (or temperature).

In Figure 4, an increase in the catalyst temperature due to higher actuation current (joule heating) causes a shift in the heat loss curve from T_{W1} to T_{W2} without causing any change in the slope since the heat transfer coefficient remains constant. However, if the cantilever is heated to a temperature exceeding T_{W2}, the heat generation curve is shifted above the heat loss curve (or line). In this region, the mixture of air and explosives flowing over the surface is heated by the heat generated from the surface reaction, and a gas phase reaction is also initiated. Eventually, the system is dominated

by the diffusion-controlled regime (via the transition state). The steady-state temperature value, T_{D2}, is determined by the catalytic surface as well as the gas-phase volumetric reactions.

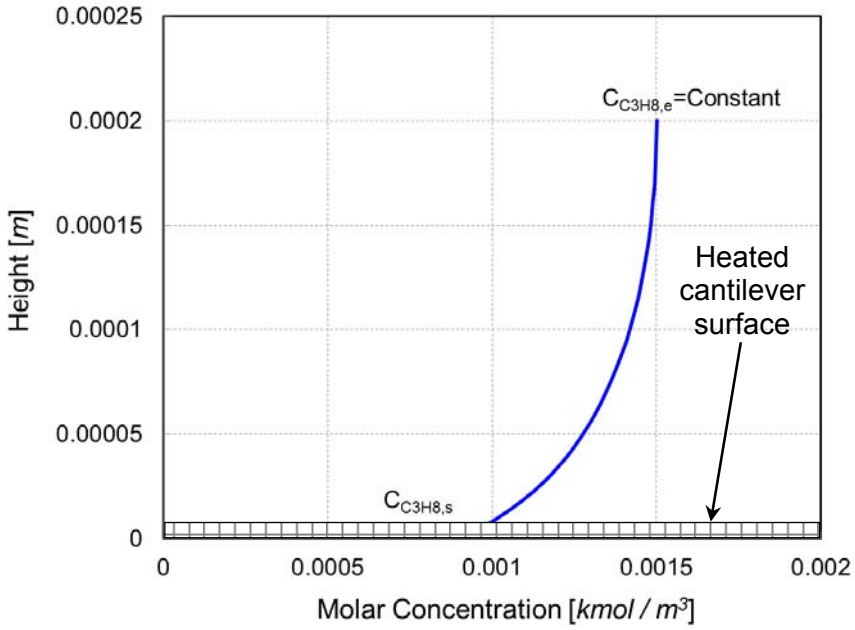

Fig. 3. Schematic of concentration profile over the heated microcantilever surface.

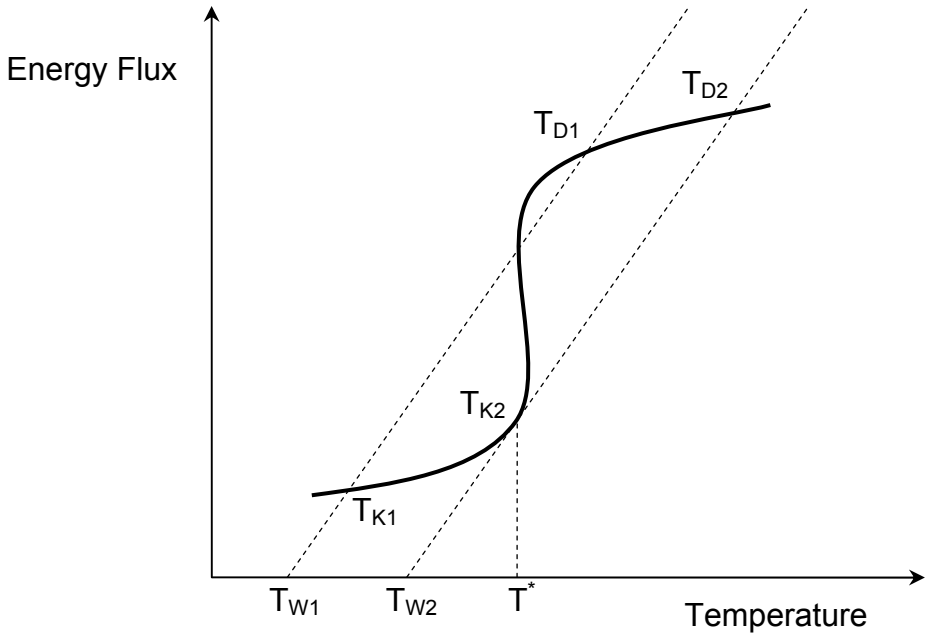

Fig. 4. Schematic representation of heat-generation (solid curve) and heat-loss (dashed line) for different initial catalyst temperatures [60][*].

[*] Reprinted with permission from "Catalytic Oxidation Studies with Platinum and Palladium" by A. Schwartz, L.L. Holbrook, H. Wise, 1971, *J. Catal.*, 21, pp. 199-207, Copyright 1971 by Elsevier.

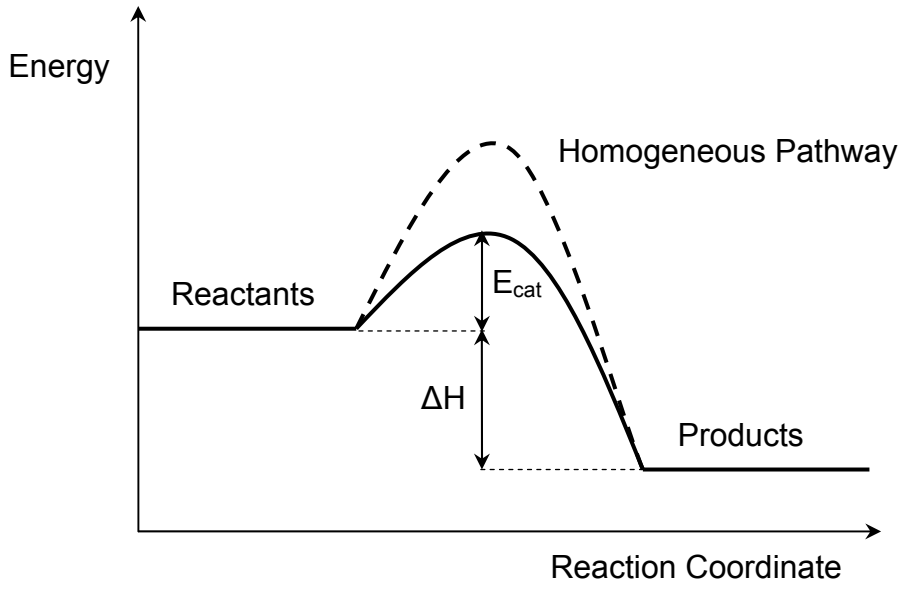

Fig. 5. Potential energy diagram for a catalytic reaction. The homogeneous reaction is shown for comparison [61].

As the first step, a 1D model is developed to provide a guideline for the design of the sensor when the vapor concentration is initially held at a constant value. For Cartesian coordinates, the molar form of the 1D species diffusion equation is [59]

$$D_{i,air}\frac{d^2C_i}{dx^2}+R_i=0 \tag{1.4}$$

where $D_{i,air}$ is the mass diffusion coefficient of species i in air [m^2/s], C_i is the molar concentration [mol/m^3], and R_i is the rate of reaction [mol/m^3-s]. For a first-order reaction that results in consumption of species i by gas-phase reaction, the rate of reaction is given by

$$R_i=-k_vC_i \tag{1.5}$$

Also, the binary mass diffusion coefficient in equation (1.4) is computed using equation (1.6) which is calculated by the relationships given by Fuller *et al.* [62]. The molecular diffusion coefficient for explosives diffusing in a mixture of explosives and air is given by:

$$D_{i,air} = \frac{1.013\times10^{-2}T^{1.75}\left[\frac{M_i + M_{air}}{M_i M_{air}}\right]^{0.5}}{p\left[V_i^{1/3} + V_{air}^{1/3}\right]^2} \tag{1.6}$$

where p is the pressure [Pa], T is the temperature [K], M *is* the molecular weight [g/mol], V are the diffusional volumes. The chemical kinetics, k_v, of each explosive are modeled based on 1st order homogeneous reactive flow proportional to the volumetric concentrations [mol/m^3] of species. Its mathematical expression is conventionally called as Arrhenius form which is of the following form:

$$k = A_r T^{\beta} \exp\left(-\frac{E_r}{RT}\right) \tag{1.7}$$

where A_r is the pre-exponential factor [s^{-1}], β is the temperature exponent, E_r is the activation energy [J/mol], and R is the universal gas constant (*8.3145 J/mol-K*). The chemical processes on the surface are treated by a procedure very similar to that for gas-phase reactions. The boundary conditions applicable to this system are:

$$\begin{aligned} C_i &= C_{i,0} \qquad \text{at } x = 0 \text{ (in gas)} \\ D_{i,air}\frac{dC_i}{dx} &= -k_s C_i \qquad \text{at } x = L \text{ (in catalyst)} \end{aligned} \tag{1.8}$$

where $C_{i,0}$ is the initial concentration of explosives in the control volume. If the evaporation occurs at a state of dynamic equilibrium, the initial concentration can be obtained from the vapor pressure of each explosive.

As opposed to homogenous reactions, catalytic oxidation by surface reaction depends on the surface coverage [mol/m^2] of explosives. The oxidation reactions of explosives are highly exothermic, which means the heat of reaction, ΔH, in Figure 5 has a negative value. In the kinetic-controlled region, the concentration of explosives over the surface is simply obtained as the general solution to the diffusion equation given in equation (1.4) as follows:

$$C_i(x) = C_1 e^{mx} + C_2 e^{-mx} \tag{1.9}$$

where

$$m = \left(k_v / D_{i,air}\right)^{1/2}, \quad C_1 = \frac{C_{i,0}\left(m - k_s / D_{i,air}\right)e^{-mL}}{2m\cosh\left(mL\right) + \left(2k_s / D_{i,air}\right)\sinh\left(mL\right)}, \text{ and } C_2 = C_{i,0} - C_1$$

In addition, the energy balance at the wall requires that at steady state the heat flux due to chemical reaction must be equal to the heat loss by convective and conductive heat transfer. Also, the heat flux by Joule heating as well as heterogeneous reaction is simultaneously imposed at the wall. Thus, the wall temperature can be calculated as:

$$T_{wall} = \frac{\Delta H \cdot D}{k} C_i + T_{wall,0} \tag{1.10}$$

Theoretically, a one-step global oxidation model can be considered as follows (i.e. *A*=Acetone, *B*=Oxygen, *C*=Carbon Dioxide, *D*=Water Vapor):

$$aA + bB \rightarrow cC + dD \tag{1.11}$$

In formulating the stoichiometric table, species *A* as is considered as the basis for the calculations (which is then divided through by the stoichiometric coefficient of *A*),

$$A + \frac{b}{a}B \rightarrow \frac{c}{a}C + \frac{d}{a}D \tag{1.12}$$

The volumetric concentration, C_i, of species *i* is defined as a function of the conversion, *X*. Neglecting pressure drop in the reaction (which is assumed to be isothermal), the concentration is obtained to be [63]:

$$C_i = \frac{F_i}{v} = C_{i,0}\left(\frac{1-X}{1+\varepsilon X}\right) \tag{1.13}$$

where

$$v = v_0\left(1+\varepsilon X\right) \tag{1.14}$$

$$C_{i,0} = y_{i,0}\left(\frac{p_0}{RT_0}\right) \tag{1.15}$$

where ε is the ratio between change in total number of moles for complete conversion and total number of moles in the control volume, which is given by

$$\varepsilon = y_{i,0}\delta \tag{1.16}$$

Also, the definition of δ and *F* are shown in Table I. The change in molar concentrations of species is calculated from stoichiometric relationships between reacting and produced molecules for a single oxidation reaction.

Table I. Stoichiometric table for complete oxidation.

Species	Initially	Change	Remaining
A	F_{A0}	$-F_{A0} \cdot X$	$F_A = F_{A0} \cdot (1 - X)$
B	$F_{B0} = \theta_B \cdot F_{A0}$	$-\frac{b}{a} F_{A0} \cdot X$	$F_A = F_{A0} \cdot \left(\theta_B - \frac{b}{a} X \right)$
C	0	$\frac{c}{a} F_{A0} \cdot X$	$F_C = \frac{c}{a} F_{A0} \cdot X$
D	0	$\frac{d}{a} F_{A0} \cdot X$	$F_D = \frac{d}{a} F_{A0} \cdot X$
Total	F_{T0}	-	$F_T = F_{T0} + \delta C_{A0} \cdot X$

$\theta_B = \frac{F_{B0}}{F_{A0}}$, $\delta = \frac{d}{a} + \frac{c}{a} - \frac{b}{a} - 1$

The simple static deformation model is applicable to thermally induced stresses and concomitant deformations of (thermal bimorph) microcantilevers made of two layered materials with different thermal expansion coefficients. Considerable effort has been devoted to analyzing the thermal stress at the surface of thermal bimorph structures [47, 64-68]. The first attempt to relate the film stress to the curvature of a bilayer film/substrate system was performed by Stoney [47] and this equation has been adopted extensively [64]. However, in these studies the film thickness was assumed to be infinitesimal (i.e., $t_{Au} << t_{Si_3N_4}$) compared to the substrate thickness. Recently, the accuracy of Stoney's equation was improved by including higher order terms of film

thickness in solutions [65-67]. The curvature and corresponding deflection for the bilayer microcantilever due to residual stress from heat treatment in fabrication process were also reported as [67]:

$$\Delta z = \frac{3L^2}{t_s + t_f}\left[\frac{\left(1+\frac{t_s}{t_f}\right)^2}{3\left(1+\frac{t_s}{t_f}\right)^2 + \left(1+\frac{t_s E_s}{t_f E_f}\right)\left(\frac{t_s^2}{t_f^2}+\frac{t_f E_f}{t_s E_s}\right)}\right]\left(\beta_s - \beta_f\right)\Delta T \qquad (1.17)$$

where L is the length of microcantilever [m], E is Young's modulus [Pa], t is the thickness [m], β is the coefficient of thermal expansion [K^{-1}] and the subscripts, s and f, denote the substrate and the film, respectively. Lee *et al.* [68] proposed a deflection model due to thermal stress distributions which do not require information about the modulus of the materials as:

$$\Delta z = \frac{\Delta T\left(\beta_f - \beta_s\right)\left(1 + t_f / t_s\right)L^2}{2\left(t_f + t_s\right)} \qquad (1.18)$$

Although the elastic deformation is only considered in this model, the differences from the predictions from this model when compared with the elastic-plastic FEA simulations are less than *10 %* [68]. Theoretical predictions from equation (1.17) and (1.18) are often used for obtaining quantitative analysis in order to determine the optimum geometry of the microcantilever and to explore the sensitivity for bending response.

2. Active Pen

The microcantilevers used in this study were procured from a commercial source (Active Pen™, Manufacturer: NanoInk Inc., Skokie, IL). The sensor array consists of six writer probes in the middle and two reader probes in the opposite end of the array. Figure 6 shows the schematic of a typical bimorph microcantilever and defines the geometrical parameters used in this study. Typically, each pen is *150 μm* long (*l*) and *1 μm* thick (*t*). The nominal width (*w*) of the reader probes is *30 μm* and of the writer probes is *40 μm*. Both writer and reader probes consist of two layers of materials – silicon nitride (Si_3N_4) substrate of *600 nm* thicknesses with a deposited gold layer of *400 nm* thickness on top.

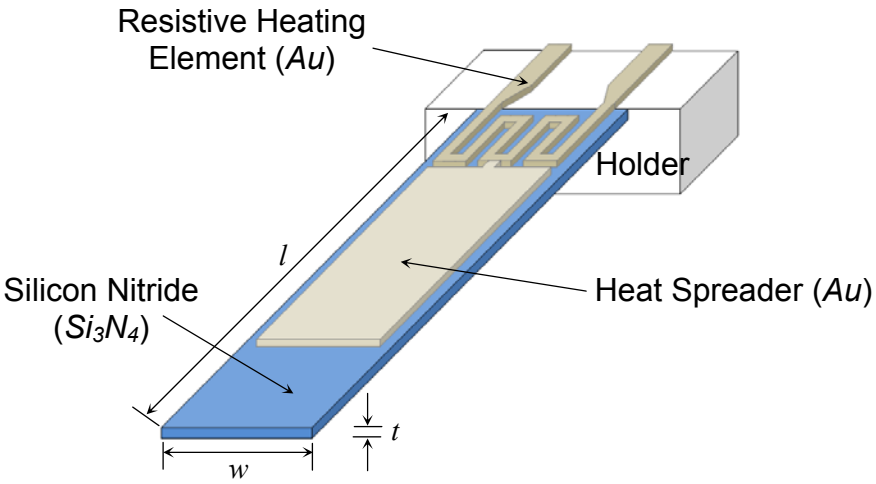

Fig. 6. Schematic of a bimetallic microcantilever used in this study (Nanoink™ Inc., *DS001*).

As shown in Figure 7, this product is fabricated by the thermal compression bonding at high temperature (*~300˚C*). The *Au* film is deposited on *Si* wafer by physical vapor deposition (PVD) at low pressure ($2\sim7\times10^{-7}$ *torr*). The Si_3N_4 microcantilevers are fabricated by patterning, etching and metallization on an oxidized *Si* wafer. In the process of thermal boding between two different metal layers, thermal stresses (i.e., residual stress) are induced. This causes the microcantilevers (bi-morph structrues) to acquire an irreversible initial deflection at room temperature. This factor should be considered in the design of microcantilever-based sensor system using the optical deflection method since it can affect the initial position of the reflected light spot.

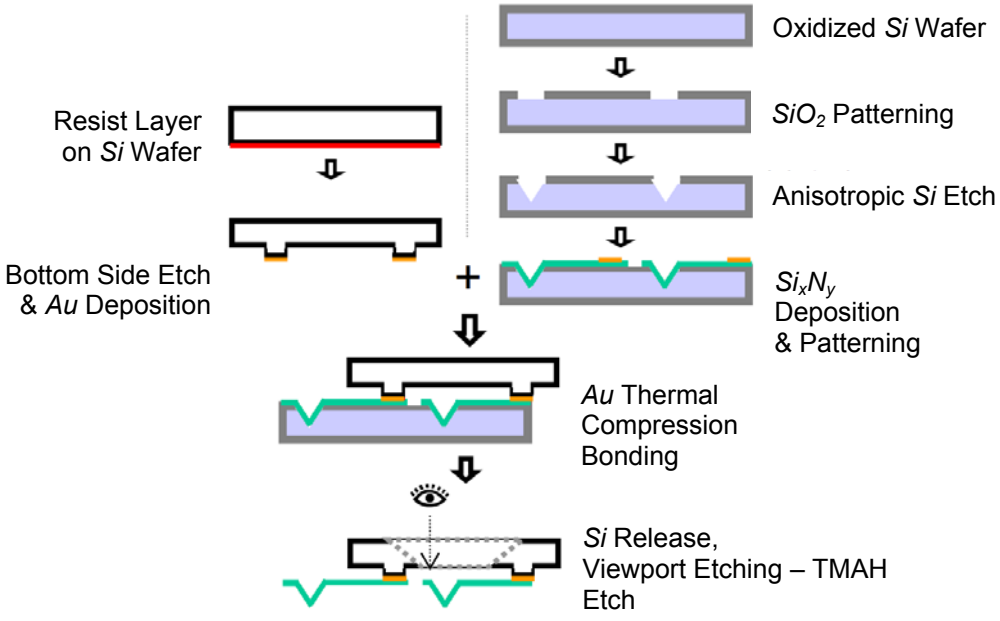

Fig. 7. Fabrication process of microcantilever array.

3. Residual Stress

Metal films can be deposited by sputtering, evaporation (PVD), electroplating, and chemical vapor deposition (CVD). During deposition processes, both the substrate and deposited film undergoes the heating and cooling cycles. Recrystallization and grain growth can occur when the temperature exceeds the elastic limit causing an irreversible deformation. This leads to the initial deflection [69]. In this case, the differential stress (or called as residual stress) is created due to dissimilar coefficients of thermal expansion of the Si_3N_4 substrate and *Au* film. Residual stress of multilayer systems is an important issue, since this sometimes results in cracking or interfacial rupture [69]. When the stress distribution through the thickness is not significant, the average residual film stress is calculated by [67]

$$\bar{\sigma}_f = \frac{1}{t_f}\int_0^{t_f} \sigma_f dz = \frac{E_s E_f t_s \left(E_s {t_s}^3 + E_f {t_f}^3\right)\left(\beta_s - \beta_f\right)\Delta T}{E_s^2 t_s^4 + E_f^2 t_f^4 + 2E_s E_f t_s t_f \left(2t_s^2 + 2t_f^2 + 3t_s t_f\right)} \tag{1.19}$$

where σ_f is defined as the mismatch between elastic stress (E) and thermal stress ($\beta\Delta T$).

4. Bending Characteristics Due to Thermal Actuation

a. Electro-Thermo-Mechanical Modeling

Various theoretical studies for the strain induced by thermal actuation have been reported [70-72]. In most theoretical models, the thickness effect and thermal resistance between layers are neglected and the strains at the interface of each the two adjacent

layers are assumed to be equal. In this study, to directly compare the results in terms of the actuation current, the electro-thermo-mechanical coupling model proposed by Jiang *et al.* [72] is adopted.

$$\Delta z = \frac{DA^{-1}C}{2 - DA^{-1}B} \times \frac{4L^4 I^2 R}{\sum_{i=1}^{2} k_i V_i \mu_1^4 \sinh(\mu_1)} \times \left[\mu_1^2 \sinh(\mu_1) - 16 \sinh\left(\frac{\mu_1}{2}\right) + 4\mu_1 - 4\mu_1 \cosh(\mu_1) + 8\sinh(\mu_1) \right] \tag{1.20a}$$

with

$$A = \begin{bmatrix} (E_1 A_1)^{-1} & (E_2 A_2)^{-1} \\ 1 & 1 \end{bmatrix}, \; B = \begin{bmatrix} t_1 & t_2 \end{bmatrix}^T, \tag{1.20b}$$

$$C = \begin{bmatrix} \alpha_2 - \alpha_1 & 0 \end{bmatrix}^T \text{ and } D = \frac{\begin{bmatrix} t_1/2 & (t_1 + t_2)/2 \end{bmatrix}}{(EI)_{eq}}$$

$$\beta_0 = \sqrt{\frac{1/a_1 + 1/a_2}{B_0}} \text{ where } a_i = \frac{\sum_{i=1}^{2} k_i V_i}{(V_1 + V_2) h_i} \tag{1.20c}$$

$$\mu_1 = 2L \sqrt{\beta_0^2 + \frac{hS}{\sum_{i=1}^{2} k_i V_i}} \tag{1.20d}$$

where I is the applied current [A], R is the resistance of heating element [Ω], V_i is the volume of ith layer [m^3], k_i is the thermal conductivity of ith layer [$W/m\text{-}K$] and S is the surface area [m^2]. Figure 8 represents the bending response due to electrical actuation and also by considering the initial deflection caused by the residual stress (calculated using equation (1.19)) for the actuation current value of *20 mA*.

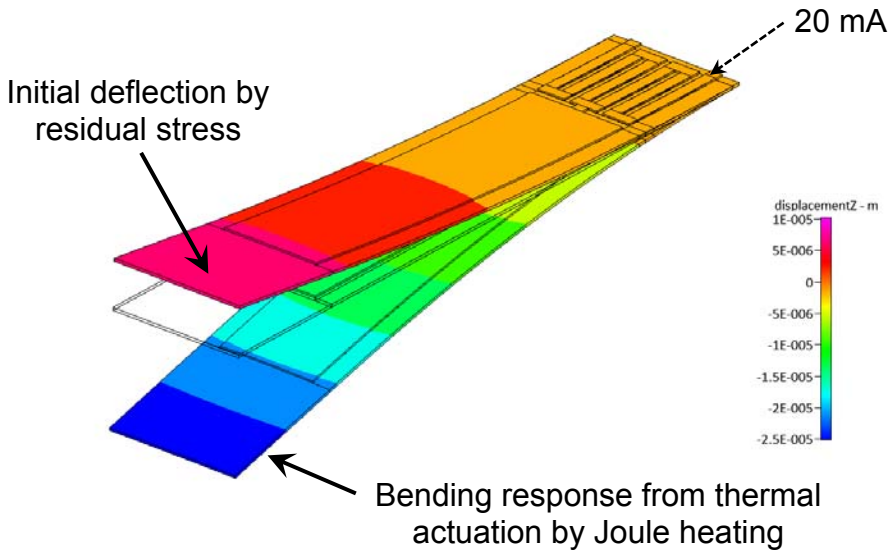

Fig. 8. Bending characteristics by electrically actuated microcantilever (Numerical Simulation by ESI CFD-ACE+®).

b. Numerical Modeling

The numerical techniques, such as finite differential method (FDM) or finite element method (FEM), are typically used for simulating the structural dynamics and for determining the response of microcantilevers. In this study, electro-thermo-structural coupling simulation is required for calculating the change in surface stresses resulting from thermal response that is caused by electrical actuation. For numerical simulations, Ansys® Multiphysics and ESI CFD-ACE+® based on FEM were used to calculate the deflection. The simulations were performed for three-dimensional FE models of the cantilevers under linear and static conditions. The FE models in Ansys® were meshed by *SOLID226* elements. The deflection due to residual stress conditions can be imposed initially using the "*INISTATE*" command, before performing the main calculations.

Deflection is calculated by static-structural simulations that are based on thermal data obtained from the results of electro-thermal coupling simulations. On the other hand, ESI CFD-ACE+® offers more straightforward environment to model multi-physics systems. Heat transfer, stress, grid deformation, and electric modules were selected for this case, while geometrical and material properties were identical to the numerical model implemented in Ansys®.

Basically, the material properties of metallic films are different than the bulk property values. The material properties used in this study are summarized in Table II. The heat supplied by the resistive heater is treated as a function of temperature due to temperature dependent resistivity of a gold heating element. It is difficult to estimate the convection heat transfer since Nusselt number correlations for natural convection are not available at this scale in the literature. In addition, the device may operate in pure conduction regime since the Rayleigh number may be less than the critical value required for natural convection. Thus, it is empirically determined that the best fit occurs at the effective value of $h = 700\ W/m^2\text{-}K$ [73]. Since the actuation slew rate is less than $10\ \mu s$ and actuation latency is less than $5\ ms$, therefore $4\ ms$ was selected as the total simulation time for the steady state simulation.

Table II. Material properties used in this study (Data was obtained from reports on thin metal film.) [73-79].

Property	Silicon Nitride (Si_3N_4)	Gold (Au)
Density [kg/m^3]	*3290*	*19320*
Thermal Conductivity [W/mK]	*1.7*	*150*
Thermal Expansion Coefficient [K^{-1}]	0.3×10^{-6}	14.6×10^{-6}
Elastic Properties E: Young's Modulus [GPa] / v: Poisson's Ratio	*224.6 / 0.253*	*74.5 / 0.35*
Electrical Resistivity [Ωm]	1×10^{10}	2.214×10^{-8}
Emissivity	*0.88*	*0.02*
Yield Strength [GPa]	*1.39*	*0.2*

c. Experimental Measurements

Generally, the change in deflection of the microcantilevers can be monitored by tracking the reflected light spot on the projection screen or position sensitive detectors (PSD) [38, 72]. This method requires a high resolution PSD and precise value of distance between the end of cantilever and the detector in order to determine the actual vertical movement of microcantilever tip for the variations in positions of reflected light spot that is recorded by the PSD. So, in this study, a method was adopted to visually

capture the dynamic motion caused by thermal actuation resulting from the electrical current recorded by the optical system. Figure 9 shows a schematic of the experimental setup that was used to measure the deflection of the reflected light from the microcantilevers. The combination of CCD camera (purchased from *IDS*^{TM}, Model: *uEye UI-1645LE*) and lenses (purchased from *Navitar*, Model: *12X UltraZoom and 2X adapter*) enabled the images to be recorded with a resolution of *~0.7 μm* per unit *pixel*. The deflection of microcantilever can also be measured by recording the pixel sizes using commercial image processing tool (e.g. *Photoshop*^{TM}).

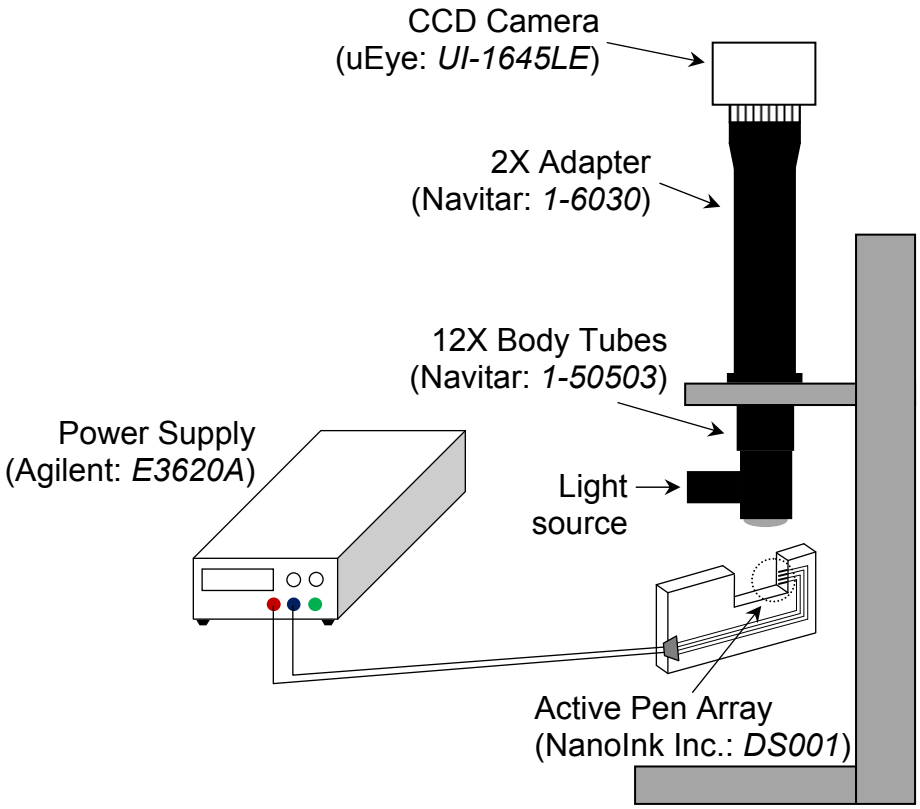

Fig. 9. Schematic setup of measurement experiment.

5. Design Optimization

The purpose of design optimization for the microcantilever-based sensor is to find the parameters that can result in larger deflections for a given surface stress as shown in equation (1.3). However, design parameters to obtain lager deflections can cause the degradation of signal-to-noise ratio due to reduction in natural frequency as mentioned in Chapter I. Typically, equation (1.1) and equation (1.2) can be applied to the case that the film thickness can be assumed to be infinitesimal compared to the substrate thickness. In this study, to evaluate the sensitivity of bimetallic microcantilever, the deflections are calculated using equation (1.17) and equation (1.21) used for the natural frequency calculation.

$$f_n = \frac{1}{2\pi} \cdot \sqrt{\frac{E_{eff}}{\rho_{eff}}} \cdot \frac{t}{l^2} \tag{1.21}$$

In equation (1.21), since the film thickness cannot be neglected, each layer (e.g., Si_3N_4 and Au) is assumed to be combined analytically into an equivalent single composite layer. As shown in Figure 10, the thickness of Si_3N_4 and Au layers are t_{SiN} and t_{Au}, and the width remains unchanged as the value of w.

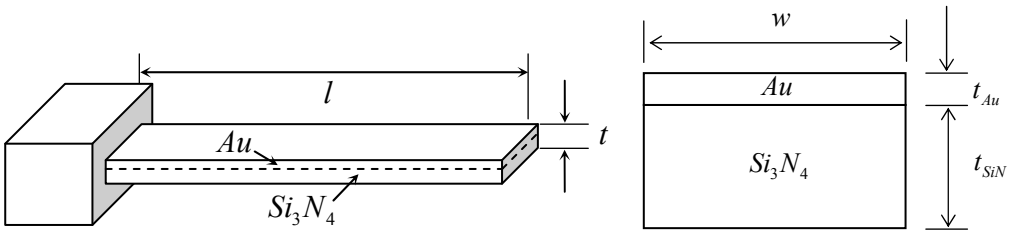

Fig. 10. Schematic representation and cross section of Si_3N_4/ Au composite beam.

The centroid location, y_{comp}, of the composite can be determined by:

$$y_{comp} = \frac{A_{SiN} \times y_{SiN} + A_{Au} \times y_{Au}}{A_{SiN} + A_{Au}} \tag{1.22}$$

where A_{SiN} and A_{Au} are the areas of the rectangular sections and y_{SiN} and y_{Au} are the locations of the centroids of the individual area. The composite section moment I_{comp} is:

$$I_{comp} = I_{SiN} + A_{SiN}(y_{comp} - y_{SiN})^2 + I_{Au} + A_{Au}(y_{comp} - y_{Au})^2 \tag{1.23}$$

where $I_{SiN} = (1/12)wt_{SiN}^3$ and $I_{Au} = (1/12)wt_{Au}^3$. Also, the effective Young's modulus of the composite, E_{eff}, based on total actual microcantilever thickness [67] is

$$E_{eff} = \frac{E_{Au}^2(\frac{t_{Au}}{t})^4 + E_{SiN}^2(\frac{t_{SiN}}{t})^4 + 2E_{Au}E_{SiN}\frac{t_{Au}}{t}\frac{t_{SiN}}{t}\left[2(\frac{t_{Au}}{t})^2 + 2(\frac{t_{SiN}}{t})^2 + 3\frac{t_{Au}}{t}\frac{t_{SiN}}{t}\right]}{E_{Au}\frac{t_{Au}}{t} + E_{SiN}\frac{t_{SiN}}{t}} \tag{1.24}$$

Also, the effective density of the composite is simply calculated by

$$\rho_{eff} = \frac{\rho_{SiN} \times t_{SiN} + \rho_{Au} \times t_{Au}}{t_{SiN} + t_{Au}} \tag{1.25}$$

The natural frequency of the bimetallic microcantilever was calculated by using equation (1.21) along with equations (1.24) and (1.25) and using the property values listed in Table II, and was estimated to be *25.5 kHz*. This result (1st flexural mode as shown in Figure 11(a)) differs from the numerical predictions (1st mode value in Table III) from Ansys® by *~24 %*. This is due to the unrealistic assumptions for the geometrical dimensions. Actual design of *Au* layer (e.g., micro heater and heat spreader) is more complex than the shape assumed for performing the theoretical calculation. The

simulated values listed in Table III represent in order each mode shape shown in Figure 11.

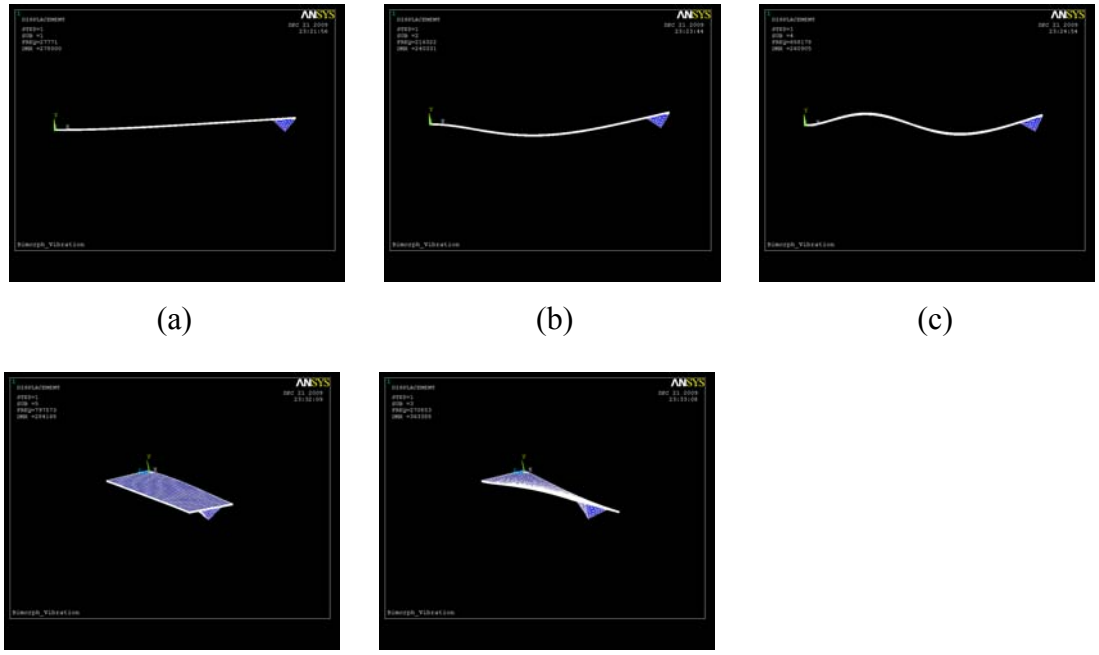

(a) (b) (c)

(d) (e)

Fig. 11. Vibration modes of cantilevers (a, b, and c) 1st, 2nd, and 3rd flexural, (d) lateral, and (e) torsional modes.

Table III. Natural frequency for first five modes of vibration obtained from the numerical analysis using Ansys®

Mode	*1*	*2*	*3*	*4*	*5*
Frequency [*kHz*]	*33.6*	*204.30*	*359.03*	*537.6*	*998.3*

The deflection and natural frequency contours, based on equation (1.17) and equation (1.21) respectively, involving the length and thickness of conventional microcantilever are plotted in Figure 12. This figure is plotted using Matlab®. It is evident that for any given thickness the deflection increases with the increase in cantilever length. Based on the definition of sensitivity given by equation (1.3), the optimum design space is given as the shaded area in Figure 12. The design of the microcantilever used for experimental testing is consistent with the optimum design derived in this study.

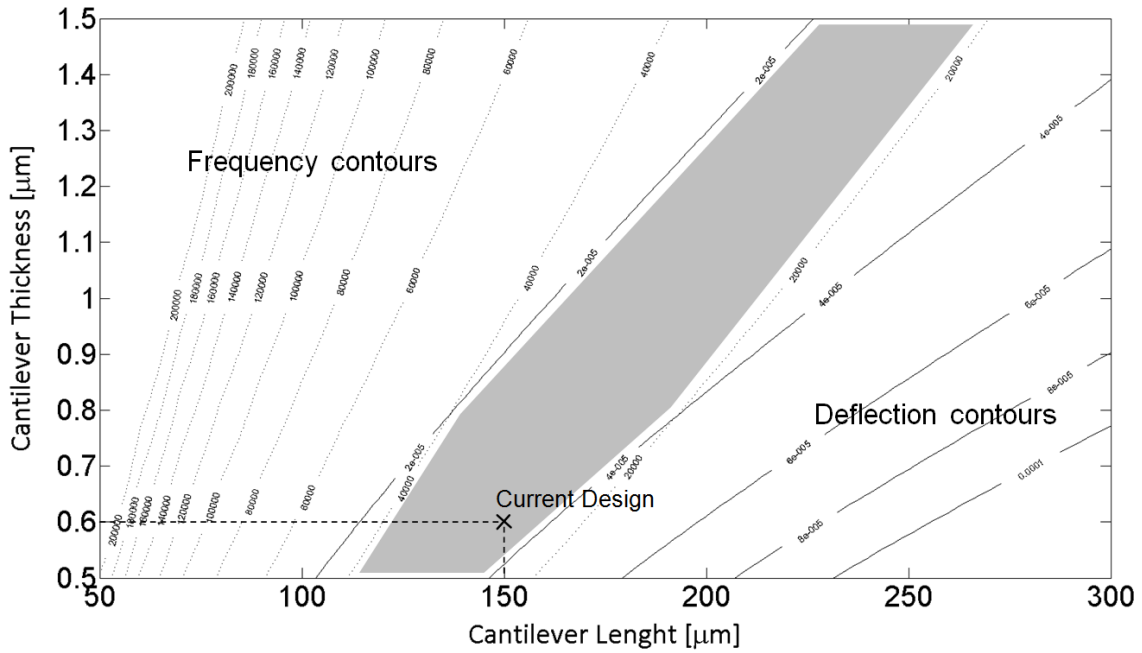

Fig. 12. Design optimization of the microcantilever for enhancing the sensitivity. The shaded area shows the optimum design space.

D. Objective and Scope of the Study

The fundamental transport mechanisms driving the chemo-mechanical transduction of microcantilever sensing platform for the detection of energetic materials (i.e., explosives, propellants and combustible materials) is the subject of this investigation. The exothermic reactions on the surface of a microcantilever causes the changes in surface stresses (i.e. compressive or tensile stresses), which is detected by the differential responses in either static mode of actuation or harmonic mode of actuation. The operation of the sensors is experimentally observed using the projection-screen method or the optical-detection method. For some volatile organic compounds (VOCs) gases (i.e. acetone and 2-propanol), the numerical analysis using commercial Computational Fluid Dynamics (CFD) and Finite Element Analysis (FEA) tools are performed to gain insights about the experimental measurements. The numerical analyses are conducted based on the following assumptions:

- In a gas-solid reaction, besides the exothermic reaction over the heated surface there exist another reaction mechanism (adsorption) by which reactants attach to the surface. However, since the forces of attraction between the gas molecules and the solid surfaces are weak, and the heat of adsorption is quite small (i.e. approximately *5 kcal*/*g-mol*), this process is neglected in this study.
- The diffusion (internal mass transfer) of reactants (or products) through pores of catalysts are neglected. The diffusion (external mass transfer) of reactants (or

products) from the ambient to the catalyst surface is the dominant transport mechanisms and is considered in this study.

- The final deflection due to thermal actuation occurs when the heat loss by convection from the heated surface is balanced by the heat generation by chemical reaction. So, the steady-state simulation results can be used to investigate the operation of the proposed sensor.

E. Overview

The scope of this investigation is limited to the development (i.e. design, fabrication, and characterization) of microcantilever-based sensors for detection of energetic materials.

The dissertation is divided into six chapters. Chapter I provides a general introduction to the basic concepts. This chapter also deals with the design, fabrication and characterization of microcantilevers to be used in the detection of explosive vapors. The principle of operation is based on the thermo-mechanical deformation of electro-thermally actuated microcantilevers (so-called bimetallic effects) caused by dissimilar coefficient of thermal expansion.

The methods for enhancing the sensitivity in thermally actuated MEMS devices are presented in Chapter II. At first, the theoretical approach using one-dimensional modeling is discussed. In addition, three experimental approaches for nano-coatings of

high thermal conductivity materials over the microcantilever surface are also investigated.

Results from numerical modeling using commercial CFD/FEA tools (i.e., Fluent® and Ansys®) are presented in Chapter III. Various parameters are discussed in this chapter – such as the estimation of differential values of deflections in response to external stimuli, thermo-chemical properties of explosives in gas-phase, as well as basic mechanisms that are used in this study such as conductive as well as convective heat transfer, chemical kinetics (i.e. homogeneous and heterogeneous reactions), and elastic deformation by thermal actuation.

Chapter IV deals with the experimental apparatus and procedure. The two detection techniques (i.e., manual projection-screen technique and automated optoelectronic detection technique) are described.

In Chapter V all the results obtained in this study (from numerical and experimental investigation as well as from analytical models) are presented and discussed. Additional results are provided in Appendices.

Finally, summary and conclusions are presented in the last chapter (Chapter VI). In the final chapter the summary of research achievements (the unique contributions from this study to the scientific/ technical literature) and the future directions for subsequent research topics are also explored.

The proposed study will contribute to the field of micro/ nano-scale heat and mass transfer as well as instrumentation of MEMS sensor in the following ways:

- Explore the characteristics of heat and mass transfer at micro/ nanoscale (e.g., estimate the equivalent convective heat transfer coefficient due to pure conduction during thermal actuation of MEMS devices).
- Investigate the robust recipe for nano-coatings of high thermal conductivity materials (e.g., Carbon Nanotubes) to enhance the sensitivity of thermally actuated MEMS-based transducers.
- Develop the multi-physics numerical model (i.e., electro-thermo-mechanical models coupled with thermo-chemical model for transport phenomena at the micro/ nano-scale). Implement the numerical models through the development of user-defined functions (UDF) in commercial numerical solver tools by coupling of computational fluid dynamics (CFD) technique with finite element analyses (FEA) techniques.
- Assess the impact of the experimental parameters on the thermo-mechanical actuation/ response of the microcantilever sensor, including: actuation current (or device temperature), thermo-chemical properties (such as chemical kinetics and enthalpy of reaction), thermo-physical properties (mass diffusivity, specified heat capacity, thermal conductivity, viscosity, etc.) and species concentration.
- Design experimental platforms and instrumentation systems for monitoring the micro/ nano-scale response of the sensor device for demonstrating the feasibility of the operating principle for a nano-calorimeter sensor based on thermal bi-morph actuation of a microcantilever array.

CHAPTER II

DIP-PEN NANOLITHOGRAPHY (DPN)

The sensor sensitivity for the fixed geometrical parameters can be maximized by enhancing the heat transfer from the microcantilever for enhancing the chemical reactions (i.e., by increasing the change in thermal surface stress $\Delta\sigma_s$ in equation 1.3). This can be achieved by enhancing the surface area as well as thermal conductivity of the substrates used for fabricating the microcantilevers. An efficient way to achieve these objectives can be the incorporation of nano-fins on the microcantilever surface. This can be achieved by application of nano-coatings with high thermal conductivity materials (e.g. Carbon Nanotubes, or " CNT") onto the micro-cantilever surfaces. An attractive approach for application of these nano-coatings is by using Dip-Pen Nanolithography (or " DPN").

A. Dip-Pen Nanolithography (DPN)

Dip-Pen Nanolithography (DPN) technique has been widely incorporated to deposit nano-scale chemical or biological patterns since it was invented by Chad Mirkin, Richard Piner, and Seunghun Hong at North Western University in 1999 (US Patent *6635311*). The nano-scale patterns are constructed via transport of molecules through the diffusion limited in small capillary meniscus (“capillary bridge”) when chemically coated scanning probe microscopy tips are very slowly moved in close proximity to a

substrate (as shown in Figure 13) [80-81]. The transport of ink molecules in DPN occurs due to the surface diffusion resulting from concentration gradient that occurs from the scanning probe tip to the surface via the capillary bridge. This method provides the nano-scale resolution (e.g., *~30-50 nm* features with *5 nm* spacing) as well as the ability to operate under ambient conditions (i.e., room temperature) [82]. Also, the unique benefit of DPN is the ability to deposit different molecules in parallel in close proximity as well as at different locations – either by single layer deposition or by multiple layers (or multiple passes) of deposition at the same location. Such an operation does not require any resist, stamp, and/or complicated fabrication processes (that are typically required in conventional photo-lithography). In addition, the operating cost is relatively cheap compared with E-Beam Lithography (EBL) or Deep UV Lithography (DUVL) since this technique can be implemented very simply on a conventional Scanning Probe Microscopy (SPM) platform.

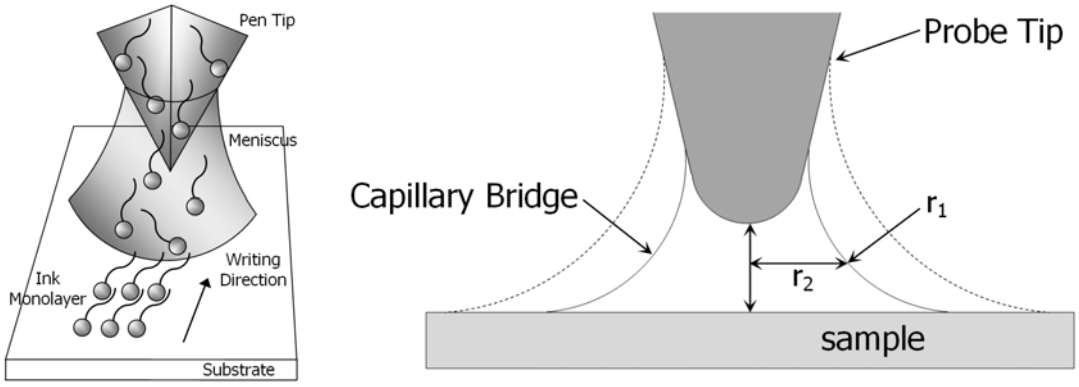

Fig. 13. Schematic of DPN "Ink" deposition (Ink molecules are transported onto the substrate through the meniscus bridge formed around tip) [83][*].

Various environmental conditions and parameters such as the surface diffusivity of the species, surface roughness of the substrate, ambient humidity, temperature, and the dwell time (or speed of writing) significantly affect the stable assembly of molecules during the DPN process [80-82]. The diffusion of molecules from the tip to the substrate occurs when the chemical affinity of molecules with the substrate is higher than that with the tip. Also, the surface roughness of substrate significantly affects the uniformity in self-diffusion of molecules over the substrate, which is related with formation of self-assembly molecules (SAM) in nano-scale.

In general, the transport of molecules can occur through the meniscus bridge formed at room temperature and under ambient conditions. Nevertheless, the relative humidity (RH) is a key factor to ensure the formation of the meniscus with appropriate

[*] Reprinted with permission from "Nanopatterning of Catalyst by Dip-Pen Nanolithography (DPN) for Synthesis of Carbon Nanotubes (CNT)" by S.-W. Kang, D. Banerjee, A.B. Kaul, K.G. Megerian, 2010, *Scanning*, 31(1), pp. 42-48, Copyright 2010 by John Wiley and Sons.

size for successful deposition [84-86]. The theoretical expression [85-86] of the curvature of a symmetrical meniscus in equilibrium is given by equation (2.1).

$$\left(\frac{1}{r_1}+\frac{1}{r_2}\right)^{-1} = r_k = \left(\frac{\gamma \cdot V}{RT \cdot \log\left(RH/100\right)}\right) \tag{2.1}$$

with $(\gamma V)/(RT) = 0.54\ nm$ for water at $20\ ^{\circ}C$; where r_k is the Kelvin radius [m], r_1 is the negative radius of the meniscus waist [m], r_2 is the negative half diameter of the meniscus at the waist [m], γ is the temperature dependent surface energy of water [J/m^2], V is the molar volume of water [m^3/mol], R is the molar gas constant [$J/mol\text{-}K$], and T is the absolute temperature [K]. Equation (2.1) reveals that the meniscus size increases by increasing RH [87]. As the meniscus size is augmented from solid line to dotted line in Figure 13, the transport of molecules becomes easier. Moreover, for inks containing large molecules, the specific value of RH can be a critical value for successful deposition.

As commonly expected, the longer contact time (t) enables larger feature size (or the radius of dot: r) [80-82, 88]. In a similar way, the thinner line (w) can be made by the faster writing speed (v). That is,

$$r \propto \sqrt{t} \quad \left(or \quad w \propto \frac{1}{\sqrt{v}}\right) \tag{2.2}$$

The experimental conditions for successful nano-patterning should be empirically determined according to different substrate-inks combinations.

Recently, the high throughput DPN platform (e.g., multi-pen configuration or integration with microfluidics) has been achieved by NanoInk Inc. – which is the outcome of the effort to commercialize DPN technology. Also, DPN technology has

been adapted and modified for purposes such as the use of different solvents (aqueous and non-aqueous) or in combination with different micro-fabrication techniques [80].

Typically, Type M (developed by NanoInk, Inc., Skokie, IL) probe enables long-time duration of patterning and multiple array generation. This probe contains 12 "A-frame" cantilevers combined with a hydrophilic microchannel in its body as shown in Figure 14(a). For the optimization for increasing loading of material and extend printing times, the numerical analysis using the VOF (Volume-of-fluids) method for the microfluidic ink delivery used to coat pen tips with ink materials was performed in this study.

The meniscus position in ink coating process is simulated by using a commercial CFD tool (or Fluent®). In the VOF method, the Navier-Stokes equations are discretized using second order schemes with the second order up-winding method. The segregated solver is applied with the PISO pressure correction method. The 3D model (as shown in Figure 14(b)) involving a square cross section is generated in Gambit®. The time step size and maximum iterations per time step in this transient simulation was 10^{-8} *sec* and *200*, respectively. Also, the boundary conditions are described in Figure 14(c). In boundary conditions for liquid-solid interface, the contact angles for both hydrophilic and hydrophobic surfaces are static values measured when using water as the ink solution.

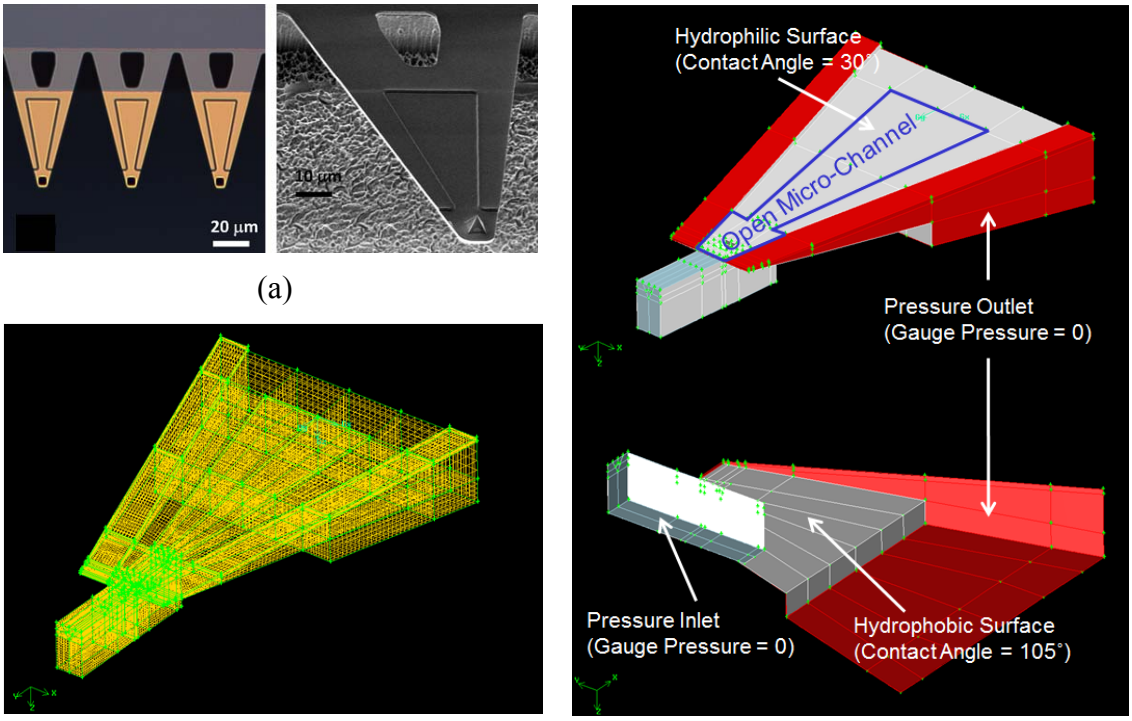

Fig. 14. Type M multi-pen array and solid model for numerical analysis (a) Geometry (b) Isometric-view of meshed numerical model (total number of grids = *71,929*) (c) Boundary conditions.

The pen tip is dipped into inkwell filled with ink solution for the inks delivery to the microchannel integrated inside the microcantilever. The microcantilever is tilted by an angle (α = *7*° in Figure 15(a)) with respect to the top surface of inkwell. Figure 15(b) shows the phase plot to show the movement of meniscus. At first, the flow goes up along to the hydrophilic surface of the pyramid pen tip. And then, the filling occurs by spreading toward the open micro-channel.

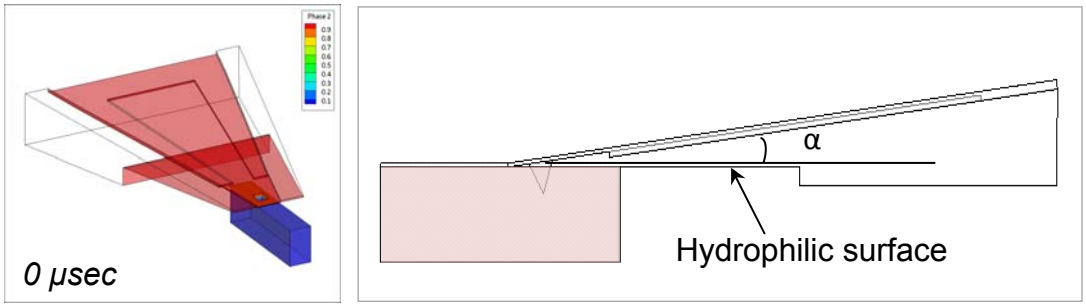

(a)

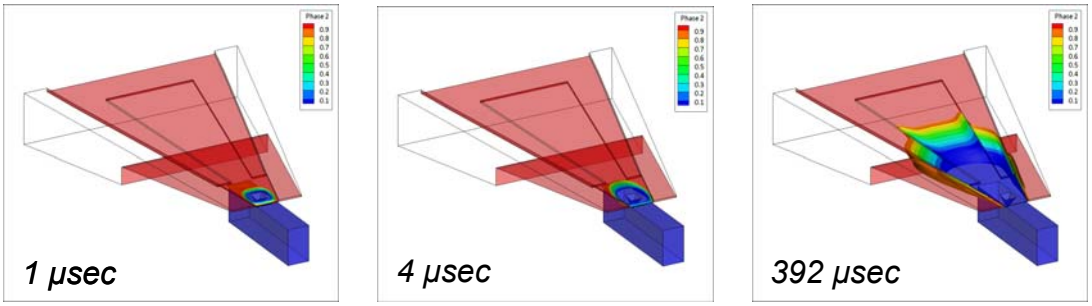

(b)

Fig. 15. Transient simulation results for inks delivery in pen coating process (a) Initial dipping (b) Phase plot (Blue: VOF = *1* (Solution) and Red: VOF = *0* (Air)).

From the simulation results shown in Figure 16, the meniscus is not separated from the hydrophobic surface. After the end of the hydrophobic area over the inkwell, the filling speed slows down considerably. That is, tip coating can be controlled by the overlapped area between cantilever and hydrophobic surface area below. So, the modification of configuration between pen and inkwell is proposed in this study. As the meniscus is approaching to the end of hydrophobic are over the inkwell, the modified design shows better filling phenomenon (as shown in Figure 16).

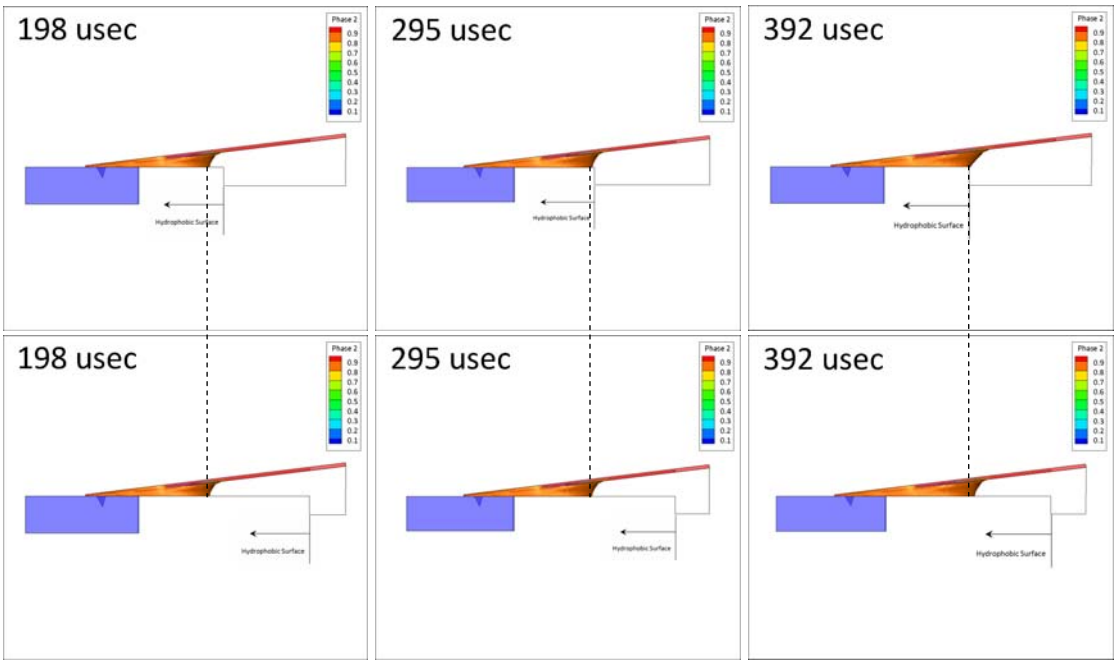

Fig. 16. Comparison of meniscus position in inks coating process – (Top) The filling is almost stopped (Bottom) The filling is still going on.

Numerical analysis for depositions can be achieved by multiple-steps from the initial filling of the microchannel in cantilever to diffusion through the meniscus bridge formed between tip and sample. Figure 17 represents the detail steps for the deposition simulation. In real physical phenomenon, the pen is extracted by moving upward to remove the pen from the inkwell, which can be simulated by moving boundary conditions along with automatic mesh adaptation. However, since the shape of the tip is pyramid, it is not easy to find the adaption formula to prevent the divergence of the simulation.

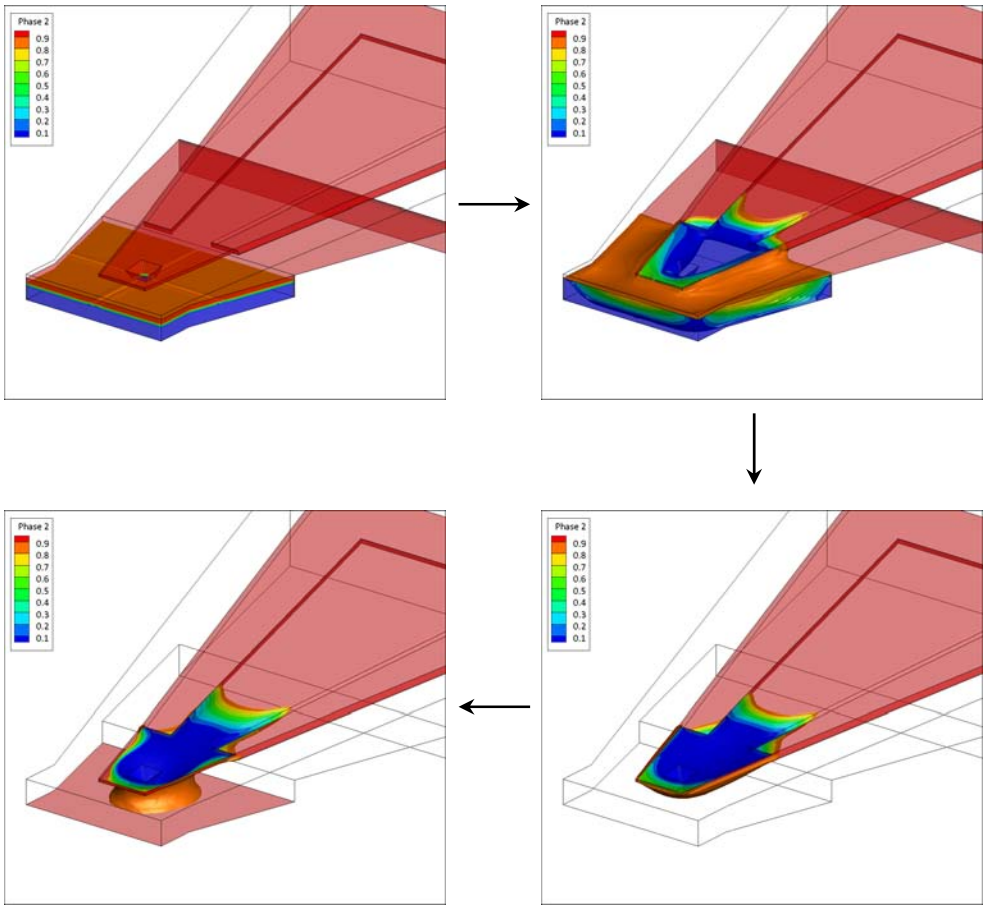

Fig. 17. Deposition of inks over the substrate – The pen extraction from the inkwell is simulated by incorporating the outlet boundary condition (gauge pressure is *0*) for all surfaces except cantilever itself.

Numerical analysis results can be used for parametric investigations for various combinations between different inks and substrates. Specially, nano-array patterned by DPN exhibits highly uniform and repeatable features within and between nano-arrays. So, this enables ultra-sensitive protein detection with even femto-scale quantities. The consistency should be ensured for the improvement of sensitivity and reproducibility.

Eventually, the changes by different ink solutions or substrates can be obtained by using different material properties. Figure 18 and 19 are measured material properties (such as viscosity, contact angle, and surface tension) used for the numerical analysis of DPN-based nano-patterning for biological protein (i.e., Rabbit IgG) detection.

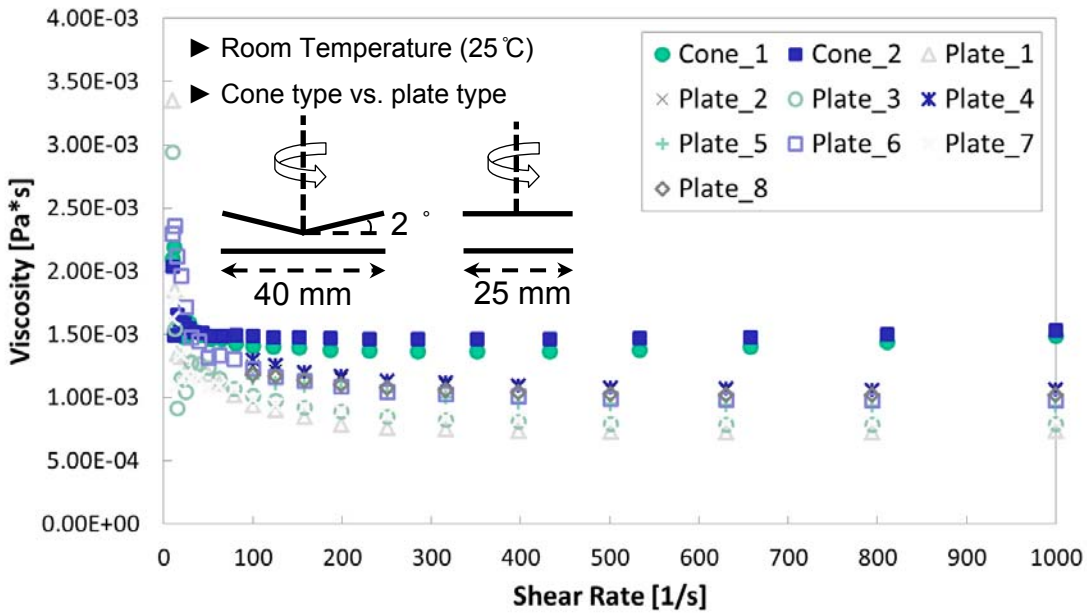

Fig. 18. Viscosity measurements of protein inks using rheometer (Model: *AR 2000x*, TA instruments, New Castle, DE).

(a)

Categories	Average Values [*degrees*]	Standard Deviation
Hydrophobic Area	*98.63*	*0.202*
		
Hydrophilic Area	*63.10*	*3.363*
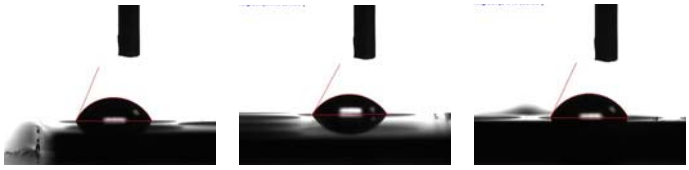		

(b)

Density Ratio with Water	Average Values [*N/m*]	Standard Deviation
1	*0.0573*	*0.005873*
0.95	*0.0544*	*0.005579*
		

(c)

Fig. 19. Contac angle and surface tension measurements of protein inks using video contact angle measurement system (a) Model: VCA Optima (AST Products, Inc., Billerica, MA) (b) Averaged values of contact angle and (c) surface tension.

B. Analysis of Nonlinear Dynamics during DPN Processes

For deposition of nano-materials by DPN on the surface of a microcantilever, the dynamic behavior of the microcantilever should be analyzed to ensure the repeatability of the DPN process. The non-linear response arising from the vibration of a microcantilever due to sliding motion of the writing probe therefore needs to be ascertained. The numerical analysis for the dynamic response of a microcantilever when subjected to a sliding probe was performed by using a point-mass model [37]. The following section has been adapted from [37].

The physical representation of an oscillating cantilever (Figure 20a) is simplified to an equivalent point-mass model (as shown in Figure 20b).

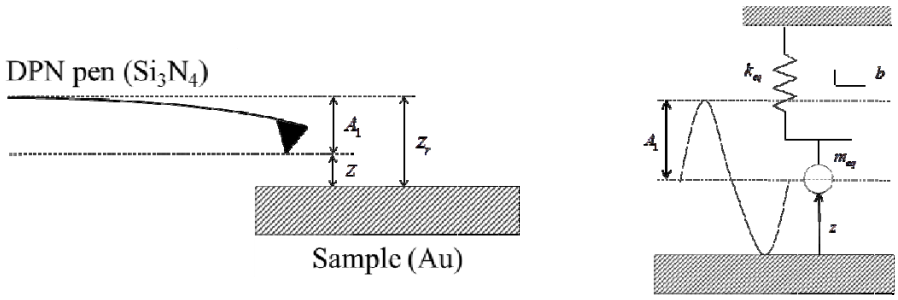

(a) (b)

Fig. 20. Equivalent point-mass representation of a cantilever oscillating in a single eigenmode (a) Schematics of the dynamics between tip and sample; (b) Corresponding point-mass model [37]*.

* Reprinted with permission from "Point-Mass Model for Nano-Patterning Using Dip-Pen Nanolithography (DPN)" by S.-W. Kang, D. Banerjee, 2011, *Sensors & Transducers*, 11, Special Issue, pp. 64-73, Copyright 2011 by International Frequency Sensor Association (IFSA).

During the deposition step, the probe will oscillate in a direction perpendicular to that of the substrate. The governing equation of the simplified model is given by [89-91]

$$m_{eq}\ddot{z} + b\dot{z} + k_{eq}(z - z_r) = F_0 \cos(\omega t) + f_{TS}(t) \tag{2.3}$$

where z is the cantilever position with respect to the surface, $F_0=k_{eq}A_1$ is the driving force (A_1 is the driving amplitude) [N], ω is the driving frequency [Hz], $f_{TS}(t)$ is the tip-sample interaction force [N] and $b=m_{eq}f_n/Q$ is the damping coefficient, where f_n is the natural frequency [Hz] and Q is the quality factor. The corresponding masses m_{eq} [kg] and flexural stiffness $k_{N,eq}$ [N/m] to the equivalent model is determined from the kinetic (T) and potential (V) energy balance between a continuous model and a point-mass model [90].

$$m_{eq} = \frac{1}{4} m_c \text{ and } k_{N,eq} = \frac{1}{12} k_c \alpha_i^4 \tag{2.4}$$

where $m_c=\rho_c L_c$ is the total mass of the cantilever [kg], $k_c=3E_cI_c/L_c^3$ and α_i is the i^{th} solution of the dispersion relation, $cos(\alpha)cosh(\alpha)+1=0$, such that the resonance frequency $\omega_{i,n}^2=E_cI_c\alpha_i^4/\rho_cL_c^4$ ($\alpha_1=1.875$, $\alpha_2=4.694$ and $\alpha_3=7.855$). In scanning mode, the probe undergoes both lateral as well as torsional deflection. The effective spring constant in lateral mode is defines as [92-93]

$$\frac{1}{k_{L,eff}} = \frac{1}{k_{lat}} + \frac{1}{k_{tor}} \tag{2.5}$$

where

$$k_{lat} = k_{N,eq}\left(\frac{w}{t}\right)^2 \text{ and } k_{tor} = k_{N,eq}\frac{1}{2}\left(\frac{L_c}{h}\right)^2 \tag{2.6}$$

In DPN process, the tip-sample interaction force (or repulsive force) in contact force regime and the adhesion force due to the capillary bridge is balanced to maintain constant contact between tip and sample. The tip-sample force based on DMT (Derjaguin-Muller-Toporov) model is used in this study as follows [94]:

$$f_{N,TS}(t) = \frac{4}{3}E^*\sqrt{R}(d_0 - z)^{3/2} \tag{2.7}$$

with

$$\frac{1}{E^*} = \frac{\left(1-\nu_t^2\right)}{E_t} + \frac{\left(1-\nu_s^2\right)}{E_s} \tag{2.8}$$

where R is the tip radius [m], d_0 is the intermolecular distance between tip and sample [m] and E^* is the effective elasticity [Pa], where E_c, v_c and E_s, v_s are the elastic module and Poisson's ratios of the tip and sample, respectively. In scanning mode, the tip-sample interaction force at the lateral direction is given as a function of the normal value [95].

$$f_{T,TS}(t) = f_{L,TS}(t) = 8G^*\left(\frac{3Rf_{N,TS}}{4E^*}\right)^{1/3} \quad for \quad z \le d_0 \tag{2.9}$$

with

$$\frac{1}{G^*} = \frac{\left(2-\nu_t\right)}{G_t} + \frac{\left(2-\nu_s\right)}{G_s} \text{ where } G = \frac{E}{2\left(1+\nu\right)} \tag{2.10}$$

In this study, the natural frequencies in flexural and lateral modes are calculated by performing numerical simulations using Finite Element Analyses (FEA) tool (Ansys®) and theoretical analysis using Maple® (Maplesoft, Waterloo, Canada). The FE models for the harmonic simulations in Ansys® were meshed by *SOLID45* elements and the normal (k_n) and lateral (k_l) stiffness is simply expressed as [96-98]:

$$k_n = \frac{\partial F_{st}}{\partial d} = (6RE^{*2}F_N)^{1/3} \tag{2.11}$$

$$k_l = \frac{k_n}{E^*}\left[\frac{\left(1-\frac{\nu_s}{2}\right)(1+\nu_s)}{E_s} + \frac{\left(1-\frac{\nu_t}{2}\right)(1+\nu_t)}{E_t}\right]^{-1} \approx k_n \frac{1-\nu}{1-\frac{\nu}{2}} \tag{2.12}$$

where the approximate relation $k_l \approx 0.9k_n$ applies to an incompressible tip. The parameters for theoretical calculation are summarized in Table IV.

Figure 21 and Figure 22 represent the natural frequency estimated by the theoretical and FEA models, respectively. FEA results shown in Figure 22 represent the natural frequencies in both air and consideration of the interaction with the *Au* coated substrate. The increase in natural frequency during DPN process as opposed to the ambient condition can be explained from the additional contributions to the total effective stiffness by that of the tip-sample interaction.

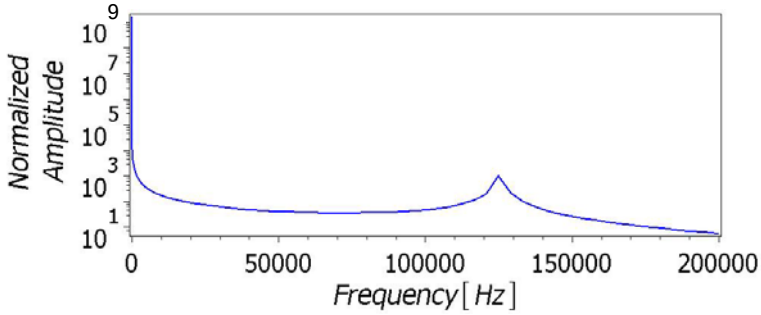

(a)

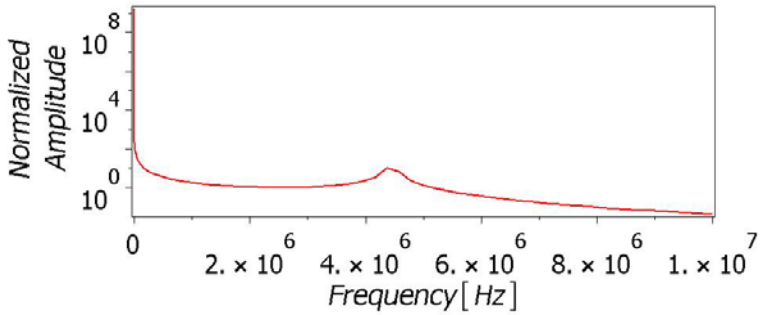

(b)

Fig. 21. Natural frequency estimated by the theoretical models (a) normal (b) lateral-directions [37][*].

[*] Reprinted with permission from "Point-Mass Model for Nano-Patterning Using Dip-Pen Nanolithography (DPN)" by S.-W. Kang, D. Banerjee, 2011, *Sensors & Transducers*, 11, Special Issue, pp. 64-73, Copyright 2011 by International Frequency Sensor Association (IFSA).

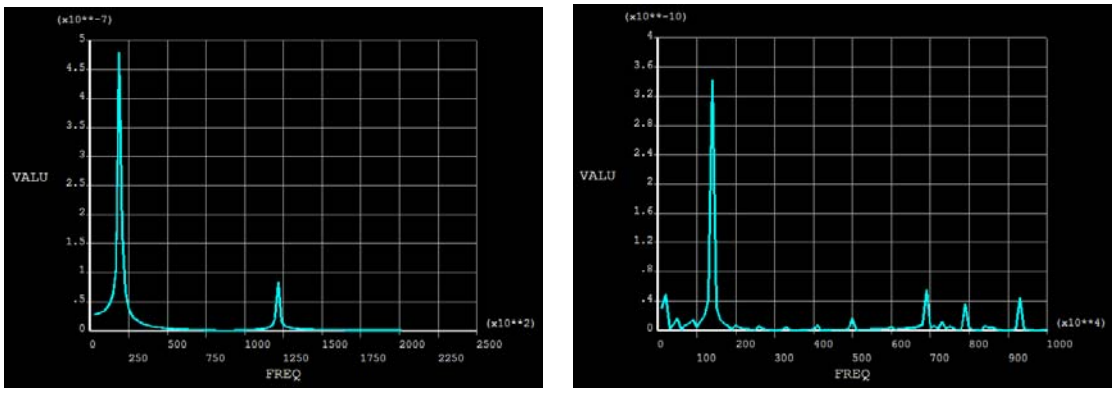

(a) (b)

Fig. 22. Simulation results of FEA model (a) normal (b) lateral-directions [37]*.

In addition, Figure 23 shows the effect of tip-sample interaction force on the tip position. These results are obtained by solving equation (2.3) in flexural mode using *ODE45* function in Matlab® (Mathworks Inc., Natick, MA). From the results, the amplitude values are observed to diverge at the driving frequency of $\omega = 120\ Hz$ which is identical to the natural frequency of the point-mass and FEA models.

The operation of deposition mode in fluid environment causes the attenuation of the vibration due to the increased hydrodynamic damping (or the decrease in the quality factor; i.g., from *100 ~ 400* in air to *1 ~ 5* in fluids [91, 99]) as shown in Figure 24. This analysis helps to determine the operating parameters for performing the direct deposition of nano-fins (CNT) on the microcantilever surface using DPN technique.

* Reprinted with permission from "Point-Mass Model for Nano-Patterning Using Dip-Pen Nanolithography (DPN)" by S.-W. Kang, D. Banerjee, 2011, *Sensors & Transducers*, 11, Special Issue, pp. 64-73, Copyright 2011 by International Frequency Sensor Association (IFSA).

Table IV. Constants and properties of the Si_3N_4 microcantilever and *Au* sample used in numerical computation [37][*].

Description	Value
Tip radius	$R = 15\ nm$
Cantilever length	$L = 200\ \mu m$
Cantilever width	$b = 45\ \mu m$
Cantilever thickness	$h = 600\ nm$
Cantilever material density	$\rho_c = 3100\ kg/m^3$
Cantilever Young's modulus	$E_c = 210\ GPa$
Cantilever Poisson ratio	$v_c = 0.22$
Sample material density	$\rho_s = 19320\ kg/m^3$
Sample Young's modulus	$E_s = 80\ GPa$
Sample Poisson ratio	$v_s = 0.4$
Effective elastic modulus	$E^* = 66.53\ GPa$
Static bending stiffness	$k = 0.064\ N/m$
1st natural frequency	$f_1 = 19.358$
Q factor (in air)	$Q = 80.0$
Hamaker constant (Si_3N_4-Au)	$A_H = 32.5 \times 10^{-20}\ J$
Intermolecular distance	$a_0 = 2.0\ Å$

[*] Reprinted with permission from "Point-Mass Model for Nano-Patterning Using Dip-Pen Nanolithography (DPN)" by S.-W. Kang, D. Banerjee, 2011, *Sensors & Transducers*, 11, Special Issue, pp. 64-73, Copyright 2011 by International Frequency Sensor Association (IFSA).

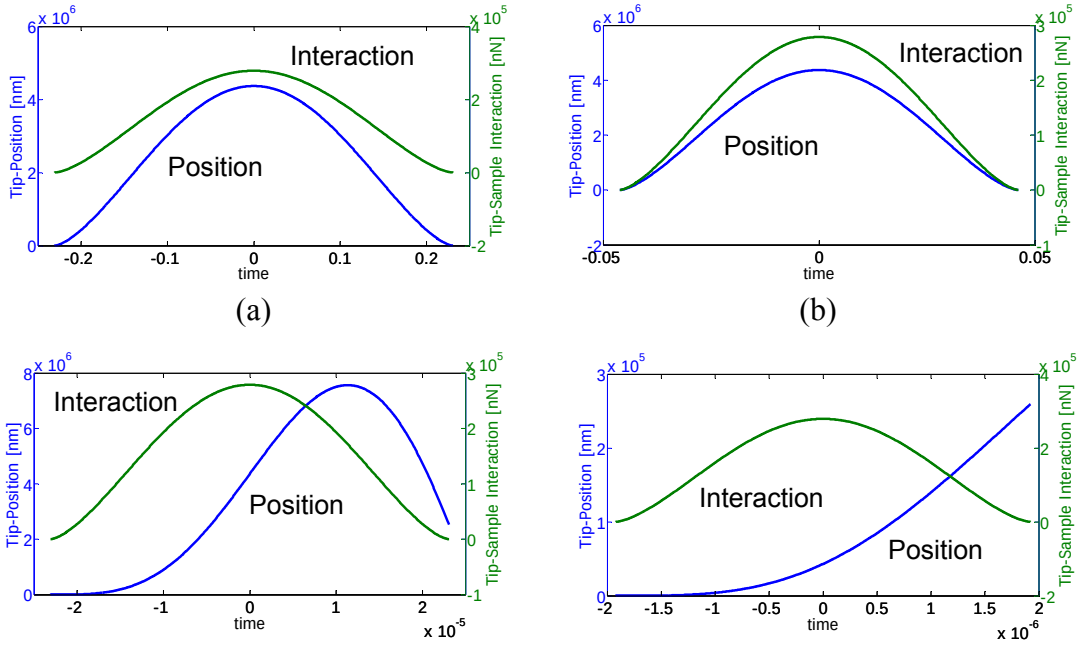

Fig. 23. Tip position in one oscillation cycle (a) $\omega = 1\ Hz$ (b) $\omega = 5\ Hz$ (c) $\omega = 10\ Hz$ (d) $\omega = 120\ Hz$ [37]*.

* Reprinted with permission from "Point-Mass Model for Nano-Patterning Using Dip-Pen Nanolithography (DPN)" by S.-W. Kang, D. Banerjee, 2011, *Sensors & Transducers*, 11, Special Issue, pp. 64-73, Copyright 2011 by International Frequency Sensor Association (IFSA).

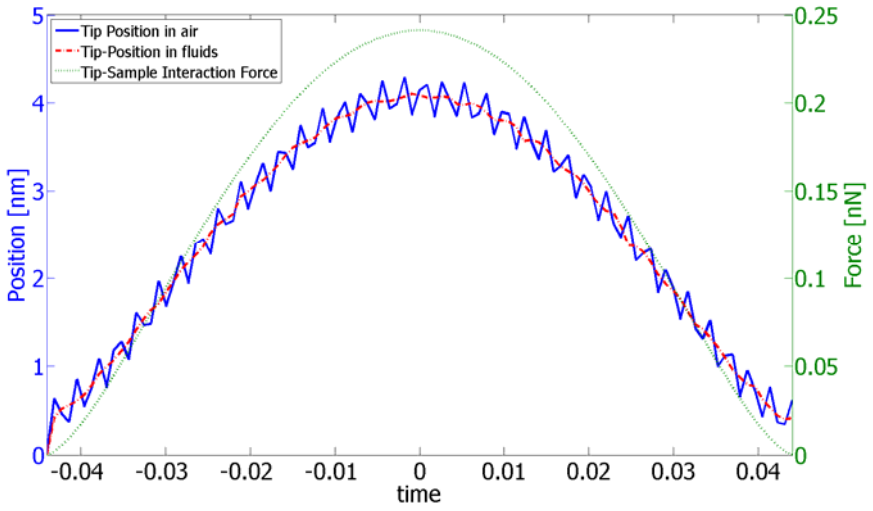

Fig. 24. Tip position and force in one oscillation cycle at the driving frequency $\omega = 1$ *Hz* [37]*.

C. Synthesis of Carbon Nanotubes (CNTs)

Carbon Nanotubes (CNTs) are allotropes of carbon with a cylindrical crystal structure which can be self-organized to form either single-walled carbon nanotubes (SWNTs) or multi-walled carbon nanotubes (MWNTs). CNT have been proposed for incorporation into a variety of solid state electronics devices - due to their outstanding material properties (electrical, magnetic, optical, mechanical, thermal, chemical, etc.) and also for their unique ability to yield tunable properties by controlling the crystal structure (or "chirality"). Properties that can be tuned (or manipulated) based on chirality

* Reprinted with permission from "Point-Mass Model for Nano-Patterning Using Dip-Pen Nanolithography (DPN)" by S.-W. Kang, D. Banerjee, 2011, *Sensors & Transducers*, 11, Special Issue, pp. 64-73, Copyright 2011 by International Frequency Sensor Association (IFSA).

include - ultra-high thermal conductivity, ballistic electron mobility, and superior mechanical strength [100-105].

However, the primary impediment to the incorporation of CNTs in these novel and proposed applications has been the lack of a suitable synthesis protocol. It was argues – that successful incorporation of CNTs in nano-electronics can be achieved only if a robust synthesis protocol can be developed that enables precise control over the chirality, selectivity in location (location of deposition/ patterning of the required CNT nanoparticles), orientation of the patterned CNTs and with sufficient number (or spatial) density [100].

In this study, various methods are explored such as the direct deposition of aqueous suspension of CNT nanoparticles that are chemically functionalized or physically dispersed in a solvent. For example, Amine-functionalized and surfactant-coated (e.g., Gum Arabic) CNTs are attractive options for ink formulations that can be used for nano-scale patterning using DPN. In contrast, a radically different approach is the in-situ synthesis of CNTs from catalyst nano-particles loaded onto on a scanning probe tip (e.g., using DPN technique), and/ or synthesis by plasma-enhanced chemical vapor deposition (PECVD) process [83, 106-107] from catalyst precursors (e.g., metal salts that form carbide eutectics: *Ni*, *Co*, *Pd*, *Fe*(*II*), *Fe*(*III*), *Pt*, and *Rh*) that are patterned on a substrate using DPN.

CNTs (and other nanoparticle/ nanowires – such as from gold or silicon) are typically synthesized from metal catalysts (or their precursors – such as aqueous salt solutions of these metal catalysts). The metal catalysts nanoparticles – such as *Pd*, *Pt*, *Ni*,

Co, *Fe* or Au (or nanopatterns of the precursor material – such as $PdCl_2$, $PtCl_2$, $FeCl_3$, $NiCl_2$, etc.) are deposited on a substrate or scanning probe tip - by DPN. Subsequently, the deposited materials can be exposed to an organic material (e.g., a carbonaceous gas) or coated with the liquid suspension of an organic solution or suspension, or coated by vapor deposition (e.g., organic gasses or Fullerene). A simpler approach can be to use organometalics as the precursor that contains both the catalyst material and the organic seed – that are required for the synthesis of CNTs (or inorganic nanowires). The substrate that contains both the catalyst (or precursor) and the seed material (organic or inorganic material) is exposed to the optimum conditions that can enable the chemical reactions to proceed that yields the CNTs (as well as any other type of organic or inorganic nanoparticles/ nano-wires) – such as CVD, PECVD, laser ablation, etc. [100, 106-113]. The role of the metal catalysts is to form a eutectic compound of metal and carbon (or inorganic material such as *Si*) – that leads to synthesis and growth of nanotube or nanowire. For CNTs, typically growth of CNTs is envisioned to occur when the carbon atoms precipitate from the catalyst after it forms a eutectic melt-pool [114]. Prior research results using similar approaches are available in the literature [115-121].

The following section has been adapted from [83]. Figure 25 shows the lateral force microscopy (LFM) images of nano-patterns of metal ($NiCl_2$) catalysts deposited on silicon substrate by DPN (Nscriptor: NanoInk, Inc., Skokie, IL) at the materials characterization facility of Texas A&M University. The $NiCl_2$ powder (*10 mg*) is dissolved in DI water (*10 mL*) to form aqueous solutions (*0.008 M*) by mixing using ultra-sonicator for *30 min*. The scanning probe tip is coated twice with ink materials by dipping it in an ink droplet for *1 - 2 min* (double dipping procedure [83, 121]) and air-drying for *30 sec* as shown in Figure 26, before the tip is contacted with the substrate for the deposition.

The scanning electron microscopy (SEM) images of CNTs grown on $NiCl_2$ catalyst nanoparticles (pre-deposited by DPN) by PECVD process is shown in Figure 27. This work was performed in collaboration with the research group of Dr. Kaul at NASA (National Air and Space Agency) / JPL (Jet Propulsion Laboratory) at Caltech (California Institute of Technology) [83]. At the pressure of $\sim 2 \times 10^{-6}$, high-purity acetylene (C_2H_2) and ammonia (NH_3) was used as the carrier gas for carbon source (organic seed). In PECVD method, the inherent electric field in the plasma enables the excellent vertical alignment of CNTs during synthesis.

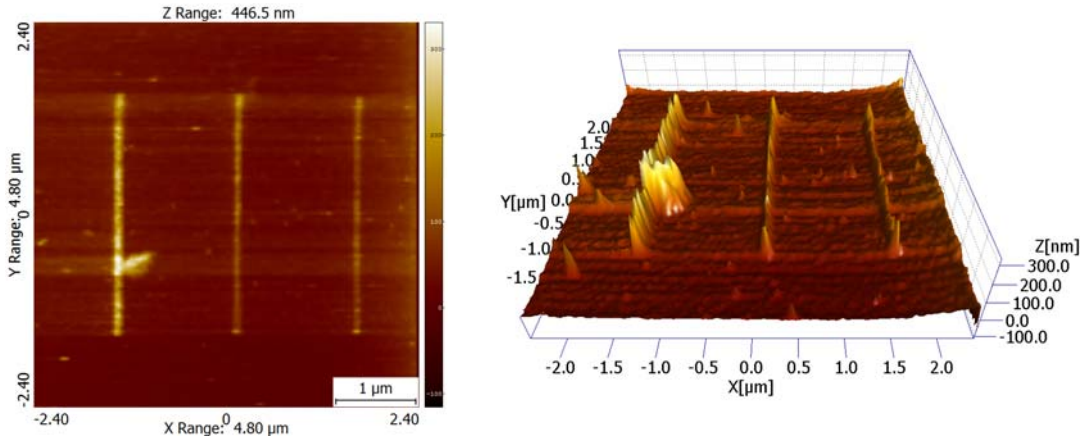

(a)

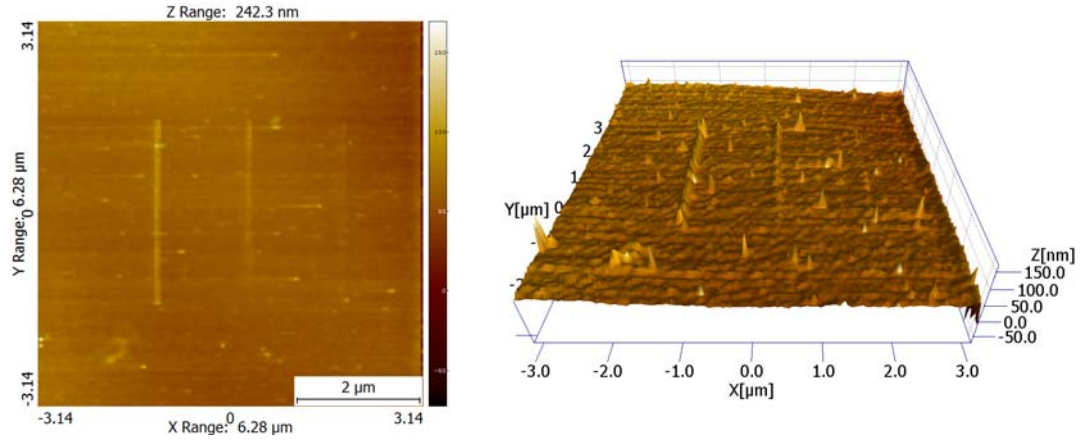

(b)

Fig. 25. Lateral Force Microscopy (LFM) image of $NiCl_2$ deposited by DPN on Sindex™ chip: (a) writing speed [*µm/s*]: *0.1*, *0.2*, *0.4*, scan size: *4.80 µm*, scan speed: *3 Hz* (b) writing speed [*µm/s*]: *0.05*, *0.1*, *0.15*, scan size: *6.30 µm/s*, scan speed: *3 Hz* [83][*].

[*] Reprinted with permission from "Nanopatterning of Catalyst by Dip-Pen Nanolithography (DPN) for Synthesis of Carbon Nanotubes (CNT)" by S.-W. Kang, D. Banerjee, A.B. Kaul, K.G. Megerian, 2010, *Scanning*, 31(1), pp. 42-48, Copyright 2010 by John Wiley and Sons.

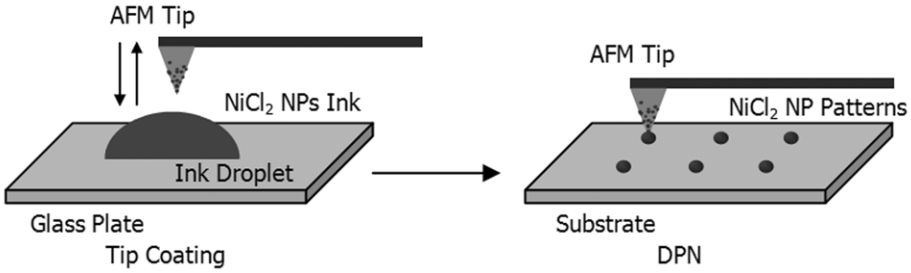

Fig. 26. Schematic illustration of the process: AFM tip coating, fabrication of $NiCl_2$ NP patterns by using DPN (Right – Double dipping procedure/ Left – DPN process) [83]*.

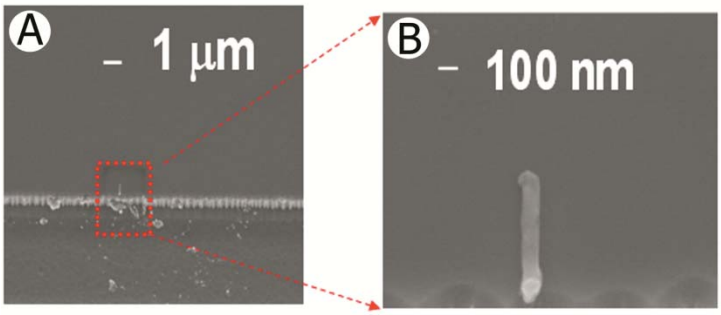

Fig. 27. (a) Left image is a low magnification image of a single vertically oriented tube (b) a high magnification SEM image of the same tube: Tilt angle in the SEM is *30 degrees* [83]*.

DPN requires the coating of scanning probe tip by using a liquid solution of ink materials. However, CNTs are basically insoluble in water. Thus, colloidal suspension of CNTs is prepared by chemical functionalization or surfactant (e.g., Gum-Arabic)

* Reprinted with permission from "Nanopatterning of Catalyst by Dip-Pen Nanolithography (DPN) for Synthesis of Carbon Nanotubes (CNT)" by S.-W. Kang, D. Banerjee, A.B. Kaul, K.G. Megerian, 2010, *Scanning*, 31(1), pp. 42-48, Copyright 2010 by John Wiley and Sons.

dispersion. These methods have the following advantages compared with conventional CVD method: (a) low temperature operation (b) preserved properties of CNTs after synthesis (c) low cost (d) quick and simple characterization by LFM right after deposition. Figure 28 represents LFM images of CNTs patterns obtained from direct deposition by DPN. The direct deposition of CNT by DPN was performed on Sindex^{TM} (Base Si substrate: purchased from Bioforce Nanosciences, Ames, IA) chip. The ink was formulation was achieved by using ethylene diamine-functionalized single-walled CNTs (EDA-SWNTs) and Gum-Arabic (GA) dispersed multi-walled CNTs (GA-MWNTs) inks. In the literature [122] GA is known to be an excellent dispersant of CNTs in aqueous solutions.

The experimental conditions for successful deposition of CNTs are sensitive to small variations in the individual steps in the experimental protocol. In our experiments using EDA-SWCNT solution, the deposition on *Si* substrate was accomplished only after the RH value exceeded *~75 %*. On the other hand, the deposition of GA-MWNTs on *Si* substrate was not affected by RH. Figure 29 shows the relationship between contact time and radius of dot. The dot size was decreased with decrease in contact time. Also, Figure 30 shows the plot of the width of line shaped features as a function of writing speed in GA-MWNTs deposition on Si substrate.

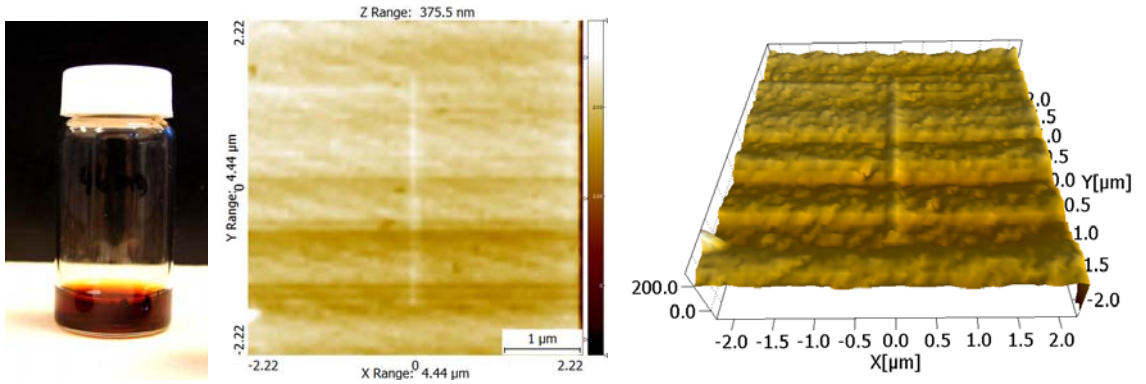

(a)

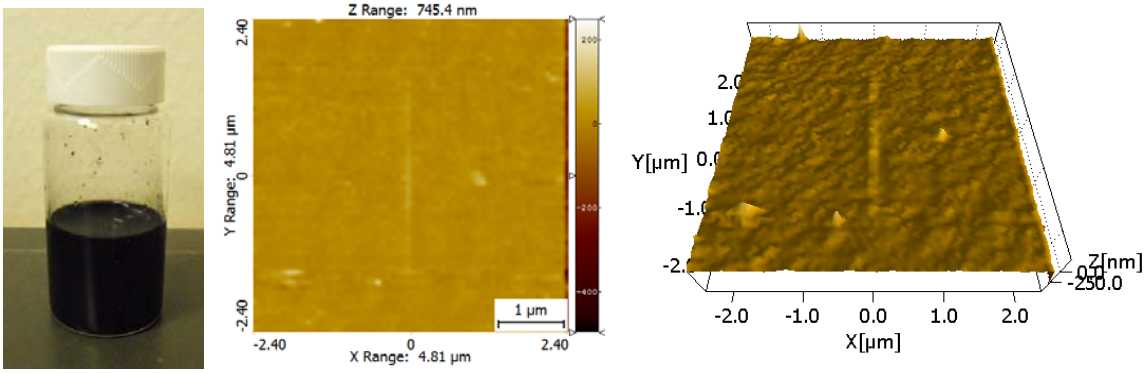

(b)

Fig. 28. LFM Images of CNTs deposited by DPN on Sidex™ chip (a) EDA-SWNTs solution of *10 pH* – writing speed: *0.15 µm/s*, scan size: *4.44 µm*, scan speed: *4 Hz* (b) GA-MWNTs solution – writing speed: *0.05 µm/s*, scan size: *4.81 µm*, scan speed: *3.5 Hz*.

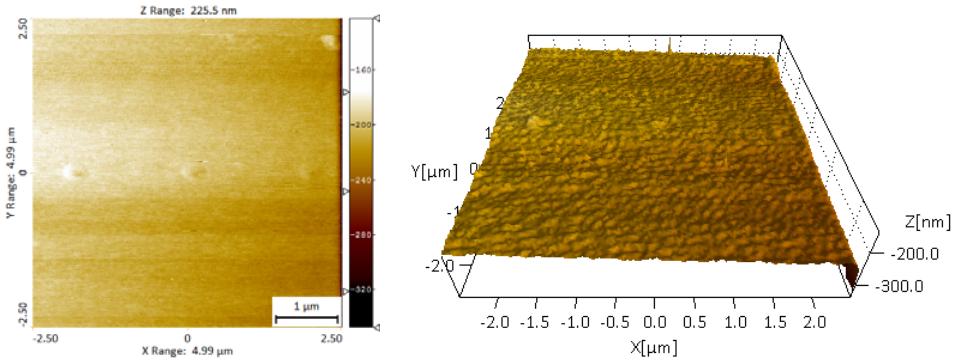

(a)

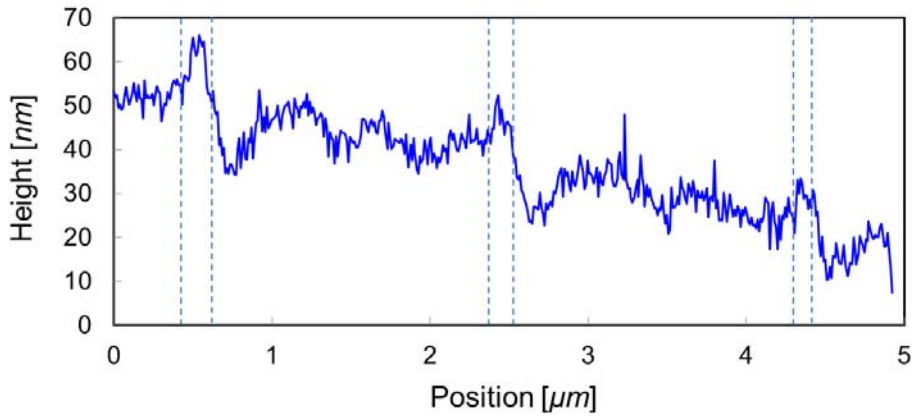

(b)

Fig. 29. Comparison of the dot size between different contact time (*100*, *50*, and *25 sec*): (a) $PdCl_2$ nanoparticles deposited on *SiO* substrate by DPN (b) Line analysis to estimate the feature size.

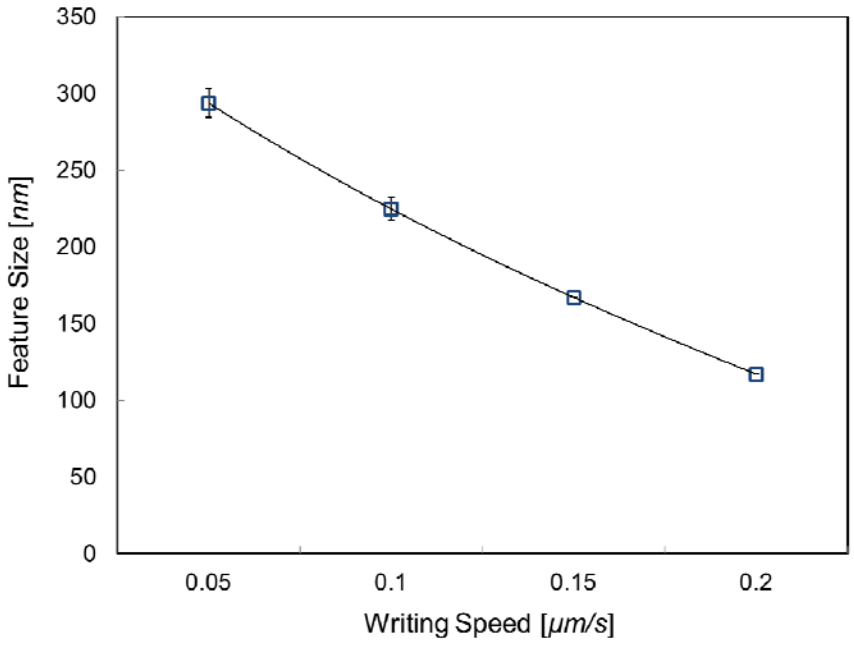

Fig. 30. Dependence of feature size on writing speed.

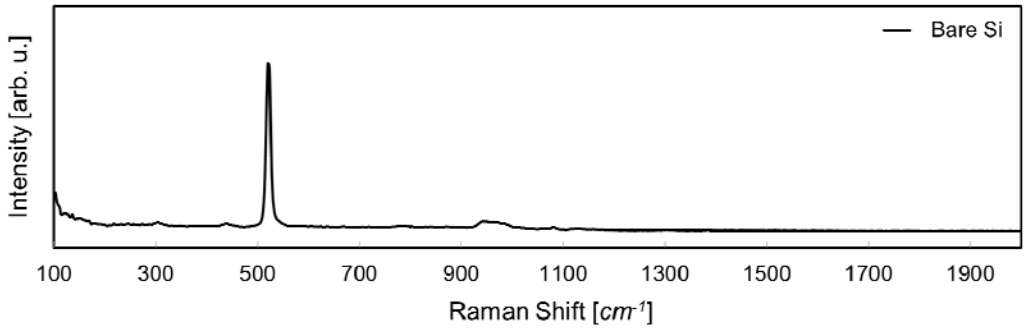

(a)

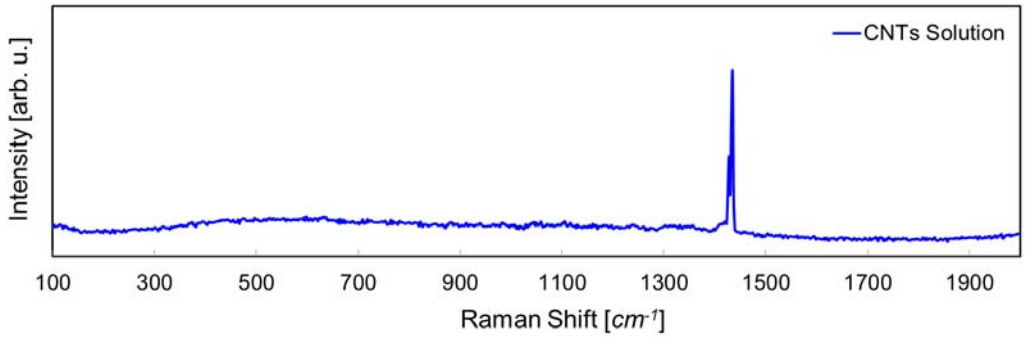

(b)

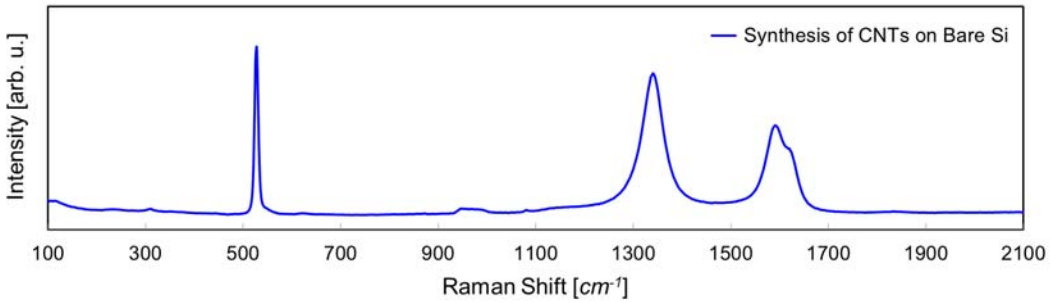

(c)

Fig. 31. Raman spectra of (a) the *Si* substrate: (b) EDA-SWNTs solution (c) GA-MWNTs (The resonant peaks of CNTs are in the range of *1400 ~ 1700 cm*$^{-1}$).

Another important factor that affects the DPN process is the combination (or compatibility) between ink material composition and the substrate morphology. The compatibility is determined by the chemical affinity of the ink to the writing probe as well as the substrate surface (which is also affected by the surface roughness). In the experiments using EDA-SWNTs, higher solution *pH* enables bigger feature size, which means the adhesion force as well as the affinity for surface adsorption between substrate (*Si*) and Inks (EDA-SWNTs solution) is enhanced at higher *pH* value.

Since DPN is based on scanning probe microscopy (SPM) technique, it basically provides the scanning mode (i.e., lateral force microscopy: LFM) which is usually performed immediately after the deposition step. However, LFM does not provide the information about the chemical composition of the deposited features. Hence, Raman spectroscopy is typically used for the verification (or materials characterization) of the CNTs inks that were deposited in this study. Figure 31 represents the resonant vibrational peaks of each sample that was deposited by DPN – thus verifying the successful deposition of CNTs by DPN.

D. Synthesis of CNTs on the Microcantilever

In this study, CNTs are synthesized on a microcantilever substrate (*Au*-coated Si_3N_4) via post-growth from metal catalyst precursors (Palladium Chloride: $PdCl_2$) pre-deposited by DPN. The synthesis of CNTs from C_{60} vapor [112-113] or C_{60}-metal catalysts layers [123-124] has been investigated in previous studies. Initially, $PdCl_2$

(procured from Sigma-Aldrich, St. Louis, MO) is deposited by DPN on the cantilever as the catalysts for growing CNTs. Figure 32 shows the setting of DPN for the deposition of metal catalysts using NScriptor ™ instruement. In the left hand side of Figure 32, the dark-colored microcantilever on the top is the Pen cantilever coated with aqueous $PdCl_2$ solution and the relatively bright colored microcantilever represents the substrate.

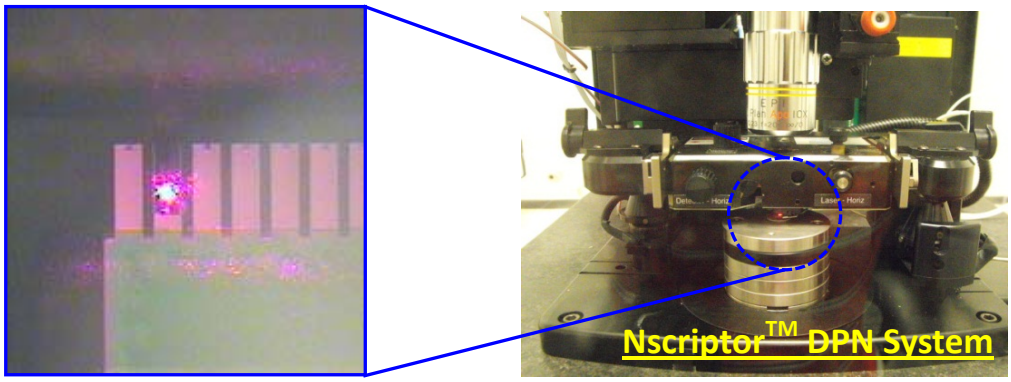

Fig. 32. DPN setting for the deposition on the microcantilever (Pen: $PdCl_2$ inks coated Type A pen purchased from NanoInk, Inc./ Substrate: Type E passive pen purchased from NanoInk, Inc.).

Figure 33 shows the experimental setup for growing CNTs. The desiccators is connected with ultra-high purity N_2 gas line used to remove H_2O vapor and O_2 gas inside the chamber for preventing the oxidation of carbon source (C_{60}: Fullerene, purchased from Nano-C, Westwood, MA) as well as metal catalysts. The process temperature is verified by using an infrared camera and a thermocouple (that is embedded on the heater) to ensure the uniformity of the surface temperature.

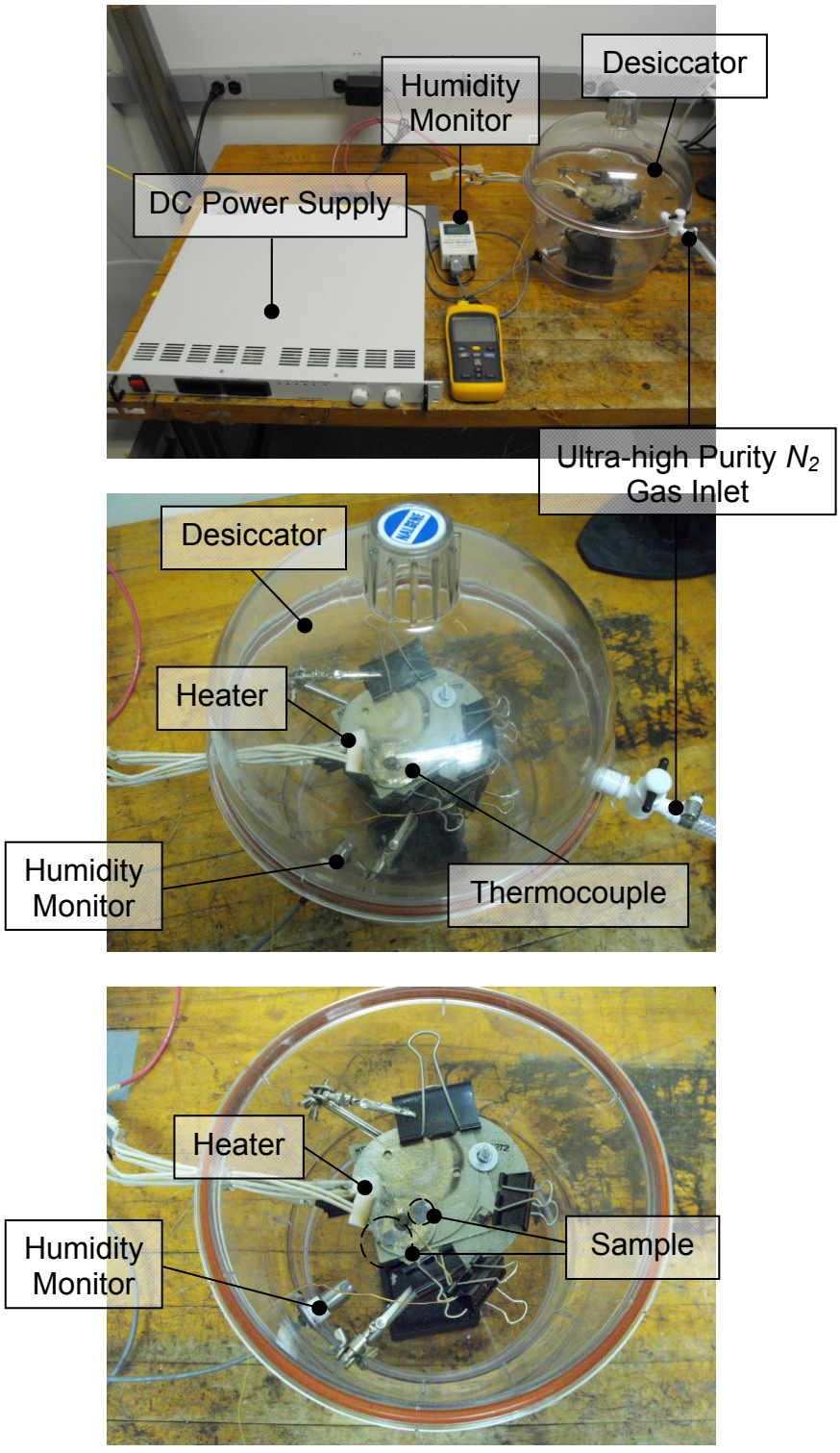

Fig. 33. Experimental apparatus for CNTs growth.

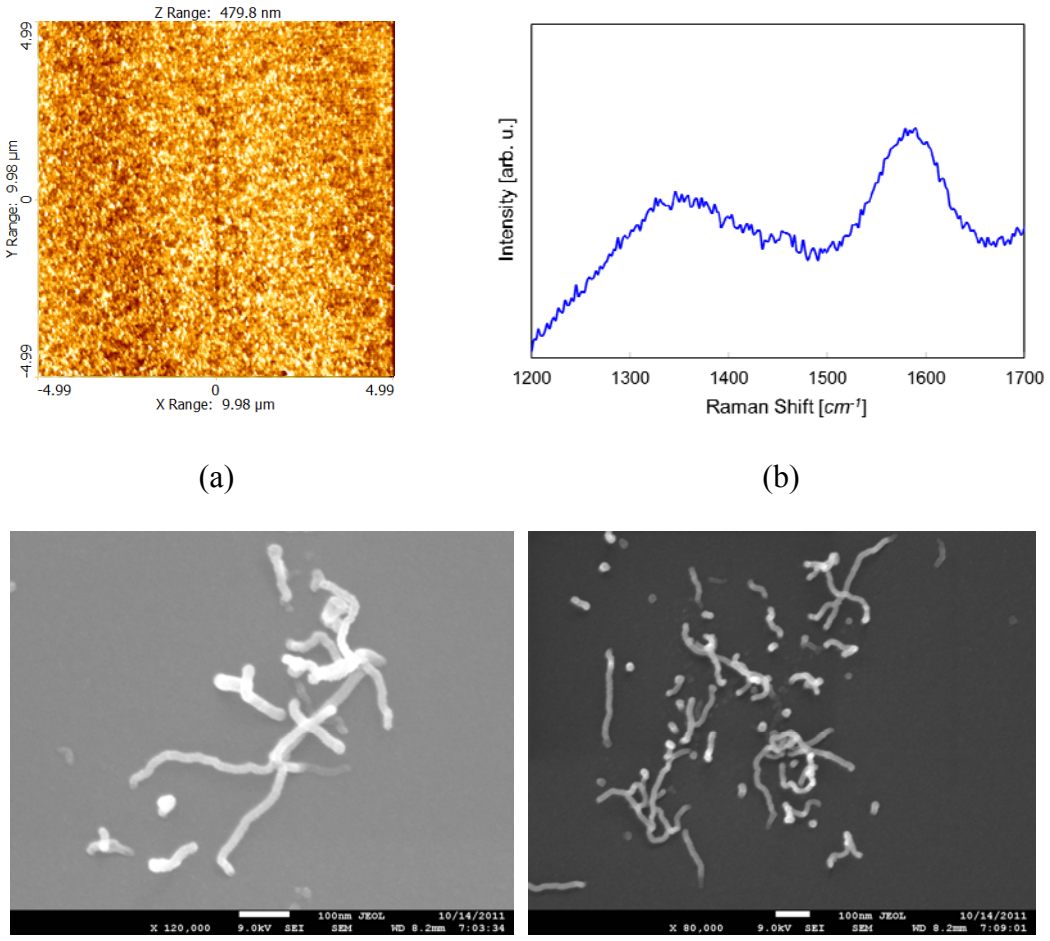

(a) (b)

(c)

Fig. 34. (a) LFM image of line features deposited by DPN on *Au*-coated Si_3N_4 microcantilever (Type E passive probe), (b) Raman characterization and (c) SEM images of CNTs grown at *600 °C*.

The materials characterization of the synthesized CNTs performed by using Raman spectroscopy and SEM. Figure 34(a) is LFM image of $PdCl_2$ nano-particles deposited on the top surface of cantilever by DPN. After deposition of metal catalysts, a single droplet of C_{60} solution (mixture of Toluene and Fullerene) is dropped on the area where metal catalysts are deposited in order to form C_{60}-$PdCl_2$ nanoparticle mixture. Finally, the sample is heated up to approximately *600 °C* for the growth of CNTs. Figure 34(b) and (c) represent the Raman peaks (R and G band) and SEM images of CNTs synthesized through this investigation.

Finally, the same procedure is applied to the bimorph microcantilever platform to verify the enhancement of sensor sensitivity by coating of high-thermal conductivity materials (i.e., CNTs). At first, for successful deposition of metal catalysts, the cantilevers are cleaned by plasma cleaning method (gas mixture of O_2 *20 %* and *Ar 80 %*) using RIE (Reactive-Ion Etching) instrument. Figure 35 shows the square-shaped deposited features and experiment setting of pen (Type NP probe with spring constant of *0.06 N/m*, purchased from Veeco, Santa Barbara, CA) and substrate cantilevers (Active Pen Model# DS001, purchased from NanoInk, Inc., Skokie, IL). After dropping a single droplet of C_{60} solution on the surface of bimorph microcantilever, the cantilever is electrically heated by micro-heater attached at its base (*50 mA* for a period of *5 min*) [117] for the growth of CNTs.

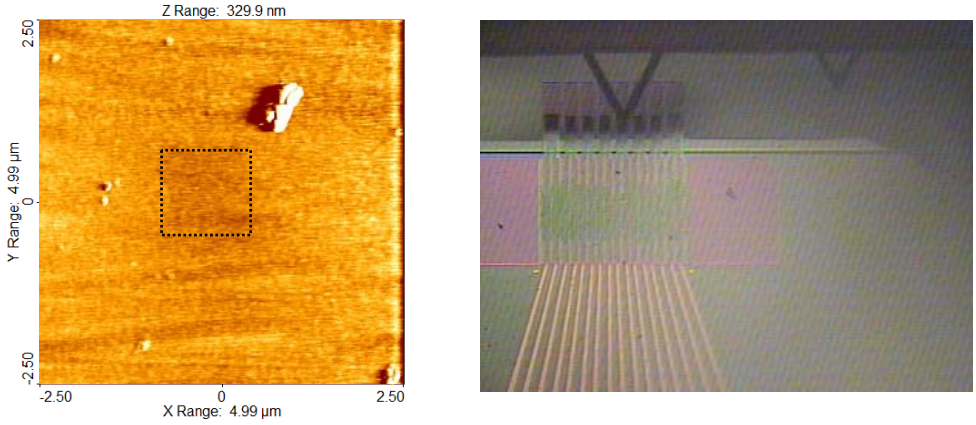

(a) (b)

Fig. 35. Surface cleaning and results of DPN experiments for the deposition of $PdCl_2$ nanoparticles on the bimorph microcantilever surface (a) LFM image (Square: *1 µm × 1 µm*) (b) Setting of pen (Top) and substrate (Bottom) cantilevers.

However, the solution is not exactly spread over the metal catalysts due to surface tension effect and initially deflected shape of bimorph microcantilever. This is verified by the experiment of CNTs growth $PdCl_2$-C_{60} layer formed by dropping a droplet for both solutions. Figure 36 shows the SEM image of carbon nano-structures formed at the edge and corner of the microcantilever. Since the nano-structures are not existed on the top surface of the cantilever, Raman peaks is not successfully obtained but the nano-structures is verified as carbon structures by EDS (Energy Dispersive X-Ray Spectrometer) analysis. The deflection measurements using this microcantilever are presented in Chapter V (Experimental Results).

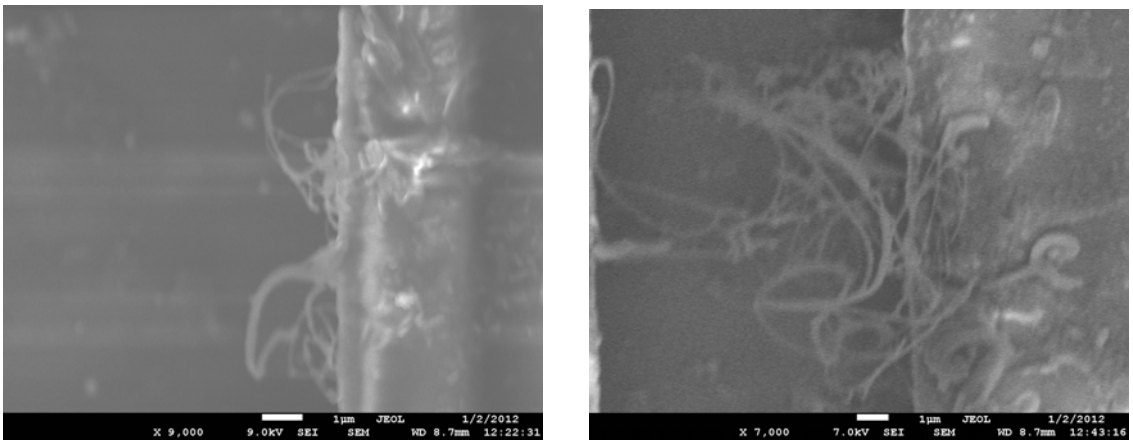

Fig. 36. SEM images obtained from the experiment using $PdCl_2$-C_{60} layer formed by dropping a droplet.

Three different approaches approached for the synthesis of CNTs were successfully explored in this study. Hence, the in-situ synthesis method by using DPN technique confers several advantages and obviates the restrictions for commercial application on CNTs in nano-electronic devices. This method yields stable and continuous pre-depositions of metal catalysts – that are crucial for the mass production (and large-scale nano-patterning) of CNTs. Most importantly, the surface roughness of the substrate for synthesis of CNTs should be low (e.g., *5 nm* or less) and uniform. However, the required surface roughness in the nano-synthesis process is a challenging issue for the synthesis of CNTs on MEMS/NEMS devices – especially for thermally actuated devices (such as explosives sensors and nano-calorimeters that are explored in this study).

CHAPTER III

MODELING AND SIMULATION

A. Governing Equations

The flow regime is assumed to be steady, incompressible and laminar. The gas mixture is treated as an ideal gas. Basically, the set of governing equations used in this study includes continuity equation (or conservation of mass), equation of motion (or momentum conservation), energy balance (or thermal energy equation), and material balance equation (or species equations).

$$\frac{\partial \rho}{\partial t} + \frac{\partial}{\partial x_j}\left(\rho u_j\right) = 0 \tag{3.1}$$

$$\frac{\partial \rho u_i}{\partial t} + \frac{\partial}{\partial x_j}\left(\rho u_i u_j\right) = -\frac{\partial p}{\partial x_i} + \frac{\partial \tau_{ij}}{\partial x_j} \tag{3.2}$$

$$\frac{\partial \rho Y_i}{\partial t} + \frac{\partial}{\partial x_j}\left(\rho u_j Y_i\right) = \frac{\partial}{\partial x_j}\left(\rho D_{i,m}\frac{\partial Y_i}{\partial x_j}\right) + R_i \; ; \; i = 1,2, \cdots, N_s \tag{3.3}$$

$$\frac{\partial \rho H}{\partial t} + \frac{\partial}{\partial x_j}\left(\rho u_j H\right) = -\frac{\partial q_j}{\partial x_j} + \mu \Phi_v \tag{3.4}$$

where N_s, ρ, u_i, Y_i, p, R_i, H, q_j, and Φ_v represent the number of species, density [kg/m^3], velocity of components [m/s], mass fraction of species, pressure [Pa], rate of reaction of species [$mol/m^3\text{-}s$], total enthalpy [J/mol], heat flux due to conduction and species diffusion [W/m^3], and viscous dissipation [$N/m^2\text{-}s$], respectively.

B. Numerical Methodology

Computational model development and simulations are performed using a commercial finite element analysis (FEA) tool (Ansys®). The computational model is used to perform a parametric study of the coupled electro – thermo – mechanical analyses of the microcantilever platform used in this study. Proper estimate for the temperature profile of the microcantilevers is a key factor in simulating the response of the nano-calorimeter platform for chemo-mechanical sensing of explosives. However, the thermal response to chemical reactions is not available in the FEA tool (Ansys®). The chemo-mechanical model is formulated for predicting the mechanical deflection for changes in temperature distribution of the bimorph structure. Hence, an electro – thermo – structural model is coupled with a computational fluid dynamics (CFD) model, as shown schematically in Figure 37. The thermal data obtained from the chemical reaction model (using Fluent®) is mapped onto each finite element (FE) node, which serves as the initial condition for the structural dynamics simulation using Ansys®.

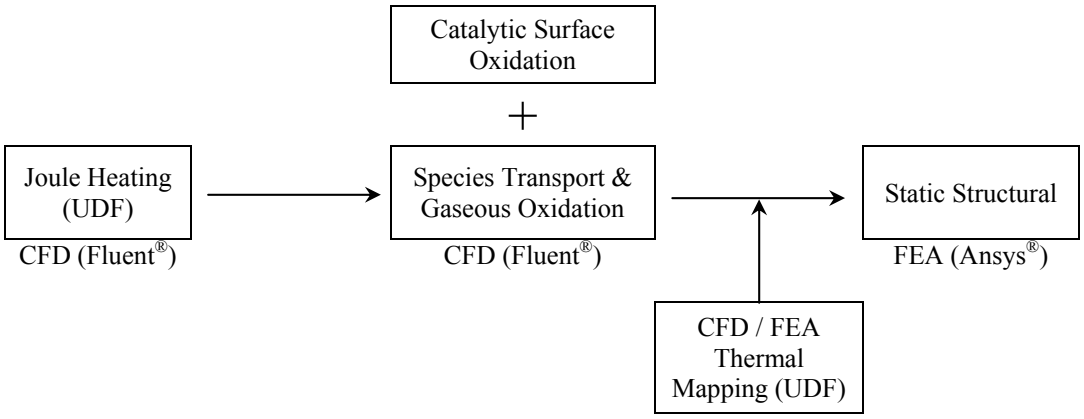

Fig. 37. Schematic of a complete model of an electro-thermally actuated microcantilever.

1. Computational Fluid Dynamics (CFD)

The volumetric generation (q) by electric current through resistive heating element (Joule heating) can be calculated from Ohm's Law as follows:

$$Q = I^2 R = I^2 \rho \frac{l}{A} \quad \rightarrow \quad q = \frac{Q}{V} = \left(\frac{I}{A} \right)^2 \rho \tag{3.5}$$

Fluent® does not provide the solution for joule heating, so we implement the user-defined function (UDF) code into the Fluent® case file. In our UDF code, the electrical conductivity value is defined as the diffusivity of the solid phase potential in the solid zones. Then we perform the thermal analysis for the catalytic oxidation based on species transport and gas phase as well as surface oxidation models.

Numerical simulations were performed based on the 3D, laminar, species transport, gas phase as well as surface reaction, and steady-state simulation techniques. Hexagonal and gradient meshing techniques were used. Figure 38 shows the solid model generated in Gambit® software for thermal analysis using Fluent®.

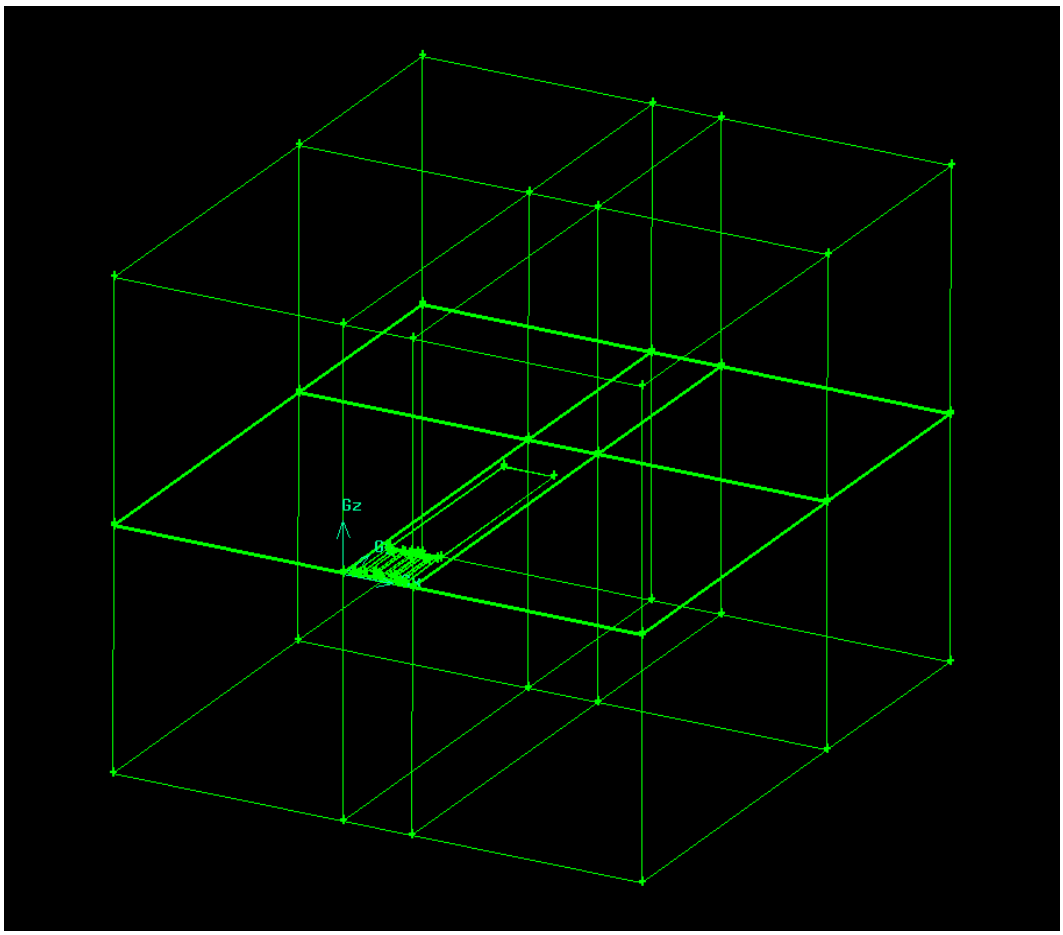

Fig. 38. Geometry of the control volume for simulation.

The thickness of thermal boundary layer (δ_T) (as shown in Figure 39) on natural convection over the heated microcantilever surface is expressed as follows [125]:

$$\delta_T = 0.0014 Ra_\delta^{0.24} \tag{3.6}$$

where Ra_δ is the Rayleigh number which is given by

$$Ra_\delta = Gr \cdot \Pr = \frac{g\beta}{\nu\alpha}(T_s - T_\infty)L^3 \tag{3.7}$$

where *Gr* is the Grashof number, *Pr* is the Prandtl number, *g* is the acceleration [*9.81* m/s^2] due to gravity, β is the thermal expansion coefficient [K^{-1}], T_s is the wall temperature [*K*], T_∞ is the ambient temperature [*K*], *v* is the kinematic viscosity [m^2/s], α is the thermal diffusivity [m^2/s], and *L* is the characteristic length [*m*].

$$L = \frac{Surface \quad area \quad (A)}{Perimeter \quad of \quad the \quad surface \quad (P)} \tag{3.8}$$

For the maximum temperature (e.g., *~580 K*) at the actuation current of *20 mA*, the thermal boundary layer is approximately 200 μm in height. Also, the thickness for other direction is determined by using the same way. For the size of the simulation volume (shown in Figure 38) obtained from the calculation of thermal boundary layer thickness, the convective heat transfer coefficient (*h*) calculated based on the pure conduction correlation (equation 2.9) by Nusselt number (*Nu*) was consistent with value obtained from the experiments (*h = 700* W/m^2*-K*) [73].

$$Nu = \frac{hL}{k} = 1 \tag{3.9}$$

where *L* is the characteristic length [*m*], *L = Volume / Surface Area*, and *k* is the thermal conductivity [*W/m-K*] for the mean temperature, $T_m = (T_s + T_\infty) / 2$.

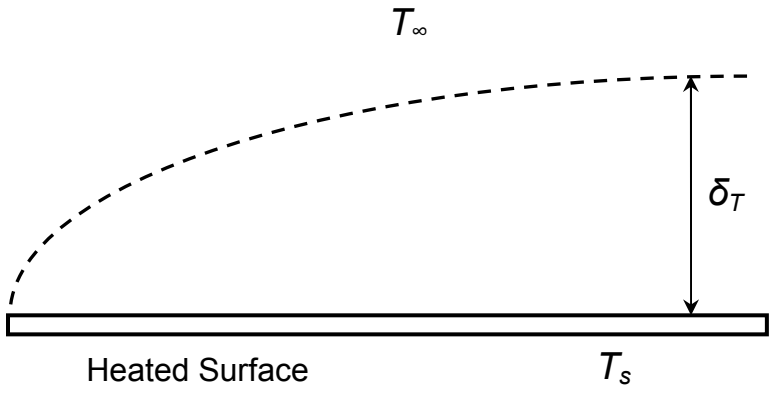

Fig. 39. Schematic representation for thermal boundary layer on natural convection over a horizontal plate.

a. Vapor-Liquid Equilibrium (VLE)

Simulations are performed at a constant gas mole (or mass) fraction in a testing chamber. The vapor-liquid equilibrium (VLE) mole fraction is determined from a vapor pressure at a room temperature (*293.15 K*). The vapor pressure, p_i^{sat}, of each explosive is commonly represented by Antoine equation which is given by:

$$\log p_i^{sat} = A - \frac{B}{T + C} \tag{3.10}$$

Table V shows Antoine Coefficients (*A*, *B* and *C*) used in equation (3.10) and vapor pressures of some VOCs gases predicted by Antoine Equation.

Table V. Antoine coefficients and VLE vapor pressure at room temperature (T is in *Celsius*) [126].

At *273.15 K*	*A*	*B*	*C*	p_i^{sat} [*mmHg*]	y_i
Acetone $(CH_3)_2CO$	*7.23160*	*1277.030*	*237.230*	*184.950*	*0.243*
2-Propanol C_3H_7OH	*8.11820*	*1580.920*	*219.620*	*33.158*	*0.044*

From the given pressure values in Table V, we can calculate the mole fraction of each species using Dalton's law.

$$y_i = \frac{p_i}{p_{total}} \text{ where } p_{total} = \sum_{i=1}^{n} p_i \tag{3.11}$$

b. Chemical Kinetics

The main assumptions for the numerical model are (i) The flow remains laminar during the entire combustion process (Laminar finite-rate model); (ii) Multi-step chemical kinetics in gas-phase (volumetric) and complete (or deep) reaction model in catalytic surface reactions occur with rate constants following the Arrhenius type dependence (equation (1.7)); (iii) Explosives of constant concentrations are presented in the control volume by forming a mixture with air. In Fluent®, concentrations of reactants need to be specified on the basis of mass fractions.

At the constant-pressure processes, the enthalpy of reaction as the difference between the enthalpies of products and the reactants is defined as:

$$\Delta H = H_{products} - H_{reactants} \tag{3.12}$$

The enthalpy of reaction can be positive or negative or zero depending upon whether the heat is gained or lost or no heat is lost or gained:

$$\begin{aligned} &\Delta H > 0, \text{ if } H_{products} > H_{reactants} \text{ endothermic reaction } (\Delta H \text{ is positive [+]}) \\ &\Delta H < 0, \text{ if } H_{products} < H_{reactants}, \text{ exothermic reaction } (\Delta H \text{ is negative [-]}) \\ &\Delta H = 0, \text{ if } H_{products} = H_{reactants}, \text{ no heat is lost or gained } (\Delta H \text{ is zero [0]}) \end{aligned} \tag{3.13}$$

Table VI represents the standard state enthalpy of some products and reactants used in this study.

Table VI. Standard state enthalpy of some gases.

	C_3H_6O	C_3H_7OH	O_2	H_2	H_2O	CO	CO_2
H [$J/kmol$]	-2.19×10^8	-2.73×10^8	0	0	-2.42×10^8	-1.11×10^8	-3.94×10^8

The complete oxidation reaction of VOCs is highly exothermic and the global oxidation models of different gases (that were used for numerical simulations) are summarized in Table VII.

Table VII. Global one-step reaction models of acetone and 2-propanol.

Gases	Combustion Model	Heat of Combustion
Acetone $(CH_3)_2CO$	$(CH_3)_2CO + 4O_2 \rightarrow 3CO_2 + 3H_2O$	*–1761 kJ/mol* (-303.2×10^5 *J/kg*)
2-Propanol C_3H_7OH	$2C_3H_7OH + 9O_2 \rightarrow 6CO_2 + 8H_2O$	*–1907 kJ/mol* (-317.3×10^5 *J/kg*)

The gas phase reaction scheme is based on reports in the literatures. The models were based on *1st* order homogeneous reactive flow proportional to the volumetric concentrations of the species. Basically, in the gas phase reactions of VOCs, hydrogen abstraction leads to the formation of CO_2 or H_2O as a result of deep (or complete) oxidation. Also, especially at low temperatures, VOCs are oxidized to form the intermediate products (i.e. acetone: CO, 2-propanol: CO, C_3H_6 or C_3H_6O). The multiple-step combustion models are listed in Table VIII, and this list provides a more optimized value (as opposed to the "global" one-step reaction model).

Table VIII. Chemical kinetic parameters for gas phase reaction of acetone and 2-propanol ($p = 1\ atm$) [127-129].

Reaction	A_r $[s^{-1}]$	E_r $[J/kmol]$
$C_3H_6O + 2.5O_2 \rightarrow 3CO + 3H_2O$	4.0×10^{14}	2.09×10^{8}
$H_2 + 0.5O_2 \rightarrow H_2O$	7.0×10^{13}	8.79×10^{7}
$CO + 0.5O_2 \rightarrow CO_2$	8.5×10^{12}	8.79×10^{7}
$CO + H_2O \rightleftarrows CO_2 + H_2$	1.0×10^{12} 3.1×10^{13}	1.74×10^{8} 2.05×10^{8}
$C_3H_8O \rightarrow C_3H_6 + H_2O$	1.26×10^{13}	1.06×10^{8}
$C_3H_8O + 0.5O_2 \rightarrow C_3H_6O + H_2O$	1.0×10^{14}	1.05×10^{8}
$C_3H_6 + 4.5O_2 \rightarrow 3CO_2 + 3H_2O$	6.75×10^{9}	1.256×10^{8}

As shown in Figure 5, catalytic oxidation is initiated at much lower activation energy than the values in Table VIII. Everaert *et al.* [130] demonstrated experimentally that the activation energy of VOCs can be correlated as a function of the molecular weight (M). The constants, a and b, are obtained as a curve-fit from the experimental results reported in the literature [131-134].

$$E_r = a \cdot \exp(b \cdot M) = 98.631 \exp(-0.0039M) \tag{3.14}$$

The constants, *a* and *b*, in equation (2.14) vary with different classes of organic compounds [130] or catalyst materials [135]. This equation cannot completely explain the catalysts-dependent properties such as high selectivity in partial oxidation. In general, *Au* shows high selectivity in catalytic oxidation of VOCs [136]; however, the selectivity is decreased with increasing temperature, hence the higher activation energy is required for complete oxidation pathway [131]. In this study, we primarily consider a complete oxidation over the catalysts surface. In the case of 2-propanol, the conversion to acetone is only initiated at lower temperatures, and the deep oxidation process becomes dominant as the temperature increases. Thus, both the partial oxidation to acetone and complete oxidations of acetone and 2-propanol were explored for 2-propanol.

For manganese oxide (Mn_3O_4) catalysts the activation energy, E_s, were reported for the complete oxidation of acetone with the values being *100 ~ 121 kJ/mol* [137], also for Cu-doped ceria catalysts ($Cu_xCe_{1-x}O_y$) E_s lying between *96.5 kJ/mol* and *97.0 kJ/mol* was reported [138]; however, for vanadium pentoxide (V_2O_5) catalysts a significantly smaller value was reported, i.e. 75 ± 8 *kJ/mol* [139]. The gold-based catalysts supported on metal oxides (i.e. Au/Fe_2O_3, Au/CeO_2, Au/TiO_2, or Au/Al_2O_3) have investigated due to its importance in industrial processes and transportation activities [140-142]. The activity of each metal catalyst is quite different [137-143] and literature on complete catalytic oxidation model of acetone over pure *Au* was not available. Thus, the activation energy was estimated from the correlation between the activation energy and activity of VOCs by *Au* catalysts using equation (3.14). For instance, the activation energies of VOCs over *Au* catalysts are *87 kJ/mol* (*61.5 kJ/mol* for partial oxidation) methanol

(CH_3OH) [131-133] and *83.7 kJ/mol* for propene (C_3H_6) [134]. Thus, the activation energy for complete oxidation of acetone over *Au* is assumed to be *78.65 kJ/mol*.

The parameters for complete or partial oxidation of 2-propanol over the metal catalysts have been obtained from various reports [136, 144-149]. In general, the catalytic oxidation of 2-propanol begins with dehydration to yield propene. The formation of the dehydrogenated product (acetone) occurs at low temperature (i.e. *393 K* for *Au/iron* oxide catalysts) [144]. The complete oxidation from acetone (or propene) to carbon dioxide (CO_2) and water vapor (H_2O) occurs at high temperature (i.e. *553 K* for Au/iron oxide catalysts) [146]. However, due to high selectivity of acetone over 2-propanol in pure gold catalytic oxidation process [136], the deep oxidation processes of 2-propanol to carbon dioxide as well as via acetone (red box in Figure 40) are considered in this study.

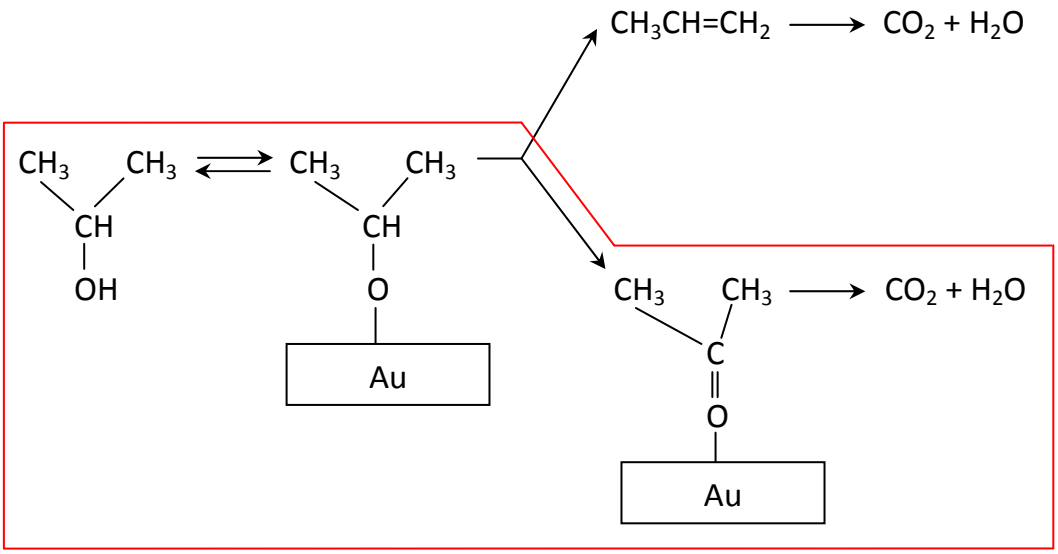

Fig. 40. Schematic of reaction scheme for selective oxidation of 2-propanol to acetone over the gold catalysts.

The activation energy for the partial oxidation of 2-propanol is reported for a value of *1.6 kJ/mol* [136]. The surface reaction of VOCs and the corresponding chemical kinetics parameters are listed in Table IX. Thus, both processes that are listed in Table IX are applied for the oxidation of 2-propanol.

Table IX. Chemical kinetic parameters for surface reaction of acetone and 2-propanol.

Reaction	A_s $[s^{-1}]$	E_s $[J/kmol]$
$C_3H_6O + 4O_2 \rightarrow 3CO_2 + 3H_2O$	4.19×10^{10}	7.865×10^{7}
$C_3H_7OH + 4.5O_2 \rightarrow 3CO_2 + 4H_2O$	3.54×10^{10}	7.802×10^{7}
$C_3H_7OH + 0.5O_2 \rightarrow C_3H_6O + H_2O$	4.40×10^{1}	1.6×10^{6}

Catalysts are substances which accelerate chemical reactions without being consumed. Catalysts change the reaction rates by offering a different path or mechanism for the reaction (as mentioned earlier in Chapter I). Catalysts change the speed of reaction. However, they do not affect the equilibrium. As written in equation (1.7), the reaction rate is the function of the pre-exponential factor and the activation energy. The pre-exponential factor, A_s, is usually determined by experimental measurements. Three approaches (i.e. Collision theory, Collision theory combined with empirical data, and Activated Complex Theory) of A_s for VOCs oxidation have been previously presented

[130, 135]. Since the Activated Complex Theory was reported to be consistent with the experimental results [130, 135], this theory is used for the proposed study. The theory is expressed as:

$$A_s = e^n \frac{k_B T}{h} \exp\left(\frac{\Delta S}{R}\right) \quad [s^{-1}] \tag{3.15}$$

where k_B is the Boltzmann constant (1.38×10^{-23} *J/K*), T is the temperature [*K*], h is the Planck constant (6.6256×10^{-34} *Js*), ΔS is the activation entropy [*J/mol-K*], R is the ideal gas constant (*0.082051 atm/mol-K*), e is the Euler-number (*2.7183*), and n is the number of molecules participating in the reaction. For catalytic reactions, ΔS should be negative (i.e. *-20 ~ -60 J/mol-K* for acetone and 2-propanol [135]) because of the immobility of the chemisorbed complex [130, 135]. Values of ΔS can be determined from the experimental results. Finally, for the complete oxidation of Acetone and 2-propanol equation (3.15) is used for this study, and A_s for partial oxidation of 2-propanol is the value by the experiments.

2. Finite Element Analysis (FEA)

The Computational Fluid Dynamics (CFD) tool provides a powerful and flexible numerical framework for modeling fluid flow and performing associated convection heat transfer calculations, but does not have built-in advanced solid mechanics analysis capabilities for performing thermo-mechanical stress analysis. On the other hand, the Finite Element Analysis (FEA) tool provides the advanced solid mechanics analysis

capabilities. To calculate the mechanical deflection by the thermal stress at the surface of microcantilevers, UDF code for CFD/FEA thermal mapping was implemented into Fluent® calculation. The limitation of this approach is that the meshing and scaling of the models needs to be consistent in both Fluent® and Ansys®, as shown in Figure 41.

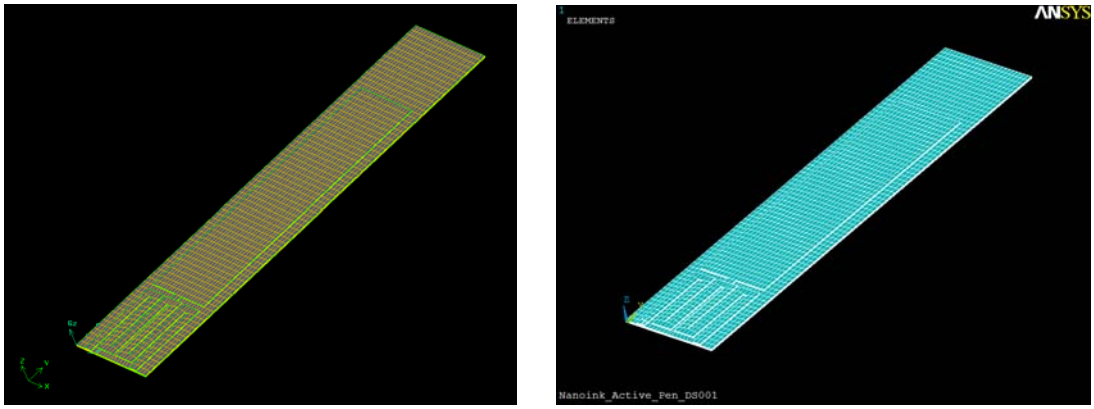

Fig. 41. Solid model of microcantilever in (LEFT) Gambit® and (RIGHT) Ansys®.

C. Temperature Dependent Properties

The temperature dependence of physical constants and thermo-chemical properties is considered to obtain more accurate estimate for the results. The property values are obtained from various reports or from the Fluent® database (which relies on a NIST database) [150] for source information. The effective mass diffusion coefficient, $D_{eff,i}$, is computed using equation (3.16).

$$D_{eff,i} = \frac{1 - y_i}{\sum_{j \neq i}^{\forall_j} \frac{y_j}{D_{ij}}} \tag{3.16}$$

The binary mass diffusivity, D_{ij}, is calculated by using the relationships of Reid *et al*. [151]. The methodology is based on the Chapman-Enskog theoretical description of a binary mixture of gases at low to moderate pressures. In this theory, the binary diffusion coefficient for the species pair *i* and *j* is given by equations (3.17).

$$D_{ij} = \frac{0.0266T^{3/2}}{pM_{ij}^{1/2}\sigma_{ij}^{2}\Omega_D} \tag{3.17}$$

$$M_{ij} = 2[M_i^{-1} + M_j^{-1}]^{-1} \tag{3.18}$$

$$\sigma_{ij} = (\sigma_i + \sigma_j)/2 \tag{3.19}$$

$$\Omega_D = \frac{1.06036}{(T^*)^{0.15610}} + \frac{0.19300}{\exp(0.47635T^*)} + \frac{1.03587}{\exp(1.52996T^*)} + \frac{1.76474}{\exp(3.89411T^*)} \tag{3.20}$$

$$T^* = k_B T/(\varepsilon_i \varepsilon_j)^{1/2} \tag{3.21}$$

where p is the pressure [Pa], T is the temperature [K], M *is* the molecular weight [g/mol], σ is the species molecular diameter [$\mathring{A}$], Ω_D is the collision integral, and T^* is the dimensionless temperature. Table X lists the values of hard-sphere collision diameter as well as Lennard-Jones energy for various species involved in the calculations.

All thermo-physical properties such as specific heat, dynamic viscosity, and thermal conductivity are assumed to be temperature dependent. The physical property values are summarized in Appendix I. The viscosity of gas mixture is determined using the kinetic theory of gases,

$$\mu_i = \frac{y_i \mu_i}{\sum_{j \neq i}^{\forall_j} y_i \phi_{ij}} \tag{3.22a}$$

where φ_{ij} and μ_i are given by

$$\phi_{ij} = \frac{\left[1 + \left(\frac{\mu_i}{\mu_j}\right)^{1/2} \left(\frac{M_j}{M_i}\right)^{1/4}\right]^2}{\left[8\left(1 + \frac{M_i}{M_j}\right)\right]^{1/2}} \tag{3.22b}$$

$$\mu_i = 2.67 \times 10^{-6} \frac{\sqrt{M_i T}}{\sigma_i^{\,2} \Omega_{\mu,i}} \tag{3.22c}$$

The thermal conductivity of gas mixture is determined from the thermal conductivity of each of the individual gases in the mixture using the ideal gas mixing law.

$$k_i = \frac{y_i k_i}{\sum_{j \neq i}^{\forall_j} y_i \phi_{ij}} \tag{3.23}$$

Table X. Hard-sphere collision diameter and Lennard-Jones energy parameter for each species [150, 152-153].

Species	σ [$\AA$]	ε / k_b [K]
H_2	*2.827*	*59.7*
H_2O	*2.641*	*809.1*
N_2	*3.798*	*71.4*
O_2	*3.467*	*106.7*
CO	*3.690*	*91.7*
CO_2	*3.941*	*195.2*
C_3H_6	*4.807*	*248.9*
C_3H_6O	*4.670*	*443*
C_3H_8O	*4.937*	*393.42*

CHAPTER IV

EXPERIMENTAL CONFIGURATION

A. Experimental Apparatus

In this study, two different techniques were used to measure the deflections of microcantilevers, namely: (i) projection-screen method and (ii) optical lever method (as shown in Figure 42). The experimental setup consists of an air-tight acrylic chamber, a platform to support and control the movement of the laser, a platform for the microcantilever beam, and a piece of paper (or position sensitive detector: PSD) to mark the location of (or detect) the reflected laser beam spot.

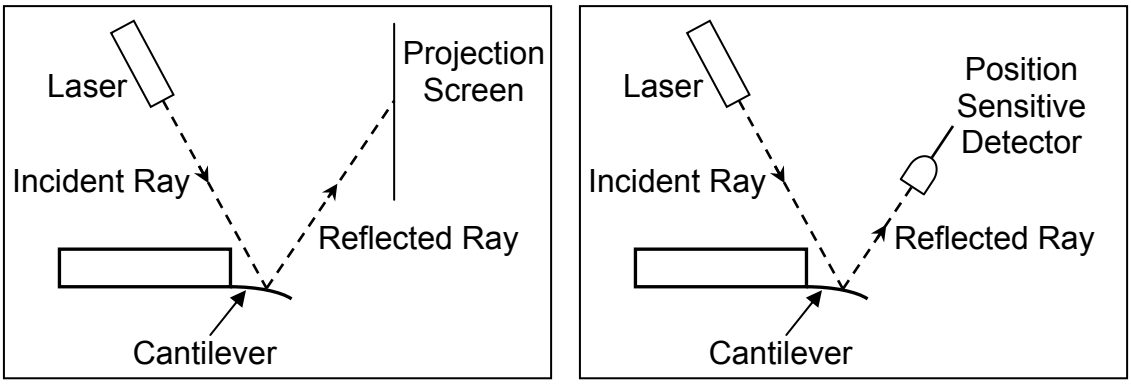

(a) (b)

Fig. 42. Schematic of the experimental apparatus (a) projection-screen method (b) optical detection method.

The experimental apparatus is placed inside an environmental control chamber, which is constructed from rectangular acrylic walls with a hinged door made from ½" thick acrylic sheets as shown in Figure 43. In order to render the chamber airtight, silicone was used to seal the edges inside the box and a tape insert was used to seal the edges along the exterior of the box. Weather-stripping was used as a sealant between the door and the front wall of the chamber. Inside the chamber, a low-power laser (*1 mW*, *635 nm*) was affixed to a semi-automated stage with *4* axes of motion (assembled from Newport components). The Newport stage system (Figure 43) supports the laser and can be actuated remotely for laser beam alignment with the cantilever axes in the nano-calorimeter apparatus. In addition to altering the position of the laser, the remote control can also be used to rotate the cantilever array within the *xy*-plane. Hence, laser alignment and cantilever positioning can be accomplished without disturbing the chamber environment.

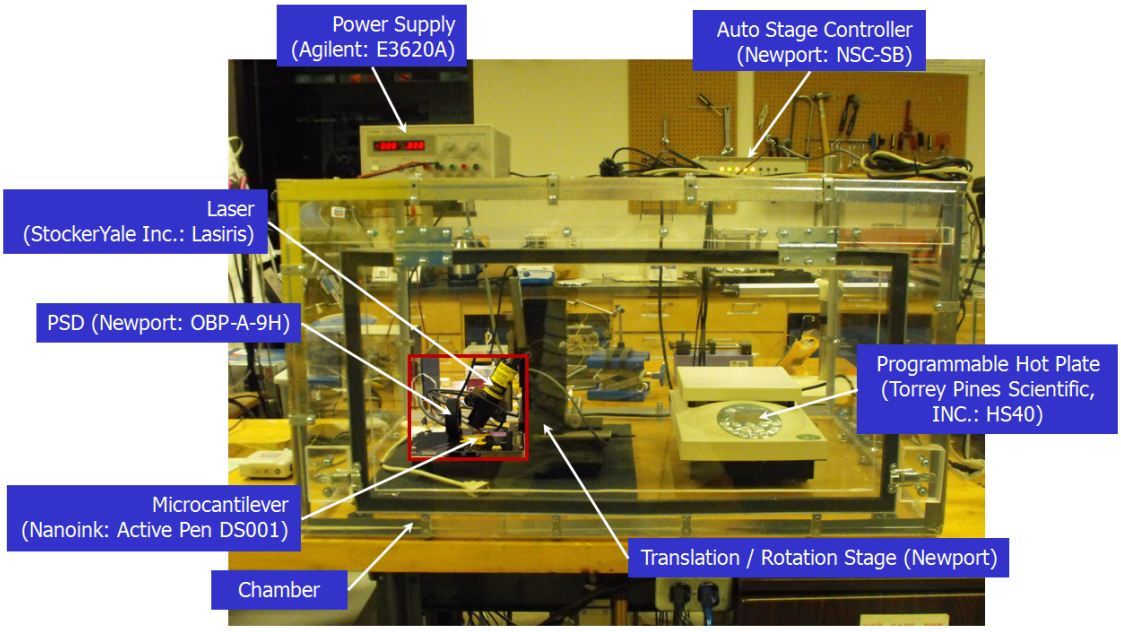

Fig. 43. Experimental appratus based on the optical-detection method for explosive detection.

B. Experimental Procedure

Each experiment was performed in two separate steps: a control experiment (baseline) was performed in ambient atmospheric conditions, and a second experiment was performed in the presence of the explosive vapor at equilibrium vapor concentration. The deflection response of the microcantilever (as a function of actuation current) in uncontaminated air environment was compared to that of air saturated with the explosives vapor. As shown in Figure 42, the laser beam incident on the microcantilever surface is reflected by the gold coating on to the screen (paper) or PSD. The actuation current (for heating the microheaters and therefore for actuating the microcantilever beam) is increased from *0* to *20 mA* at *2 mA* intervals. It was observed that at actuation current values exceeding *20 mA* - the bending response diverged from the control experiments. For each *2 mA* increment, the resulting deflection of the microcantilever beam is tracked by measuring the location of the laser beam spot reflected on the screen (paper) attached to the chamber wall or voltage values corresponding the position from PSD. The deflection is expected to be proportional to the change in the location of the reflected laser spot, which is measured by calculating the difference in vertical location of the laser spot centroid from a reference position (in this case, the laser beam position at *0 mA* actuating current). The resistance of the gold filament is also recorded for each value of the actuation current. Once the data is collected for the control experiment, the liquid explosive is poured into a small bowl and placed inside the chamber. The liquid remains in the chamber for approximately thirty

minutes to ensure saturation conditions are established for explosive vapor. Subsequently, the experiment is repeated in the presence of the vapor samples. The results are then recorded and compared to the results obtained from the control experiments.

C. Measurement Uncertainty

The change in deflection angle of the microcantilevers is measured as a function of actuation current. The total experimental error (percentage) in measuring the angle is given by [57]:

$$\frac{\delta\theta}{\theta} = \sqrt{\left(\frac{\delta y}{y}\right)^2 + \left(\frac{\delta L}{L}\right)^2} \tag{4.1}$$

where θ is the deflection angle [*degrees*], y is the change in height [m] from the reference point on the screen (or PSD), and L is the distance [m] from the cantilevers to the projection screen (or PSD) and $\delta\theta$ is the error in the calculation of the deflection angle. The experimental error for measuring the change in angular deflection was found to be less than *0.5 %*.

CHAPTER V

RESULTS AND DISCUSSION

A. Base Line

The FEA results for the thermal deformation are based on the thermal history during metal film deposition (as shown in Figure 44). Both models show similar trends and are consistent with the FEA results. At low temperature, the FEA results are more consistent with Lee's model [68]. However, as the temperature is increased, the FEA results are more consistent with Hsueh's model [67]. This response is usually characterized by the geometrical factors, material properties and most importantly, temperature variations during heating treatment [67-68].

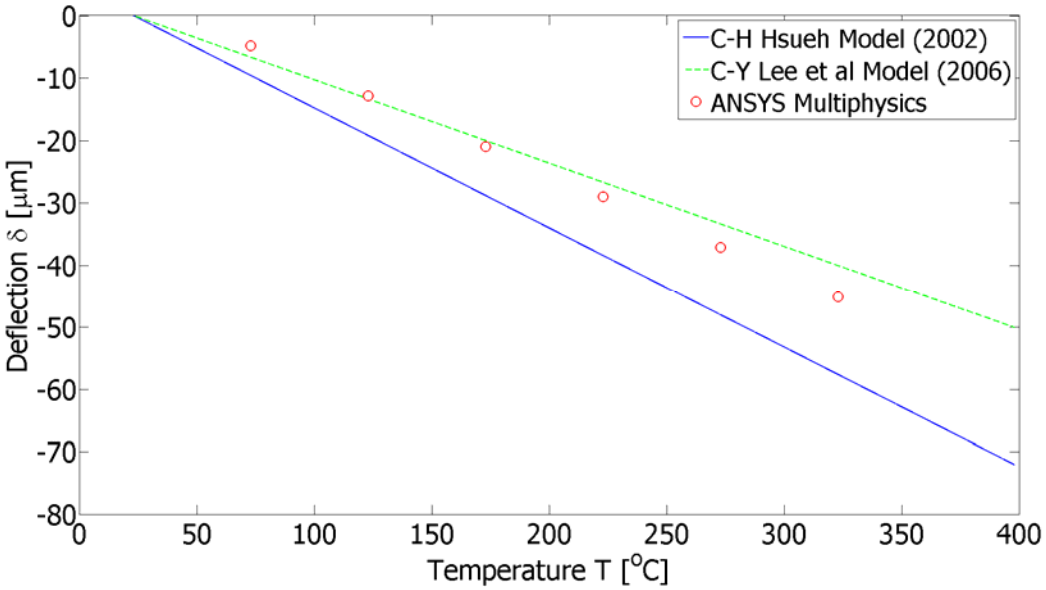

Fig. 44. Comparison on variations in free end deflection during heat treatment.

In this study, we analyzed only thermally induced stress and excluded intrinsic stress values (that can arise from defects and impurities incorporated in the material). The deflection due to residual stress is generated when metal layers with different thermal expansion coefficient are thermally bonded. Hence, for application of the theoretical models only the length (e.g. *122 μm*) corresponding to the area where *Au* thin-film is deposited was considered.

The thermal deformation that exceeds the elastic limit cannot be completely reversed to the original status (even at room temperature). The estimation of initial deflection due to residual stress is shown in Figure 45(a). Since the stress distribution through the thickness is not significant, the average residual film stress is calculated by [67]

$$\bar{\sigma}_f = \frac{1}{t_f}\int_0^{t_f} \sigma_f dz = \frac{E_s E_f t_s \left(E_s t_s^{\,3} + E_f t_f^{\,3}\right)\left(\beta_s - \beta_f\right)\Delta T}{E_s^2 t_s^4 + E_f^2 t_f^4 + 2E_s E_f t_s t_f \left(2t_s^2 + 2t_f^2 + 3t_s t_f\right)} = -1.1025\times 10^8\ Pa \qquad (5.1)$$

where σ_f is defined as the mismatch between elastic stress ($E\varepsilon$) and thermal stress ($\beta\Delta T$). As shown in Figure 45(a), the negative stress causes the microcantilever deflection to be inverted. After calculating the initial deflection, subsequently deflection values are estimated from the electro-thermal-structural coupling simulations. Figure 45(b) shows the resultant deflections of the microcantilever for an actuation current of *20 mA*. Since the deflection by thermal actuation occurs in the reverse direction (of the deflection due to residual stress). The total deflection can be defined as the sum of deflections due to residual stress and thermal stresses.

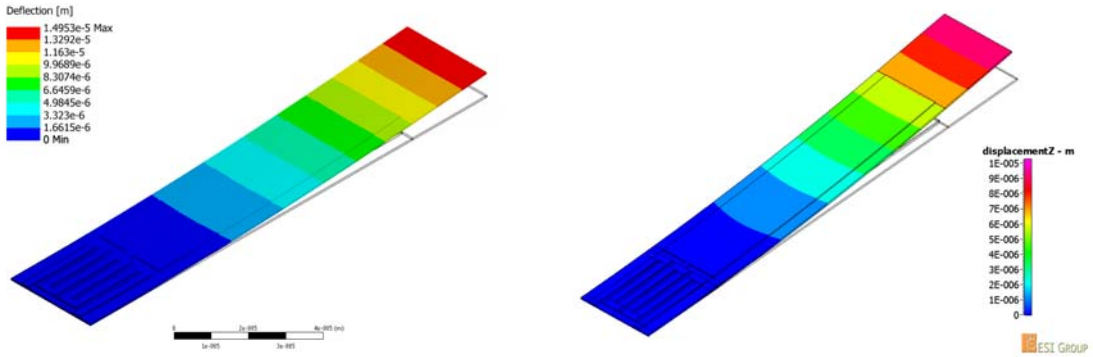

Ansys® Multiphysics ESI CFD-ACE+®

(a)

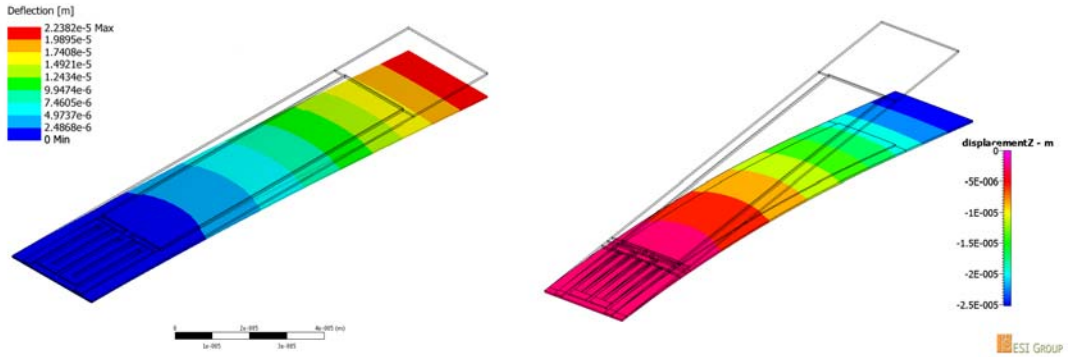

Ansys® Multiphysics ESI CFD-ACE+®

(b)

Fig. 45. Deflection of bimorph microcantilever occurred due to thermal-actuation for an actuation current of *20 mA*. Total deflection (Ansys®-*37.335 μm* / ESI CFD-ACE+®-*35.45 μm*) is determined by the sum of deflections by residual stress and thermal actuation. (a) Initial deflection due to residual stress (b) Final position due to thermal actuaction.

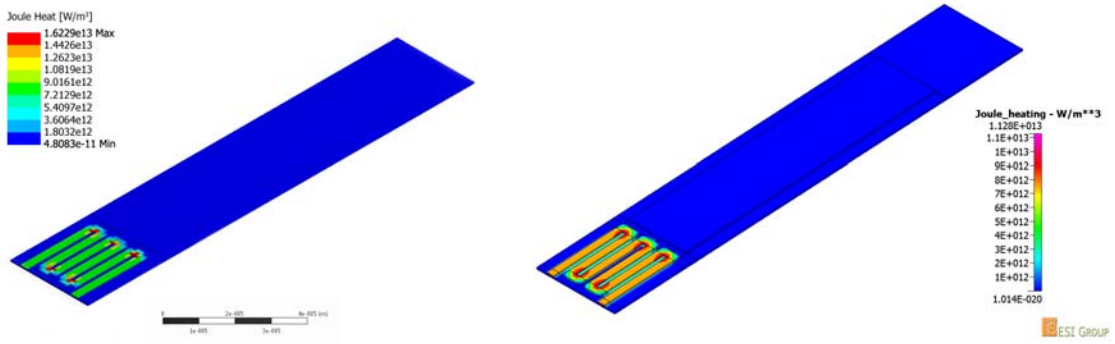

Ansys® Multiphysics ESI CFD-ACE+®

(a)

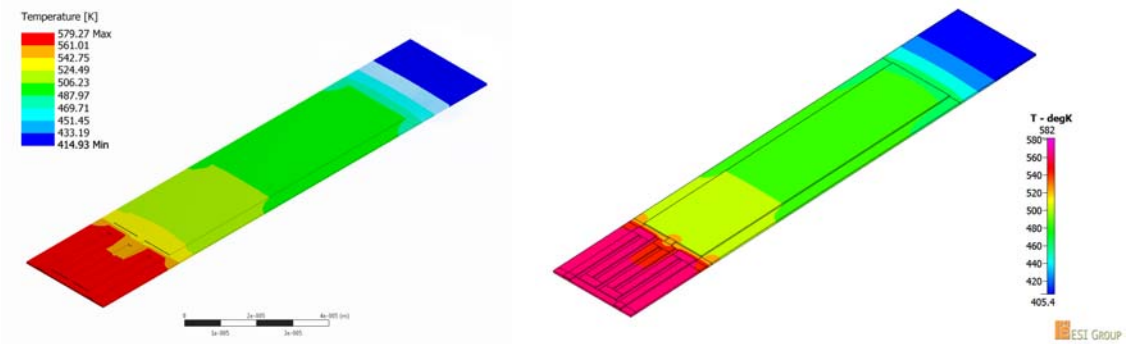

Ansys® Multiphysics ESI CFD-ACE+®

(b)

Fig. 46. (a) Joule heating and (b) temperatue profile of thermal-actuated birmorph microcantilever (actuation current = *20 mA*).

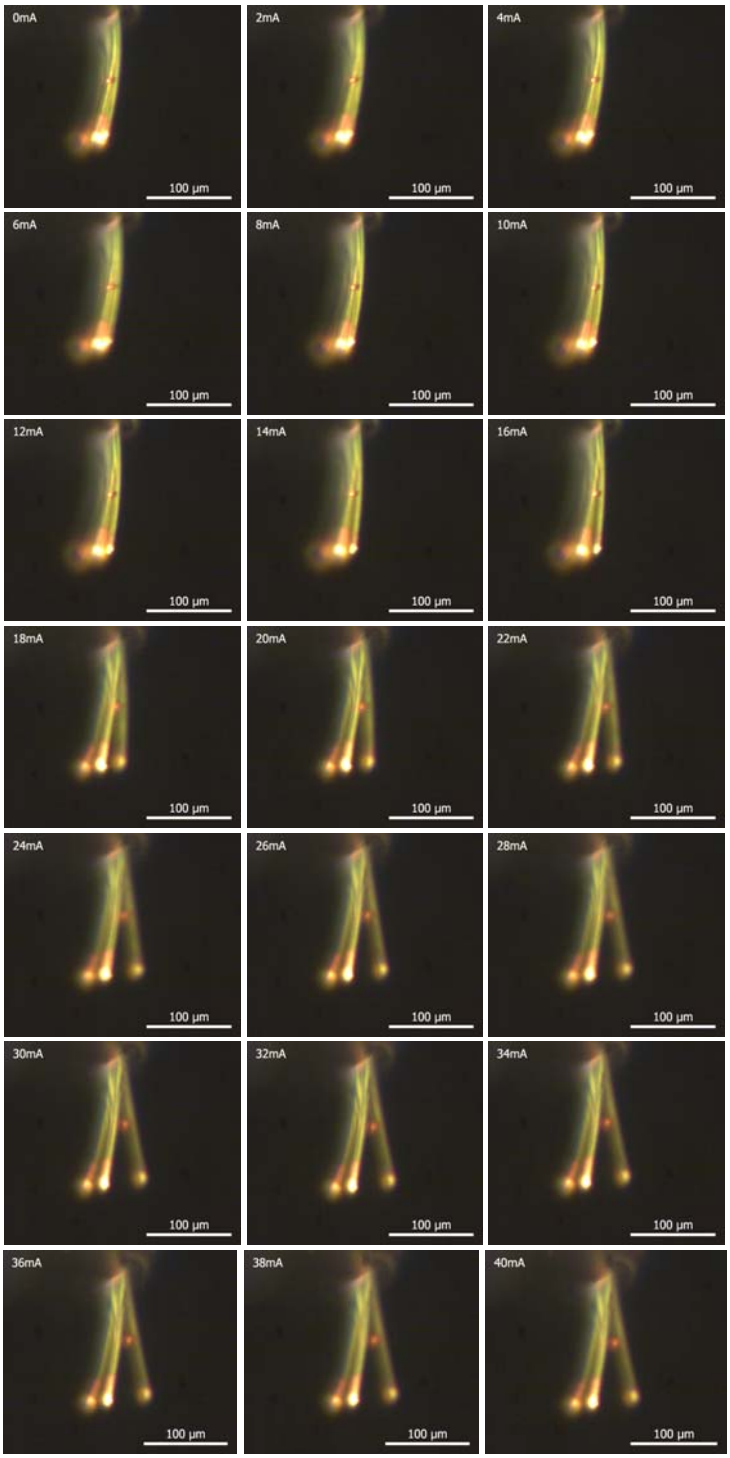

Fig. 47. Flexural motions of bimorph microcantielvers thermally activated by electrical current (*0 mA ~ 40 mA*).

Figure 46(a) shows the heat generation from the resistive heating element of thin gold film type for an actuation current of *20 mA*. As shown in Figure 46(b), for the actuation current of *20 mA*, the microcantilever is heated to *580 K*. Also, it was demonstrated that the temperature distribution within the microcantilever is not uniform. This is due to the convective heat transfer coefficient ($h = 700\ W/m^2\text{-}K$ [73]) that is imposed in these calculations. Moreover, the theoretical model does not account for the temperature dependence of resistivity for the *Au* heating element. The nominal resistance value that is used in the theoretical model, given by equation (1.20), is *21 Ω*. This value was measured using multi-meter, for the micro-heater device.

To ascertain the validity of applying the FEA model for estimating the microcantilever deflection, the results are plotted for comparison with the analytical model (proposed by Jiang *et al.* [72]) and the experimental data obtained from this study (as shown in Figure 47). Figure 45 represents the thermal-induced deflection due to bimetallic effect, which is simulated based on the temperature profile, as shown in Figure 46(b). For actuation current below *~25 mA*, the numerical predictions are consistent with experimental data with errors within *10 %*. However, for the current exceeding *25 mA*, theoretical and numerical model did not agree with the experimental results. This disagreement can be explained from the data sheet provided by the manufacturer (NanoInk Inc., Skokie, IL). According to the technical manual for the Active Pen array (Model#: *DS001*), the optimum actuation current is *~20-25 mA*. For actuation currents exceeding *35 mA*, the Active Pen™ can be damaged irreversibly. In addition, since the analytical and numerical models follow the linear characteristics,

these cannot completely account for non-linear behaviors of over-heated micro structures. The simulation results of two commercial multiphysics tools were almost identical. However, the results predicted by ESI CFD-ACE+® were found to be more consistent with the experiments for higher actuation currents (as shown in Figure 48).

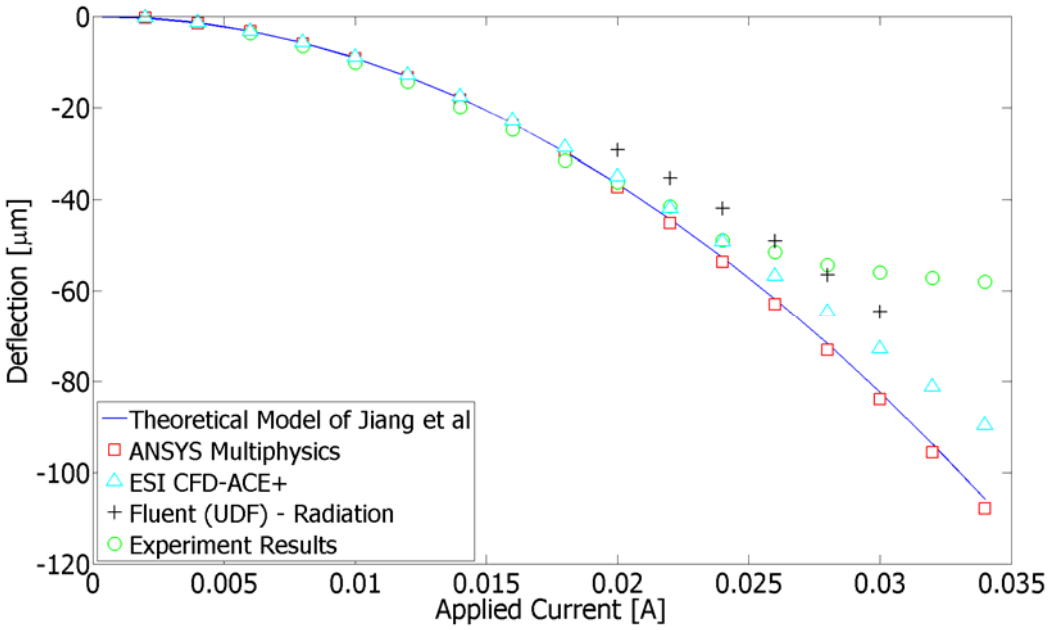

Fig. 48. Comparison of deflection among FEA model (Ansys® and ESI CFD-ACE+®), theoretical model, and experimental data.

In addition, to investigating the radiation effect, the radiation model in Fluent®, P_1 mdole, has been used for solving the radiative flux. From the results shown in Figure 48, the radiation effect could not completely compensate for the difference between the predictions and the measurments. The thermo-mechanical properties of each metal layer in Table II are used for this calculation.

B. Bending Response Due to Thermal Actuation

1. Numerical Analysis

Before performing simulations using the multi-step reaction model and temperature dependent properties, the preliminary simulations were performed to verify the theoretical model. In this calculation, the global one-step oxidation model of propane (C_3H_8) is adopted for the simplicity of the calculations. The chemical kinetics such as activation energy and rate constant are obtained from Hayes *et al.* [61] as follows:

$$k_v = 5.0\times10^9 \exp\left(\frac{8.98\times10^7}{T}\right) \ [kmol/m^3\text{-}s] \tag{5.2}$$

$$k_s = 2.4\times10^5 \exp\left(\frac{8.98\times10^7}{T}\right) \ [kmol/m^2\text{-}s] \tag{5.3}$$

The results also help to provide confidence for the Governing Equations used in the CFD code. The concentrations profiles over the heated surface are shown in Figure 49. In the 1D model, the temperature differences for the same heights level are similar. Hence, the concentrations of explosive vapor are assumed to vary with the height. Nevertheless, the predictions by theoretical calculation were found to be in agreement with the results obtained from the CFD models.

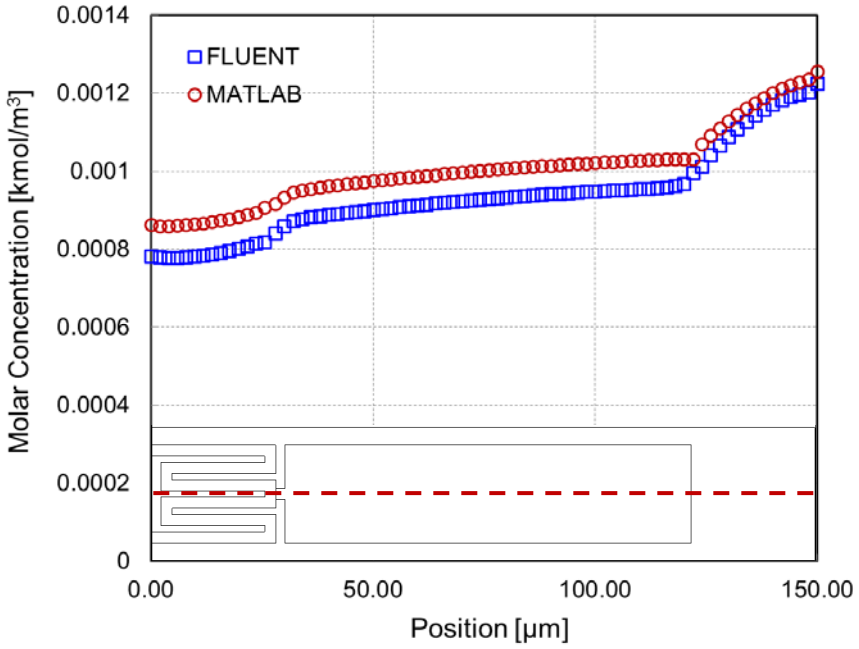

Fig. 49. Concentration profile over the microcantilever surface in the logitudinal direction.

Oxidation of Volatile Organic Compounds (VOCs) in air is numerically explored for specific values of initial concentrations within the control volume. The chemical kinetics is expressed in an Arrhenius form (equation 1.7) and is used to model the temperature dependence of reaction rate as well as activation energy for oxidation. The higher surface area to volume ratio at the nano-scale is expected to expedite the kinetics of the area-limited catalytic reactions, which means the chemical reactions only occur on the catalyst surface provided by the gold coatings on the microcantilevers [58]. The catalytic reaction on the surface of the microcantilevers depends on the core temperature of the heating element. Figure 50 shows the surface temperature range of electrically

pre-heated microcantilevers in air. These results can be easily obtained from the electro-thermo coupling simulation in Ansys® or ESI CFD-ACE+®.

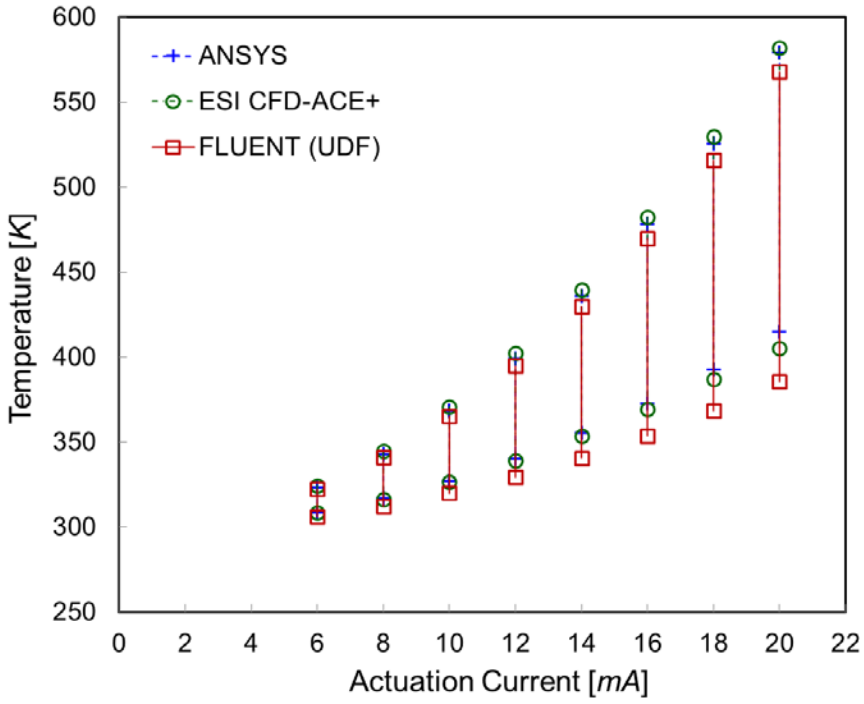

Fig. 50. Temperature range of microcantilever heated in air.

However, to estimate the variations of surface temperature after oxidation on the pre-heated catalyst surface, the mass and heat transfer equations along with chemical species equations as well as resistive heating should be solved simultaneously. Since the mapping of temperature data from Ansys® to Fluent® is not supported, the UDF code for resistive heating was implemented in the chemical reaction model. To verify the UDF code, temperature profile was calculated by UDF for Ohmic-heating in Fluent® along with the calculations for electro-thermo multiphysics in Ansys® and ESI CFD-ACE+®.

Figure 51 represents the comparison of numerical simulation when three different simulation tools were used for the actuation current of *20 mA*. In this simulation, the values for geometrical and material properties of microcantilevers are summarized in Table II. As shown in Figure 50 and 51, the numerical results using Fluent®, Ansys®, and ESI CFD-ACE+® demonstrated almost identical temperature distribution over the cantilever surface.

Complete oxidation of VOCs proceeds with the formation of oxidation products carbon dioxide (CO_2) and water vapor (H_2O) as summarized in Table VII. The initial conditions for concentration and the enthalpy for phase change are listed in Table V and Table VI, respectively. Since the oxidation reactions of explosives are highly exothermic, (as shown in Figure 52 and 53) the surface temperature is increased by the presence of heat generation that is occurs due to the oxidation reactions. Accordingly, the microcantilevers demonstrate a downward bending response, as shown Figure 52. Finally, the change in surface temperature due to combustion of VOCs contributes to the differences in deflections caused by the bimetallic effect.

Figure 53 shows the simulation results for the bending response as a function of actuation current. Since the evaporation pressure of acetone is higher than that of 2-propanol, it is observed that the effects of the oxidation was more pronounced in the case of acetone. Accordingly, the surface temperature increased due to oxidation is more significant in acetone. Figure 53 also shows the surface temperature of microcantilevers obtained from the simulations for the nano-scale combustion reactions.

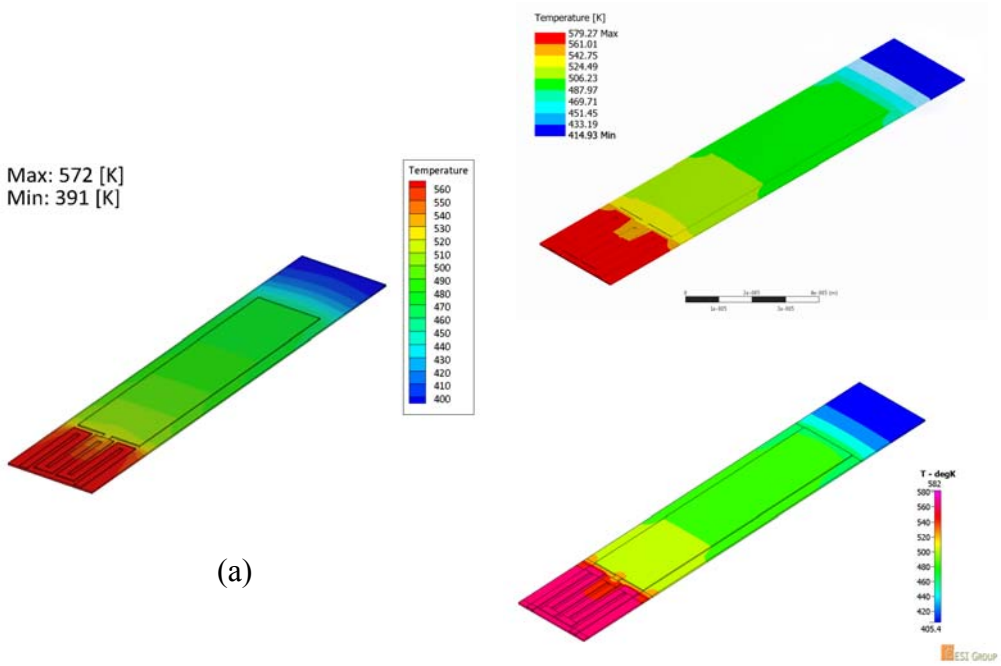

(a)

(b)

Fig. 51. Temperature profile of bimorph microcantilever due to ohmic-heating (a) UDF in Fluent® (b) Multiphysics in (Top) Ansys® and (Bottom) ESI CFD-ACE+®.

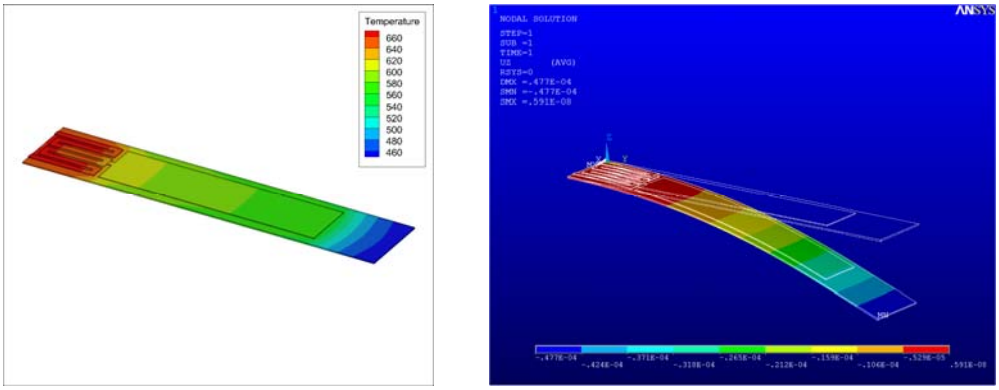

(a)

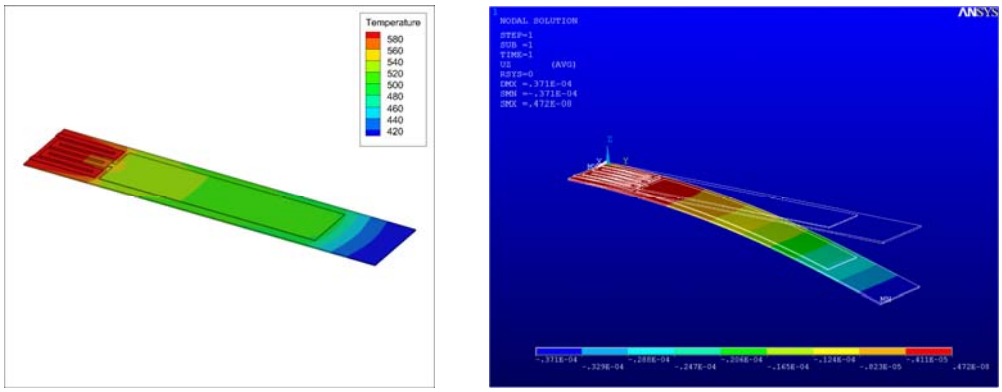

(b)

Fig. 52. Surface temperature profile by nano-scale combustion reactions on the surface of the microcantilevers and bending response caused by bimetallic effect at *20 mA* (a) Acetone (b) 2-Propanol.

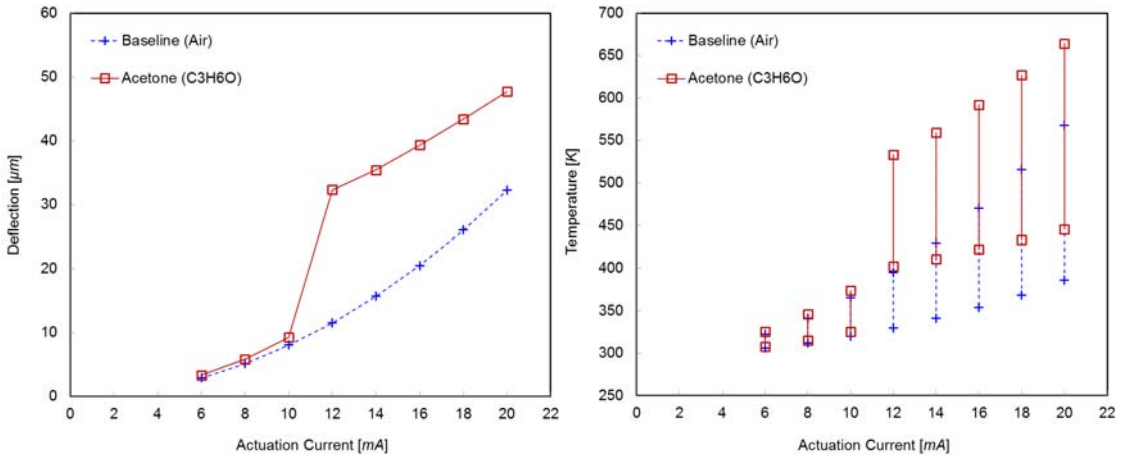

(a)

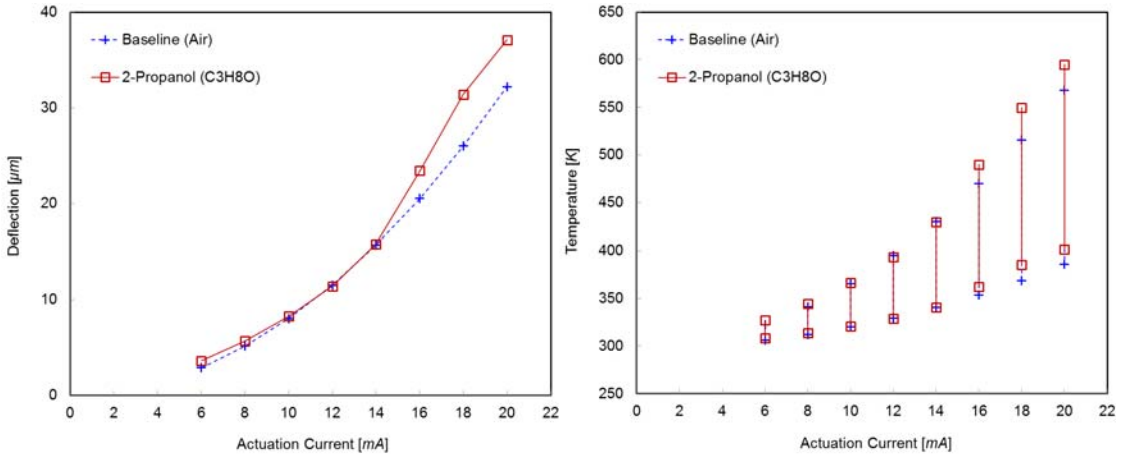

(b)

Fig. 53. Simulation of the resultant deflection and temperature changes due to nano-scale combustion at the actuation current of from *6 mA* to *20 mA* (a) Acetone (b) 2-Propanol.

Figure 54 shows the concentration profiles for reaction products for catalytic oxidation of acetone and 2-propanol over the microcantilevers for an actuation current of *20 mA*. At the applied current of *20 mA*, as shown in Figure 51(a) the maximum surface temperature is *572 K*, which is below the ignition temperature (e.g. acetone: *738 K*/ 2-propanol: *672 K*) that is reported for macro-scale combustion devices. So, during the oxidation of acetone and 2-propanol complete oxidation products such as CO_2 and H_2O are formed - as well as intermediate products such as *CO* are formed due to partial oxidation. In addition, the numerical analysis was performed to find the effect of sensor performance on the variations of concentrations of explosives. At room temperature , the constant saturation concentrations are listed in Table V. Those values are obtained for saturated air mixture in the control volume.

Acetone has a relatively high evaporation pressure compared with 2-propanol. So, the mole fraction (i.e. *0.243*) of acetone in binary mixture of air and explosives is much higher than that of 2-propanol (i.e. *0.044*). The amount of gas comsumed for oxidation is proportional to the concentrations over the surface which are assumed as the constant value, initially. Therefore, the change in temperature by oxidation is more vigourous in acetone as expected; however, the mixture of air and acetone can be regarded as a richer mixture (lower air-fuel ratio: AFR), which makes the reacton to be diffusion controlled. As shown in the right hand side of Figure 54, the case of reduced concentrations in acetone demonstrates the bigger temperature change due to higher AFR. But, since the mixture of air and 2-propanol is lean, the surface temperature is decreased when the concentrations of reactants are reduced by a factor of two.

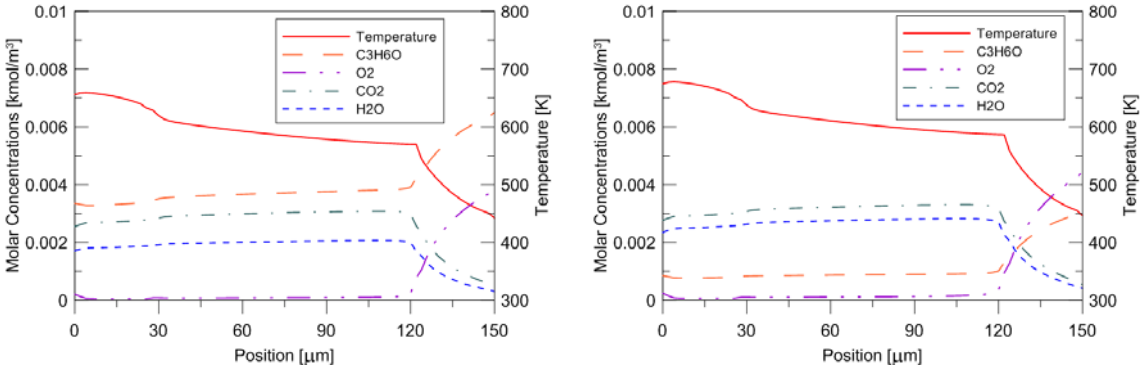

(a)

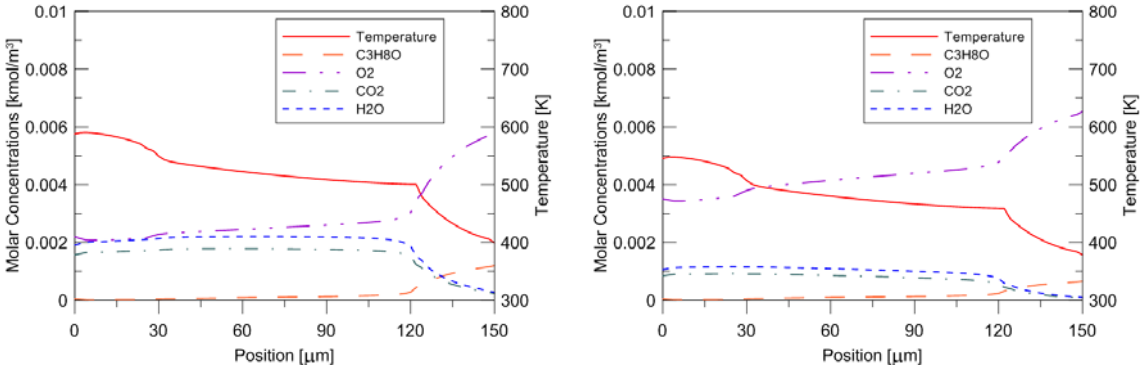

(b)

Fig. 54. Surface coverage and wall temperature in different mole fractions (or concentrations) (a) Acetone (Explosive : Air = (LEFT) *0.243* : *0.598* and (RIGHT) *0.122* : *0.694*) (b) 2-Propanol (Explosive : Air = (LEFT) *0.044* : *0.756* and (RIGHT) *0.022* : *0.773*).

2. Experimental Results

The nano-calorimeter was tested by performing experiments using different explosive materials (e.g. acetone and 2-propanol) as the sources for pure vapor. Figure 55 and Figure 56 show the results for the change in height of the reflected beam as a function of actuation current. The experimental results are achieved using both detection methods (i.e. projection screen method and optical lever method) supposed in this study. The trends observed from the results show that at a specific value of actuation current the change in deflection deviates from the control experiments (performed in air). This is identified as the threshold value which is used for uniquely detecting the combustible material. However, the threshold current value depends on various factors such as vapor pressure (or concentrations) of the combustible vapors, chemical kinetics (i.e. activation energy and rate constant), and ignition temperature. Figure 55 represents the comparison of the change in position of the reflected light on the projection screen between explosives and air.

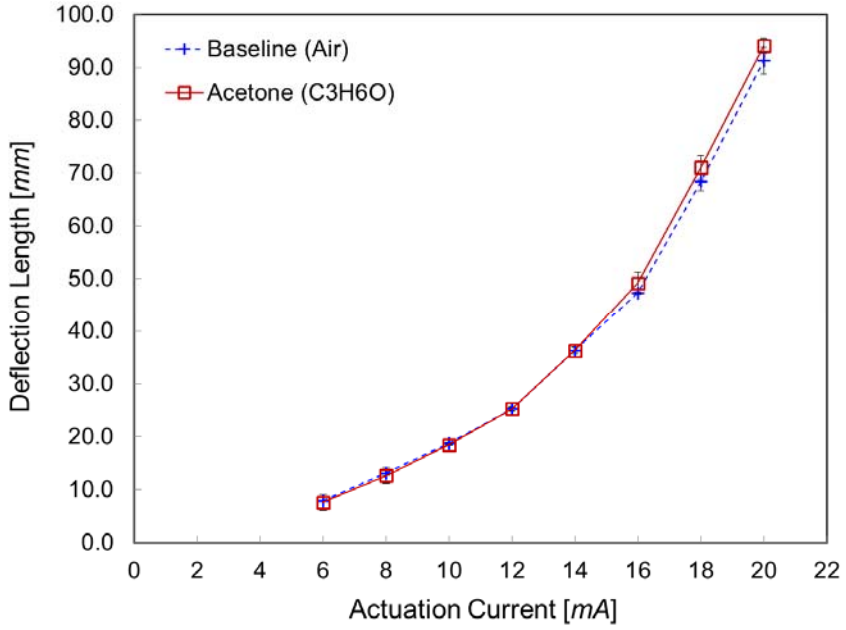

(a)

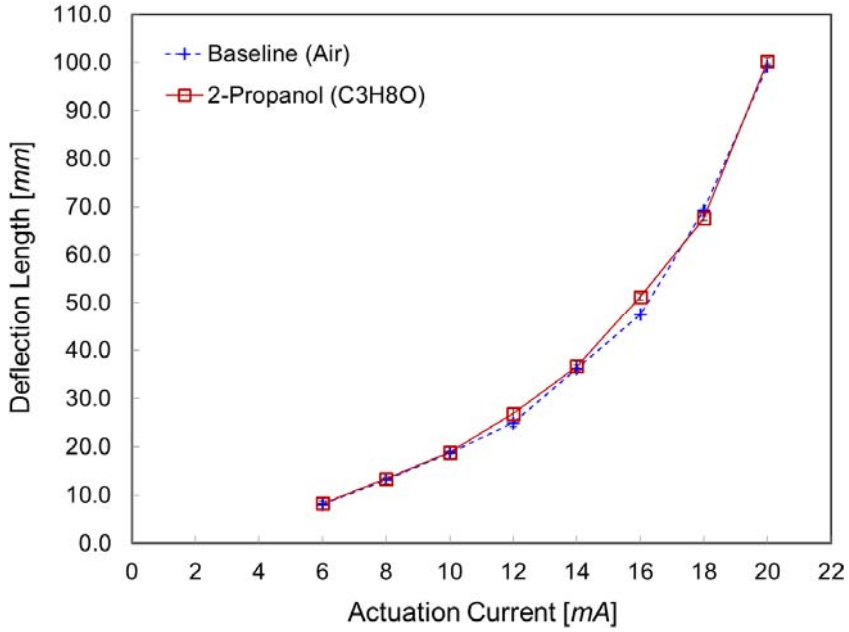

(b)

Fig. 55. Experimental results of microcantilever deflection based on projection screen method in explosive sensing (a) Acetone (Self Ignition Temperature = *738.15 K*) (b) 2-Propanol (Self Ignition Temperature = *672.15 K*).

In general, in the low current region the microcantilever bending response in the presence of the combustible vapors is almost the same as that of air. As the actuation current is increased, the temperature of the bimorph microcantilever structure is increased causing additional bending of the beam. Thus, the incident laser ray is reflected from the microcantilever and begins to deflect upwards causing the reflected light beam to move upwards. That is because the ignition temperatures of most combustible vapors are higher than the ambient temperature; furthermore, the presence of the vapor causes more vigorous oxidation on the surface of the microcantilever at elevated temperatures (caused by the higher actuation current). As shown in Figure 55(a), the cantilever bending response matched the control experiments for actuation currents up to *~14 mA*. This is compatible with my numerical analysis as well as the results of Nelson *et al.* [57]; on the other hand, the case of 2-propanol is more complex due to its chemical characteristics in thermal oxidation. A small divergence in response was observed for low actuation currents (e.g. $< 6\ mA$). However, this value was not depicted in the experimental results based on the projection screen method. The possible reason is that this method has the limitations in detecting small difference of deflections. Also, this difference is within the ranges of the experimental uncertainty. Figure 56 represents the measurement results based on PSD method, for which the output voltage corresponding to the change in position of reflected light is monitored using PSD. The values are obtained by averaging three times measurements for each actuation current value. In addition, measured signals obtained by using an oscilloscope are listed in Appendix C.

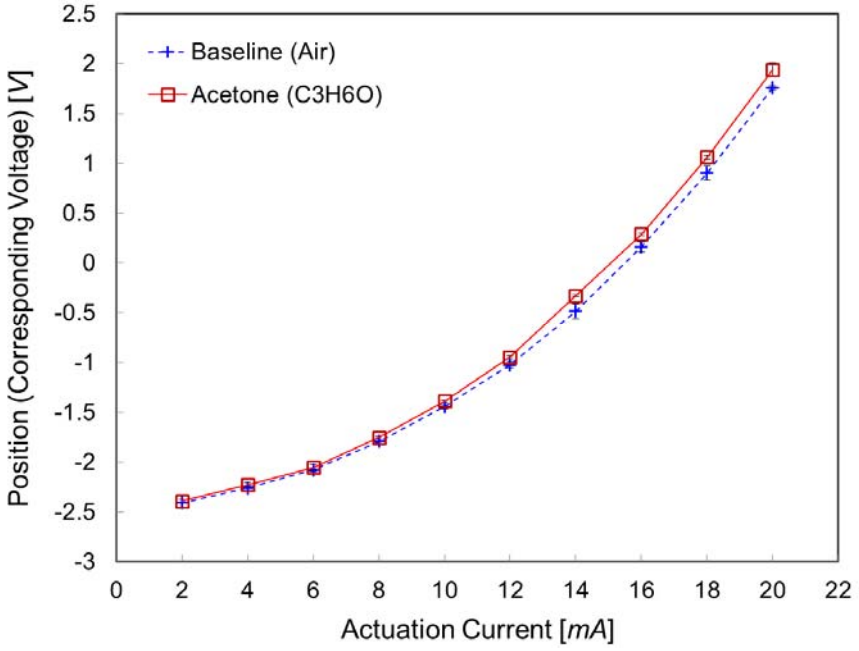

(a)

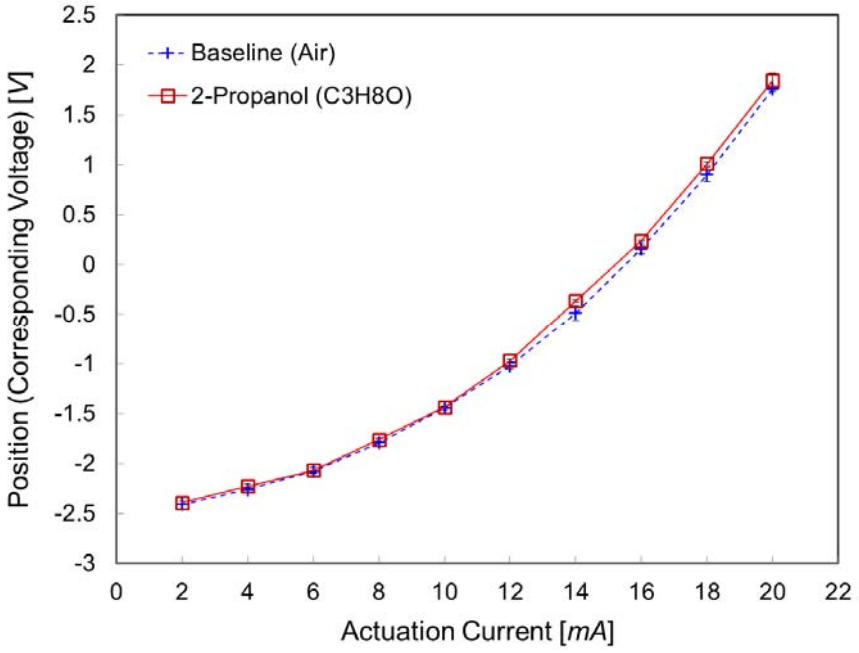

(b)

Fig. 56. Experimental results of microcantilever deflection based on optical lever method in explosive sensing (a) Acetone (b) 2-Propanol.

The PSD method affords higher precision (as opposed to the projection screen method) even for small differences in deflection values. In the case of acetone, similar trends are observed as with the predictions by numerical analysis and the measurements by projection screen method. The deflections diverge as the temperature (or actuation current) increases. Also, in the case of 2-propnaol, the response to the conversion from 2-propanol to acetone at room temperature (i.e. *0 mA* actuation current) as well as thermal oxidation of 2-propanol at higher actuation currents were observed in this method. However, in the experiment using the microcantilever involving carbon nano-structures, the experimental evidence showing the enhancement in sensitivity compared with the clean one are not found in this study (The results are almost the same with those shown in Figure 56). This is because the CNTs are not existed on the cantilever surface where the heat transfer with surroundings dominates.

In addition, since acetone and 2-propanol are highly volatile, their ignition temperatures as well as vapor pressures are key factors for predicting the threshold current. On the other hand, for solid explosives (e.g. TNT, Ammonium Nitrate, RDX, and Picramic Acid), the threshold current can be estimated only from the self-ignition temperature due to their low evaporation pressures (or concentrations in air). The vapor pressures of acetone and 2-propanol are summarized in Table V. The response to chemical reaction is more pronounced at the lower temperature region than the self-ignition temperature value due to higher volatility. The vapor pressure (*186 mmHg*) of acetone is much higher than that (*33 mmHg*) of 2-propanol. However, the catalytic surface reaction of 2-propanol can be activated at lower surface temperature (or

actuation currents) since the activation energy of 2-propanol for initializing the oxidation is lower than that of acetone; in other words; the combustion reaction of acetone requires higher energy (or temperature). Nevertheless, at higher surface temperature, the sensitivity for 2-propanol was quite low due to low concentrations (vapor pressure) and formation of water vapors. It is observed that the deflection characteristics in VOCs show the same tendency (downward bending response) from both the numerical and experimental results.

3. Sensitivity Analysis

The sensitivity analysis that was performed in Chapter I provides the design guidelines for the microcantilever-based sensor. In real operation, the sensitivity can be evaluated as the ratio of input values and output results. In other words, the sensitivity is calculated based on the change in the deflection in relation to the electrical actuation. Equation (5.4) [154] implies the change of sensitivity for each explosive as a function of the actuation current.

$$Sensitivity(S) = \frac{output \quad change}{load} = \frac{\Delta z / z}{I} \tag{5.4}$$

From the results shown in Figure 57, the optimum operating current can be defined as the current value that enables higher sensitivity. The specific current region (i.e., from *14 mA* to *20 mA* or from *6 mA* to *8 mA*) can provide higher sensitivity for acetone and 2-propanol vapors. The sensitivity of the microcantilever sensor used in this study was

obtained as $0.052 \pm 0.047\ mA^{-1}$ for acetone and $0.011 \pm 0.014\ mA^{-1}$ for 2-propanol. These results can vary with the different design parameters of the microcantilever (e.g., length, width, thickness, or elastic properties) or different chemical properties (e.g., enthalpy of reaction or concentration).

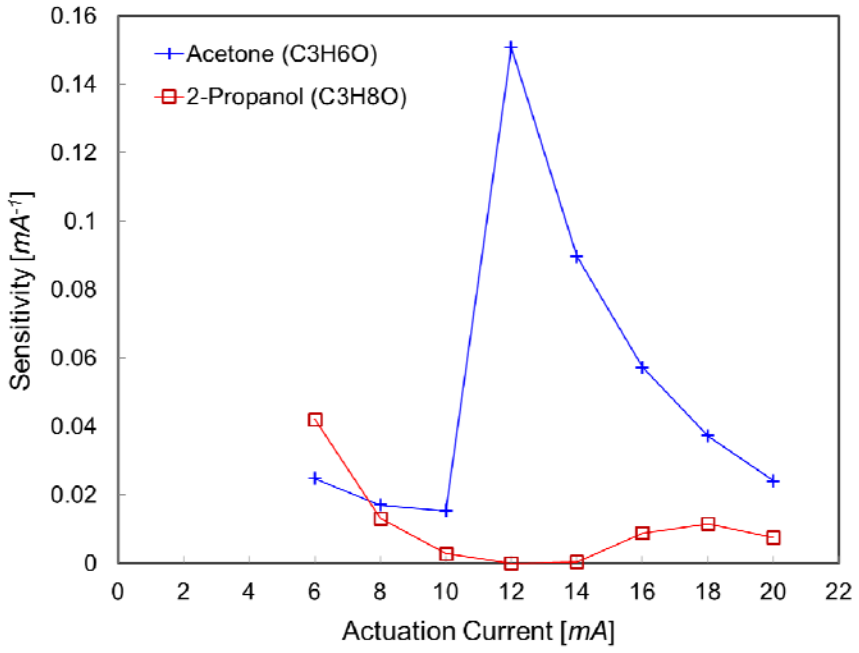

Fig. 57. Actuation current dependence of sensitivity for microcantilever-based sensor.

4. Manufacturing Tolerance Effect

The micro-fabrication based on photo-lithography is excellent for achieving small absolute tolerances as opposed to material removal by machining. Nevertheless, the substantial geometrical variations for microcantilevers fabricated with MEMS processing technologies (e.g., Photolithography) can significantly affect the performance of the sensor. In this study, the effect of manufacturing tolerances on the bending response is numerically investigated. The tolerance values summarized in Table XI are based on information received from the manufacturer (NanoInk, Inc., Skokie, IL).

The variations due to manufacturing tolerance are subject to the geometrical variations (e.g., absolute values of deflections) rather than depending on the chemical properties. So, the numerical analysis is performed for only acetone vapor, which provides enough information to evaluate the effect of manufacturing tolerance. The results from the numerical analysis are summarized in Table XI. The results demonstrate that the geometrical variations do not affect the detection of explosives. However, small variations in sensor response (compared with the total variations in the presence of explosives vapor) can be caused due to manufacturing tolerance.

Table XI. Change in bending response due to manufacturing tolerance.

Parameters	Manufacturing Tolerance	Change in bending response (Δz_{dif}) for the actuation current of *20 mA* ($\Delta z_{dif} = \Delta z_{explosives} - \Delta z_{air}$)		
Length	*± 2 μm* (*± 1.3 %*)	*± 0.48 μm* (*± 2.68 %*)		Heater Size (+10 %)
			Length (*+2 μm*)	*-0.74 μm* (*-4.11 %*)
Thickness	*N/A*	-	Length (*-2 μm*)	*-1.64 μm* (*-9.09 %*)
				Heater Size (-10 %)
Heater Size	± 10 %	*-1.2 μm* (*- 7.74 %*) *1.1 μm* (*7.1 %*)	Length (*+2 μm*)	*1.78 μm* (*9.89 %*)
			Length (*-2 μm*)	*0.75 μm* (*4.18 %*)

5. Humidity Effect

The screening or identification of explosives based on electrochemical detection is not affected by the relative humidity (RH) which can cause the change in resistance or capacitance of electric components [155]. However, the sensitivity to VOCs decreases with increasing humidity [156]. The relative humidity (RH) is the ratio of the actual water vapor pressure (p_w) to the saturation water vapor pressure (p_{sw}) [157].

$$RH = \frac{p_w}{p_{sw}} \times 100 \ [\%] \tag{5.5}$$

where

$$p_{sw} = 610.78 \times \exp\left(\frac{17.2694 \times T}{T + 238.3} \right) \ [Pa] \tag{5.6}$$

From the results shown in Table XII, it was observed that the variations in surface temperature under the high humidity environment are not significant. However, since the humidity dependence of the electrical property of bimetallic components is not considered in this study, the effect of resistance variations due to humidity on Joule heating was not explored.

Table XII. Change in bending response due to relative humidity in air (Top: acetone/ Bottom: 2-propanol).

RH	Temperature distribution for the actuation current of *20 mA*	Note
40 %	*443.9 ~ 661.7 K* *396.9 ~ 585.3 K*	When RH = *0 %*, *T = 445.1 ~ 664.2 K*
60 %	*444.1 ~ 661.9 K* *397.4 ~ 586.2 K*	When RH = *0 %*, *T = 401.6 ~ 595.1 K*
80 %	*444.1 ~ 661.8 K* *397.3 ~ 586.0 K*	

CHAPTER VI

SUMMARY AND FUTURE DIRECTIONS

A. Summary and Conclusion

In this study the static response of a microcantilever in the presence of explosive or combustible vapors were characterized experimentally and by performing numerical simulations. Also, the bending characteristics of a bi-layer microcantilever, parametric study for optimized operation as well as nano-coatings of high thermal conductivity materials for enhancing the sensitivity were investigated. These results demonstrate the advantages and response characteristics of bimorph microcantilever as the sensing platform for energetic materials.

To explore the bending response to explosive vapors, the change in deflection of the microcantilevers caused by bimetallic effect was measured in both air saturated with explosive vapor and uncontaminated air as a function of the actuation current. From the results, it was found that the specific actuation current value (i.e., threshold value) causing the deflection deviated from the value measured in the absence of explosive vapors depends on explosive materials. (e.g., acetone $\sim= 12\ mA$ and 2-propanol $\sim= 14\ mA$). Therefore, these values can be used for identifying the specific explosives.

Additionally, the numerical analysis was performed based on electro-thermo-mechanical coupling model by using UDF in Fluent® and Ansys®. The consistency between theoretical calculation and CFD simulation for global one-step chemical

kinetics of propane demonstrates the reliability of CFD results. The simulation results showed similar trends with the experimental results for monitoring the bending response of the microcantilever sensors as a function of the actuation current.

- There was no response to acetone vapor at lower actuation currents (e.g., *0 mA ~ 10 mA*). However, as the actuation current value is increased, the deflection deviated from the baseline (i.e., values measured in air) was observed at the specific actuation current value (i.e., *12 mA*).
- The response to 2-propanol vapors occurs at lower actuation current (as the response to conversion of 2-propanol to acetone - *6 mA ~ 10 mA*) as well as higher actuation current (as the response to complete oxidation of 2-propanol over the catalysts - *16 mA*).

The predictions from the numerical simulations provide insights about the fundamental interactions between various transport mechanisms responsible for the observed behavior of the thermally actuated microcantilever array, such as effect of manufacturing tolerance and humidity on the responsiveness and effect of chemical kinetics or vapor concentrations on threshold current value. Also, numerical models offer the guideline for design optimization of microcantilevers.

In conclusion, the feasibility of implementing the proposed bimorph microcantilever-based nano-calorimeter sensing platform for detection of energetic materials was demonstrated in this study. The predictions from the numerical models for

the various transport mechanisms coupled with the chemical reactions for the combustion reactions were validated experimentally.

B. Future Directions

The predictions from the numerical models can be validated experimentally by using other combustible materials and explosive materials. In the aspect of numerical analysis, chemical kinetics for other materials can be explored by experimental or numerical approaches. Moreover, to clearly verify the response to the materials with low volatility (e.g., Ammonium Nitrate, Ammonium Picrate, TNT, RDX, Picric Acid, Picramic Acid, and EGDN as listed in Appendix D), additional measurements can be performed by experimentally controlling the species concentrations of these analytes.

Also, the robust recipe for obtaining stable coating of CNTs on the microcantilever surface can be explored. In addition, the experiments can be repeated by using different sizes or kinds of nano-structured metal catalysts to find the optimum parameters at different operating temperatures for the growth (and coating) of CNTs on the microcantilever surface.

Ultimately, this approach can be implemented into a portable detection platform or integrated instrument for remote monitoring and real-time detection of explosives. For this purpose, miniaturization of optoelectronics platform is essential. Also, since the operation in the real situation is quite different compared with the experimental conditions in the laboratory (e.g., clean and optimized environment inside the chamber),

additional apparatus (e.g., fine meshed screen) is required to prevent false positive alarms that are likely to be triggered in harsh operating environment (such as for low vapor pressure or dust). In addition, optimization of the geometry of micro-heater and microcantilever can enable the application of the sensor platform for a wide range of energetic materials as well as obviate the false-positives/ false-negatives by enhancing the statistical confidence of the results. Alternatively, individual microcantilevers can be designed in an array for the highest sensitivity to particular analytes and for enhancing the specificity of the sensor array for desired analytes.

REFERENCES

[1] Grandke, T. and Ko, W.H., 1989, *Sensors: A Comprehensive Survey – Vol. 1 Fundamentals and General Aspects*, VCH, Weinheim, Germany.

[2] Torrijo, L.G.V., 2006, "Development of Cantilevers for Biomolecular Measurements," Ph.D. Thesis, Universitat Autònoma de Barcelona, Cerdanyola del Vallès, Spain.

[3] Petersen, K.E., 1982, "Silicon as a Mechanical Material," Proc. IEEE, **70**(5), pp. 420-457.

[4] Yinon, J., 2003, "Detection of Explosives by Electronic Noses," Anal. Chem., **75**(5), pp. 98A-105A.

[5] Lavrik, N.V., Sepaniak, M.J., and Datskos, P.G., 2004, "Cantilever Transducers as a Platform for Chemical and Biological Sensors," Rev. Sci. Instrum., **75**(7), pp. 2229-2253.

[6] Li, M., Tang, H.X., and Roukes, M.L., 2007, "Ultra-sensitive NEMS-based Cantilevers for Sensing, Scanned Probe and Very High-Frequency Applications," Nat Nanotechnol., **2**, pp. 114-120.

[7] Lang, H.P. and Gerber, Ch., 2010, *Handbook of Nanophysics: Nanomedicine and Nanorobotics – Nanomechanical Sensors for Biochemistry and Medicine*, 1st Edition, CRC Press, Boca Raton, FL, USA.

[8] Lang, H.P., Hegner, M., and Gerber, Ch., 2005 "Cantilever Array Sensors," Mater. Today, **8**, pp. 30-36.

[9] Baller, M.K., Lang, H.P., Fritz, J., Gerber, Ch., Gimzewski, J.K., Drechsler, U., Rothuizen, H., Despont, M., Vettiger, P., Battiston, F.M., Ramseyer, J.P., Fornaro, P., Meyer, E., and Guntherodt, H.-J., 2000, "A Cantilever Array-based Artificial Nose," Ultramicroscopy, **82**, pp. 1-9.

[10] Lang, H.P., Ramseyer, J.P., Grange, W., Braun, T., Schmid, D., Hunziker, P., Jung, C., Hegner, M., and Gerber, Ch., 2007, "An Artificial Nose Based on Microcantilever Array Sensors," J. Phys.: Conf. Ser., **61**, pp. 663-667.

[11] Lang, H.P., Baller, M.K., Berger, R., Gerber, Ch., Gimzewski, J.K., Battiston, F.M., Fornaro, P., Ramseyer, J.P., Meyer, E., and Guntherodt, H.J., 1999, "An Artificial Nose Based on a Micromechanical Cantilever Array," Anal. Chim. Acta, **393**(1-3), pp. 59-65.

[12] Vashist, S.K., 2007, "A Review of Microcantilevers for Sensing Applications," Nanotechnology, **3**, pp. 1-15.

[13] Gimzewski, J.K., Gerber, Ch., Meyer, E., and Schlittler, R.R., 1994, "Observation of a Chemical Reaction Using a Micromechanical Sensor," Chem. Phys. Lett., **217**(5-6), pp. 589-594.

[14] Pinnaduwage, L.A., Gehl, A.C., Allman, S.L., Johansson, A., and Boisen, A., 2007, "Miniature Sensor Suitable for Electronic Nose Applications," Rev. Sci. Instrum., **78**, pp. 055101-1-4.

[15] Battiston, F.M., Ramseyer, J.-P., Lang, H.P., Baller, M.K., Gerber, Ch., Gimzewski, J.K., Meyer, E., and Guntherodt, H.-J., 2001, "A Chemical Sensor

Based on a Microfabricated Cantilever Array with Simultaneous Resonance-Frequency and Bending Readout," Sens. and Actuators, B, **77**, pp. 122-131.

[16] Fadel, L., Lochon, F., Dufour, I., and Francais, O., 2004, "Chemical Sensing: Millimeter Size Resonant Microcantilever Performance," J. Micromech. Microeng., **14**, pp. S23-S30.

[17] Wachter, E.A. and Thundat, T., 1995, "Micromechanical Sensors for Chemical and Physical Measurements," Rev. Sci. Instrum., **66**(6), pp. 3662-3667.

[18] Singamaneni, S., McConney, M.E., LeMieux, M.C., Jiang, H., Enlow, J.O., Bunning, T.J., Naik, R.R., and Tsukruk, V.V., 2007, "Polymer-silicon Flexible Structures for Fast Chemical Vapor Detection," Adv. Mater., **19**, pp. 4248-4255.

[19] Raiteri, R., Grattarola, M., Butt, H.-J., and Skladal, P., 2001, "Micromechanical Cantilever-based Biosensors," Sensor. Actuat. B-Chem., **79**, pp. 115-126.

[20] Moulin, A.M., O'Shea, S.J., and Welland, M.E., 2000, "Microcantilever-based Biosensors," Ultramicroscopy, **82**, pp. 23-31.

[21] Khaled, A.-R.A., Vafai, K., Yang, M., Zhang, X., and Ozkan, C.S., 2003, "Analysis, Control and Augmentation of Microcantilever Deflections in Bio-Sensing Systems," Sensor. Actuat. B-Chem., **94**, pp. 103-115.

[22] Berger, R., Delamarche, E., Lang, H.P., Gerber, Ch., Gimzewski, J.K., Meyer, E., Guntherodt, H.-J., 1997, "Surface Stress in the Self-Assembly of Alkanethiols on Gold," Science, **276**, pp. 2021-2024.

[23] Wu, G.H., Datar, R.H., Hansen, K.M., Thundat, T., Cote, R.J., and Majumdar, A., 2001, "Bioassay of Prostate-Specific Antigen (PSA) Using Microcantilevers," Nat. Biotechnol., **19**(9), pp. 856-860.

[24] Fritz, J., Baller, M.K., Lang, H.P., Rothuizen, H., Vettiger, P., Meyer, E., Guntherodt, H.J., Gerber, Ch., and Gimzewski, J.K., 2000, "Translating Biomolecular Recognition into Nanomechanics," Science, **288**(5464), pp. 316-318.

[25] Fritz, J., Baller, M.K., Lang, H.P., Strunz, T., Meyer, E., Guntherodt, H.J., Delamarche, E., Gerber, Ch., and Gimzewski, J.K., 2000, "Stress at the Solid-Liquid Interface of Self-Assembled Monolayers on Gold Investigated with a Nanomechanical Sensor," Langmuir, **16**(25), pp. 9694-9696.

[26] Thundat, T., Finot, E., Hu, Z., Ritchie, R.H., Wu, G., and Majumdar, A., 2000, "Chemical Sensing in Fourier Space," Appl. Phys. Lett., **77**(24), pp. 4061-4063.

[27] Hansen, K.M., Ji, H.F., Wu, G.H., Datar, R., Cote, R., Majumdar, A., and Thundat, T., 2001, "Cantilever-based Optical Deflection Assay for Discrimination of DNA Single-Nucleotide Mismatches," Anal. Chem., **73**(7), pp. 1567-1571.

[28] Garcia, R. and San Paulo, A., 1999, "Attractive and Repulsive Tip-Sample Interaction Regimes in Tapping-Mode Atomic Force Microscopy," Phys. Rev. B, **60**(7), pp. 4961-4967.

[29] San Paulo, A. and Garcia, R., 2000, "High-Resolution Imaging of Antibodies by Tapping-Mode Atomic Force Microscopy: Attractive and Repulsive Tip-Sample Interaction Regimes," Biophys. J., **78**(3), pp. 1599-1605.

[30] Garcia, R. and San Paulo, A., 2000, "Amplitude Curves and Operating Regimes in Dynamic Atomic Force Microscopy," Ultramicroscopy, **82**(1-4), pp. 79-83.

[31] Davis, Z.J., Abadal, G., Kuhn, O., Hansen, O., Grey, F., and Boisen, A., 2000, "Fabrication and Characterization of Nanoresonating Devise for Mass Detection," J. Vac. Sci. Technol. B, **18**(2), pp. 612-616.

[32] Hagleitner, C., Lange, D., Hierlemann, A., Brand, O., and Baltes, H., 2002, "CMOS Single-Chip Gas Detection System Comprising Capacitive, Calorimetric and Mass-Sensitive Microsensors," IEEE J. Solid-St. Circ., **37**(12), pp. 1867-1878.

[33] Lange, D., Hagleitner, C., Hierlemann, A., Brand, O., and Baltes, H., 2002, "Complementary Metal Oxide Semiconductor Cantilever Arrays on a Single Chip: Mass Sensitive Detection of Volatile Organic Compounds," Anal. Chem., **74**(13), pp. 3084-3095.

[34] Davis, Z.J., Abadal, G., Helbo, B., Hansen, O., Campabadal, F., Perez-Murano, F., Esteve, J., Figueras, E., Verd, J., Barniol, N., and Boisen, A., 2003, "Monolithic Integration of Mass Sensing Nano-Cantilevers with CMOS Circuitry," Sensor. Actuat. A, **105**(3), pp. 311-319.

[35] Arcamone, J., Rius, G., Abadal, G., Teva, J., Barniol, N., and Perez-Murano, F., 2006, "Micro/Nanomechanical Resonators for Distributed Mass Sensing with Capacitive Detection," Microelectron. Eng., **83**(4-9), pp. 1216-1220.

[36] Strick, T.R., Dessinges, M.N., Charvin, G., Dekker, N.H., Allemand, J.F., Bensimon, D., and Croquette, V., 2003, "Stretching of Macromolecules and Proteins," Rep. Prog. Phys., **66**(1), pp. 1-45.

[37] Kang, S.-W. and Banerjee, D., 2011, "Point-Mass Model for Nano-Patterning Using Dip-Pen Nanolithography (DPN)," Sensors & Transducers, **11**, pp. 64-73.

[38] Meyer, G. and Amer, N.M., 1988, "Novel Optical Approach to Atomic Force Microscopy," Appl. Phys. Lett., **53**(12), pp. 1045-1047.

[39] Villanueva, G., Montserrat, J., Perez-Murano, F., Rius, G., and Bausells, J., 2004, "Submicron Piezoresistive Cantilevers in a CMOS-Compatible Technology for Intermolecular Force Detection," Microelectron. Eng., **73-74**, pp. 480-486.

[40] Li, P., Li, X., Zuo, G., Liu, J., Wang, Y., Liu, M., and Jin, D., 2006, "Silicon Dioxide Microcantilever with Piezoresistive Element Integrated for Portable Ultraresoluble Gaseous Detection," Appl. Phys. Lett., **89**, pp. 074104-1-3.

[41] Boisen, A., Thaysen, J., Jensenius, H., and Hansen, O., 2000, "Environmental Sensors Based on Micromachined Cantilevers with Integrated Read-out," Ultramicroscopy, **82**, pp. 11-16.

[42] Kobayashi, T., Tsaur, J., Ichiki, M., and Maeda, R., 2006, "Fabrication and Performance of a Flat Piezoelectric Cantilever Obtained Using a Sol-Gel Derived PZT Thick Film Deposited on a SOI Wafer," Smart Mater. Struct., **15**(1), pp. S137-S140.

[43] Katragadda, R., Wang, Z., Khalid, W., Li, Y., and Xu, Y., 2007, "Parylene Cantilevers Integrated with Polycrystalline Silicon Piezoresistors for Surface Stress Sensing," Appl. Phys. Lett., **91**, pp. 083505-1-3.

[44] Ibbotson, R.H., Dunn, R.J., Djakov, V., Ferrigno, P.K., and Huq, S.E., 2008, "Polyimide Microcantilever Surface Stress Sensor Using Low-Cost, Rapidly-

Interchangeable, Spring-Loaded Microprobe Connections," Microelectron. Eng., **85**, pp. 1314-1317.

[45] Ansari, M.Z., Cho, C., Kim, J., and Bang, B., 2009, "Comparison Between Deflection and Vibration Characteristics of Rectangular and Trapezoidal Profile Microcantilevers," Sensors, **9**, pp. 2706-2718.

[46] Ansari, M.Z. and Cho, C., 2009, "Deflection, Frequency, and Stress Characteristics of Rectangular, Triangular, and Step Profile Microcantilevers for Biosensors," Sensors, **9**, pp. 6046-6057.

[47] Stoney, G.G., 1909, "The Tension of Metallic Films Deposited by Electrolysis," Proc. R. Soc. Lon. Ser-A, **82**, pp. 172-175.

[48] Sader, J.E., 2001, "Surface Stress Induced Deflections of Cantilever Plates with Applications to the Atomic Force Microscope: Rectangular Plates," J. Appl. Phys., **89**(5), pp. 2911-2921.

[49] Rao, S.S., 1997, *Fundamentals of Mechanical Vibrations*, Addison-Wesley, Singapore.

[50] Liu, Y.-S., 2006, "Development of an Advanced Nanocalorimetry System for Rapid Material Characterizations," Ph.D. Thesis, Texas A&M University, College Station, TX, USA.

[51] Carreto-Vazquez, V.H., Wojcik, A.K., Liu, Y.-S., Bukur, D.B., and Mannan, M.S., 2010, "Miniaturized Calorimeter for Thermal Screening of Energetic Materials," Microelectr. J., **41**, pp. 874-881.

[52] Pinnaduwage, L.A., Gehl, A., Hedden, D.L., Muralidharan, G., Thundat, T., Lareau, R.T., Sulchek, T., Manning, L., Rogers, B., Jones, M., and Adams, J.D., 2003, "A Microsensor for Trinitrotoluene Vapour," Nature, **425**, pp. 474.

[53] Pinnaduwage, L.A., Ji, H.-F., and Thundat, T., 2005, "Moore's Law in Homeland Defense: An Integrated Sensor Platform Based on Silicon Microcantilevers," IEEE Sens. J., **5**(4), pp. 774-785.

[54] Zhu, W., Park, J.S., Sessler, J.L., and Gaitas, A., 2011, "A Colorimetric Receptor Combined with a Microcantilever Sensor for Explosive Vapor Detection," Appl. Phys. Lett., **98**, pp. 123501-1-3.

[55] Muralidharan, G., Wig, A., Pinnaduwage, L.A., Hedden, D., Thundat, T., and Lareau, R.T., 2003, "Adsorption-Desorption Characteristics of Explosive Vapors Investigated with Microcantilevers," Ultramicroscopy, **97**, pp. 433-439.

[56] Pinnaduwage, L.A., Thundat, T., Gehl, A., Wilson, S.D., Hedden, D.L., and Lareau, R.T., 2004, "Desorption Characteristics of Uncoated Silicon Microcantilever Surfaces for Explosive and Common Nonexplosive Vapors," Ultramicroscopy, **100**, pp. 211-216.

[57] Nelson, I.C., Banerjee, D., Rogers, W.J., and Mannan, M.S., 2006, "Detection of Explosives Using Heated Micro-Cantilever Sensors," Proc. SPIE, **6223**, 62230O-1-8.

[58] Ahn, J.A., Eastwood, C., Sitzki, L., and Ronney, P.D., 2005, "Gas-Phase and Catalytic Combustion in Heat-Recirculating Burners," P. Combust. Inst., **30**, pp. 2463-2472.

[59] Mills, A.F., 1995, *Heat and Mass Transfer*, Prentice Hall, Upper Saddle River, NJ, USA.

[60] Schwartz, A., Holbrook, L.L., and Wise, H., 1971, "Catalytic Oxidation Studies with Platinum and Palladium," J. Catal., **21**, pp. 199-207.

[61] Hayes, R.E. and Kolaczkowski, S.T., 1997, *Introduction to Catalytic Combustion*, Gordon and Breach Science Publishers, Netherlands.

[62] Fuller, E.N., Schettler, P.D., and Giddings, J.C., 1966, "A New Method for Prediction of Binary Gas-Phase Diffusion Coefficients," Ind. Eng. Chem., **58**(5), pp. 19-27.

[63] Fogler, H.S., 1999, *Elements of Chemical Reaction Engineering*, 3rd Edition, Prentice Hall, Upper Saddle River, NJ, USA.

[64] Ramos, D., Mertens, J., Calleja, M., and Tamayo, J., 2007, "Study of the Origin of Bending Induced by Bimetallic Effect on Microcantilever," Sensors, **7**, pp. 1757-1765.

[65] Klein, C.A., 2000, "How Accurate are Stoney's Equation and Recent Modifications," J. Appl. Phys., **88**(8), pp. 5487-5489.

[66] Chu, W.-H., Chu, W.-H., Mehregany, M., and Mullen, R.L., 1993, "Analysis of Tip Deflection and Force of a Bimetallic Cantilever Microactuator," J. Micromech. Microeng., **3**, pp. 4-7.

[67] Hsueh, C.-H., 2002, "Modeling of Elastic Deformation of Multilayers Due to Residual Stresses and External Bending," J Appl. Phys., **91**(12), pp. 9652-9656.

[68] Lee, C.-Y., Tasi, C.-H., Chen, L.-W., Fu, L.-M., and Chen, Y.-C., 2006, "Elastic-Plastic Modeling of Heat-Treated Bimorph Mico-Cantilevers," Microsyst. Technol., **12**, pp. 979-986.

[69] Hodge, T.C., Bidstrup-Allen, S.A., and Kohl, P.A., 1997, "Stresses in Thin Film Metallization," IEEE T. Compon. Pack. A, **20**, pp. 241-250.

[70] Fu, J.Y., Chen, D.P., Ye, T.C., Jiao, B.B., and Ou, Y., 2009, "Modeling and Optimal Design of Multilayer Thermal Cantilever Microactuators," Sci. China Ser. E-Tech. Sci., **52**, pp. 1167-1170.

[71] Pal, S., and Xie, H., 2010, "Distributed and Lumped Element Models for a Bimorph-Actuated Micromirror," J. Micromech. Microeng., **20**(4), pp. 045020.

[72] Jiang, J., Hilleringmann, U., and Shui, X., 2007, "Electro-Thermo-Mechanical Analytical Modeling of Multilayer Cantilever Microactuator," Sensor. Actuat. A, **137**, pp. 302-307.

[73] Bullen, D., Wang, X., Zou, J., Chung, S.-W., Mirkin, C.A., and Liu, C., 2004, "Design, Fabrication, and Characterization of Thermally Actuated Probe Arrays for Dip Pen Nanolithography," J. Microelectromech. S., **13**, pp. 594-602.

[74] Langer, G., Hartmann, J., and Reichling, M., 1997, "Thermal Conductivity of Thin Metallic Film Measured by Photothermal Profile Analysis," Rev. Sci. Instrum., **68**, pp. 1510-1513.

[75] Jou, J.H., Liao, C.N., and Jou, K.W., 1994, "A Method for the Determination of Gold Thin-Films Mechanical-Properties," Thin Solid Films, **238**, pp. 70-72.

[76] Khan, A., Philip, J., and Hess, P., 2004, "Young's Modulus of Silicon Nitride Used in Scanning Force Microscope Cantilevers," J. Appl. Phys., **95**, pp. 1667-1672.

[77] Pamula, V.K., Jog, A., and Fair, R.B., 2001, "Mechanical Property Measurement of Thin-Film Gold Using Thermally Acutated Bimetallic Cantilever Beams," Nanotech 2001, **1**, pp. 410-413.

[78] Piccirillo, A. and Gobbi, A.L., 1990, "Physical-Electrical Properties of Silicon Nitride Deposited by PECVD on I II-V Semiconductors," J. Electrochem. Soc., **137**(12), pp. 3910-3917.

[79] de Vries, J.W.C., 1988, "Temperature and Thickness Dependence of the Resistivity of Thin Polycrystalline Aluminum, Cobalt, Nickel, Palladium, Silver and Gold Films," Thin Solid Films, **167**, pp. 25-32.

[80] Banerjee, D., 2006, *Vol. I: Biological and Biomedical Nanotechnology – Dip Pen Technologies for Bio-molecular Devices*, Editor: A. Lee, Kluwer, New York, NY, USA.

[81] Schwartz, P.V., 2002, "Molecular Transport from an Atomic Force Microscope Tip: A Comparative Study of Dip-Pen Nano-lithography," Langmuir, **18**, pp. 4041-4046.

[82] Haaheim, J. and Nafday, O.A., 2008, "Dip Pen Nanolithography®: A "Desktop Nanofab™" Approach Using High-Throughput Flexible Nanopatterning," Scanning, **30**, pp. 137-150.

[83] Kang, S.-W., Banerjee, D., Kaul, A.B., and Megerian, K.G., 2010, "Nanopatterning of Catalyst by Dip-Pen Nanolithography (DPN) for Synthesis of Carbon Nanotubes (CNT)," Scanning, **31**(1), pp. 42-48.

[84] Jang, J., Hong, S., Schatz, G.C., and Ratner, M.A., 2001, "Self-Assembly of Ink Molecules in Dip-Pen Nanolithography: A Diffusion Model," J. Chem. Phys., **115**(6), pp. 2721-2729.

[85] Sheehan, P.E. and Whitman, L.J., 2002, "Thiol Diffusion and the Role of Humidity in Dip-Pen Nanolithography," Phys. Rev. Lett., **88**(15), pp. 156104-1-156104-4.

[86] Adamson, A.W. and Gast, A.P., 1997, *Physical Chemistry of Surfaces – Ch. 10 The Solid-Liquid Interface-Contact Angle*, John Wiley & Sons, Inc., New York, NY, USA.

[87] Weeks, B.L. and Vaughn, M.W., 2005, "Direct Imaging of Meniscus Formation in Atomic Force Microscopy Using Environmental Scanning Electron Microscopy," Langmuir, **21**, pp. 8096-8098.

[88] Rozhok, S., Piner, R., and Mirkin, C.A., 2003, "Dip-Pen Nanolithography: What Controls Ink Transport?" J. Phys. Chem. B, **107**(3), pp. 751-757.

[89] Liu, Z., Yang, Y., Qu, Y., Dong, Z., Li, W.J., and Wang, Y., 2007, "Vibration-Mode Based Real-Time Nanoimaging and Nanomanipulation," IEEE-Nano 2007, pp. 515-519, Hong Kong, August 2 - 5.

[90] Melcher, J., Hu, S., and Raman, A., 2007, "Equivalent Point-Mass Models of Continuous Atomic Force Microscope Probes," Appl. Phys. Lett., **91**, pp. 053101-1-053101-3.

[91] Legleiter, J., Park, M., Cusick, B., and Kowalewski, T., 2006, "Scanning Probe Acceleration Microscopy (SPAM) in Fluids: Mapping Mechanical Properties of Surfaces at the Nanoscale," Proc. Natl. Acad. Sci. USA, **103**(13), pp. 4813-4818.

[92] Pietrement, O., Beaudoin, J.L., and Troyon, M., 1999 "A New Calibration Method of the Lateral Contact Stiffness and Lateral Force Using Modulated Lateral Force Microscopy," Tribol. Lett., **7**, pp. 213-220.

[93] Clifford, C.A. and Seah, M.P., 2005, "The Determination of Atomic Force Microscope Cantilever Spring Constants via Dimensional Methods for Nanomechanical Analysis," Nanotechnology, **16**, pp. 1666-1680.

[94] Derjaguin, B.V., Muller, V.M., and Toporov, Yu.P., 1975, "Effect of Contact Deformations on the Adhesion of Particles," J. Colloid Interf. Sci., **53**, pp. 314-326.

[95] Song, Y. and Bhushan, B., 2006, "Simulation of Dynamic Modes of Atomic Force Microsocopy Using a 3D Finite Element Model," Ultramicroscopy, **106**, pp. 847-873.

[96] Mazeran, P.-E. and Loubet, J.-L., 1999, "Normal and Lateral Modulation with a Scanning Force Microscope, and an Analysis: Implication in Quantitative Elastic and Friction Imaging," Tribol. Lett., **7**, pp. 199-212.

[97] Lantz, M.A., O'Shea, S.J., Hoole, A.C.F., and Welland, M.E., 1997, "Lateral Stiffness of the Tip and Tip-Sample Contact in Frictional Force Microscopy," Appl. Phys. Lett., **70**, pp. 118476-1-118476-3.

[98] Johnson, K.L., 1985, *Contact Mechanics*, Cambridge University Press, New York, NY, USA.

[99] Basak, S. and Raman, A., 2007, "Dynamics of Tapping Mode Atomic Force Microscopy in Liquids: Theory and Experiments," Appl. Phys. Lett., **91**, pp. 064107-1-064107-3.

[100] Huang, L., Jia, Z., and O'Brien, S., 2007, "Orientated Assembly of Single-walled Carbon Nanotubes and Applications," J. Mater. Chem., **17**, pp. 3863-3874.

[101] Salvetat, J.-P., Bonard, J.-M., Thomson, N.H., Kulik, A.J., Forró, L., Benoit, W., and Zuppiroli, L., 1999, "Mechanical Properties of Carbon Nanotubes," Appl. Phys. A-Mater, **69**, pp. 255-260.

[102] Javey, A., Guo, J., Farmer, D.B., Wang, Q., Yenilmez, E., Gordon, R.G., Lundstrom, M., and Dai, H., 2004, "Self-Aligned Ballistic Molecular Transistors and Electrically Parallel Nanotube Arrays," Nano Lett., **4**, pp. 1319-1322.

[103] Yan, Y., Chan-Park, M.B., and Zhang, Q., 2007, "Advances in Carbon-Nanotube Assembly," Small, **3**(1), pp. 24-42.

[104] Robertson, J., 2007, "Growth of Nanotubes for Electronics," Mater. Today, **10**(1-2), pp. 36-43.

[105] Star, A., Joshi, V., Skarupo, S., Thomas, D., and Gabriel, J.-C.P., 2006, "Gas Sensor Array Based on Metal-decorated Carbon Nanotubes," J. Phys. Chem. B, **110**(42), pp. 21014-21020.

[106] Bower, C., Zhou, O., Zhu, W., Werder, D.J., and Jin, S., 2000, "Nucleation and Growth of Carbon Nanotubes by Microwave Plasma Chemical Vapor Deposition," Appl. Phys. Lett., **77**(17), pp. 2767-2769.

[107] Chhowalla, M., Teo, K.B.K., Ducati, C., Rupesinghe, N.L., Amaratunga, G.A.J., Ferrari, A.C., Roy, D., Robertson, J., and Milne, W.I., 2001, "Growth Process Conditions of Vertically Aligned Carbon Nanotubes Using Plasma Enhanced Chemical Vapor Deposition," J. Appl. Phys., **90**(10), pp. 5308-5317.

[108] Rohmund, F., Falk, L.K.L., and Campbell, E.E.B., 2000, "A Simple Method for the Production of Large Arrays of Aligned Carbon Nanotubes," Chem. Phys. Lett., **328**, pp. 369-373.

[109] Li, Y., Kim, W., Zhang, Y., Rolandi, M., Wang, D., and Dai, H., 2001, "Growth of Single-walled Carbon Nanotubes from Discrete Catalytic Nanoparticles of Various Sizes," J. Phys. Chem. B, **105**, pp. 11424-11431.

[110] Nerushev, O.A., Dittmar, S., Morjan, R.-E., Rohmund, F., and Campbell, E.E.B., 2003, "Particle Size Dependence and Model for Iron-catalyzed Growth of Carbon Nanotubes by Thermal Chemical Vapor Deposition," J. Appl. Phys., **93**(7), pp. 4185-4190.

[111] Li, B., Goh, C.F., Zhou, X., Lu, G., Tantang, H., Chen, Y., Xue, C., Boey, F.Y.C., and Zhang, H., 2008, "Patterning Colloidal Metal Nanoparticles for Controlled Growth of Carbon Nanotubes," Adv. Mater., **20**, pp. 4873-4878.

[112] Morjan, R.E., Nerushev, O.A., Sveningsson, M., Rohmund, F., Falk, L.K.L., and Campbell, E.E.B., 2004, "Growth of Carbon Nanotubes from C_{60}," Appl. Phys. A-Mater., **78**, pp. 253-261.

[113] Biró, L.P., Ehlich, R., Tellgmann, R., Gromov, A., Krawez, N., Tschaplyguine, M., Pohl, M.-M., Zsoldos, E., Vértesy, Z., Horváth, Z.E., and Campbell, E.E.B., 1999, "Growth of Carbon Nanotubes by Fullerene Decomposition in the Presence of Transition Metals," Chem. Phys. Lett., **306**, pp. 155-162.

[114] Homma, Y., Kobayashi, Y., Ogino, T., Takagi, D., Ito, R., Jung, Y.J., and Ajayan, P.M., 2003, "Role of Transition Metal Catalysts in Single-walled Carbon Nanotube Growth in Chemical Vapor Deposition," J. Phys. Chem. B, **107**, pp. 12161-12164.

[115] Rivas Cardona, J.A., 2006, "Development of a Microfluidic Device for Patterning Multiple Species by Scanning Probe Lithography," M.S. Thesis, Texas A&M University, College Station, TX, USA.

[116] Huitink, D., 2007, "Nanolithographic Control of Carbon Nanotube Synthesis," M.S. Thesis, Texas A&M University, College Station, TX, USA.

[117] Gargate, R.V., 2008, "Synthesis and Characterization of Carbon Nanotubes using Scanning Probe based Nano-lithographic Techniques," M.S. Thesis, Texas A&M University, College Station, TX, USA.

[118] Banerjee, D., Amro, N.A., and Fragla, J., 2005, "Optimization of Microfluidic Ink-Delivery Apparatus for Dip Pen Nanolithography™," SPIE J. Microlithogr. Microfabrication, Microsyst., **4**, pp. 023014-023021.

[119] Rosner, B., Duenas, T., Banerjee, D., Shile, R., Amro, N., and Rendlen, J., 2005, "Functional Extensions of Dip Pen Nanolithography™: Active Probes and Microfluidic Ink Delivery," Smart Mater. Struct., **15**, pp. S124-S130.

[120] Rivas-Cordona, J.A. and Banerjee, D., 2007, "Microfluidic Device for Delivery of Multiple Inks for Dip Pen Nanolithography," SPIE J. Microlithogr. Microfabrication, Microsyst., **6**(3), pp. 033004-12.

[121] Gargate, R.V. and Banerjee, D., 2008, "In Situ Synthesis of Carbon Nanotubes on Heated Scanning Probes Using Dip Pen Techniques," Scanning, **30**, pp. 151-158.

[122] Ding, Y., Alias, H., Wen, D., and Williams, R.A., 2006, "Heat Transfer of Aqueous Suspensions of Carbon Nanotubes (CNT Nanofluids)," Int. J. Heat Mass Tran., **49**, pp. 240-250.

[123] Zhang, Y. and Iijima, S., 1999, "Formation of Single-wall Carbon Nanotubes by Laser Ablation of Fullerenes at Low Temperature," Appl. Phys. Lett., **75**(20), pp. 3087-3089.

[124] Czerwosz, E., Dluzewski, P., Dmowska, G., Nowakowski, R., Starnawska, E., and Wronka, H., 1999, "Atomic Force Microscopy and Transmission Electron Microscopy Investigations of Catalytic Formed Nanotubes in C_{60}/C_{70} + *Ni* Layers," Appl. Surf. Sci., **141**, pp. 350-356.

[125] Kozanoglu, B. and Lopez, J., 2007, "Thermal Boundary Layer and the Characteristic Length on Natural Convection over a Horizontal Plate," Heat Mass Transfer, **43**(4), pp. 333-339.

[126] Yaws, C.L. and Yang, H.C., 2009, "To Estimate Vapor Pressure Easily," Hydrocarb. Process., **68**(10), pp. 65-70.

[127] Basevich, V.Ya., Belyaev, A.A., and Frolov, S.M., 1998, "Global Kinetic Mechanisms for Calculating Turbulent Reactive Flows – 1. The Basic Chemical Heat Release Process," Chem. Phys. Rep., **17**(9), pp. 1747-1772.

[128] Gnesdilov, N.N., Dobrego, K.V., Kozlov, I.M., and Shmelev, E.S., 2006, "Numerical Study and Optimization of the Porous Media VOC Oxidizer with Electric Heating Elements," Int. J. Heat Mass Tran., **49**, pp. 5062-5069.

[129] Trenwith, A.B., 1975, "Thermal Decomposition of Isopropanol," J. Chem. Soc., Farad. T. 1, **71**, pp. 2405-2412.

[130] Everaert, K. and Baeyens, J., 2004, "Catalytic Combustion of Volatile Organic Compounds," J. Hazard. Mater., **109**(1-3), pp. 113-139.

[131] Wittstock, A., Zielasek, V., Biener, J., Friend, C.M., and Baumer, M., 2010, "Nanoporous Gold Catalysts for Selective Gas-phase Oxidative Coupling of Methanol at Low Temperature," Science, **327**, pp. 319-322.

[132] Liu, X., Madix, R.J., and Friend, C.M., 2008, "Unraveling Molecular Transformations on Surfaces: A Critical Comparison of Oxidation Reactions on Coinage Metals," Chem. Soc. Rev., **37**, pp. 2243-2261.

[133] Outka, D.A. and Madix, R.J., 1987, "Bronsted Basicity of Atomic Oxygen on the Au(110) Surface: Reactions with Methanol, Acetylene, Water, and Ethylene," J. Am. Chem. Soc., **109**(6), pp. 1708-1714.

[134] Cant, N.W. and Hall, W.K., 1971, "Catalytic Oxidation – IV. Ethylene and Propylene Oxidation over Gold," J. Phys. Chem., **75**(19), pp. 2914-2921.

[135] Dewil, R., Everaert, K., and Baeyens, J., 2005, "Theoretical Assessment of the Catalytic (Pt/TiO_2) Oxidation of Formaldehyde at Ambient Temperature," Catal. Commun., **6**, pp. 793-795.

[136] Gong, J., Flaherty, D.W., Yan, T., and Mullins, C.B., 2008, "Selective Oxidation of Propanol on Au(111): Mechanistic Insights into Aerobic Oxidation of Alcohols," ChemPhysChem, **9**, pp. 2461–2466.

[137] Gil, A., Burgos, N., Paulis, M., Montes, M., and Gandia, L.M., 2000, "Activity and Stability of Single and Perovskite-type Manganese and Cobalt Oxides in the Catalytic Combustion of Acetone," Stud. Surf. Sci. Catal., **130**, pp. 2153-2158.

[138] Hu, C., 2011, "Catalytic Combustion Kinetics of Acetone and Toluene over Cu0.13Ce0.87Oy Catalyst," Chem. Eng. J., **168**, pp. 1185-1192.

[139] Golidets, G.I., Borovik, V.V., and Vorotyntsev, V.M., 1986, "Mechanism and Kinetics of the Selective Catalytic Oxidation of Acetone," Teor. Eksp. Khim., **22**(2), pp. 252-254.

[140] Minico, S., Scire, S., Crisafulli, C., and Galvagno, S., 2001, "Influence of Catalyst Pretreatments on Volatile Organic Compounds Oxidation over Gold/Iron Oxide," Appl. Catal. B: Environ., **34**, pp. 277-285.

[141] Micico, S., Scire, S., Crisafulli, C., Maggiore, R., and Galvagno, S., 2000, "Catalytic Combustion of Volatile Organic Compounds on Gold/Iron Oxide Catalysts," Appl. Catal. B-Environ., **28**, pp. 245-251.

[142] Bond, G.C. and Thompson, D.T., 1999, "Catalysis by Gold," Catal. Rev., **41**(3), pp. 319-388.

[143] Dissanayake, D.P., 2006, *Metal Oxides-Chap17. Applications of Metal Oxides for Volatile Organic Compound Combustion*, Edited by J.L.G. Fierro, CRC Press, Boca Raton, FL, pp. 543-568.

[144] Ismagilov, I.Z., Michurin, E.M., Sukhova, O.B., Tsykoza, L.T., Matus, E.V., Kerzhentsev, M.A., Ismagilov, Z.R., Zagoruiko, A.N., Rebrov, E.V., de Croon, M.H.J.M., and Schouten, J.C., 2008, "Oxidation of Organic Compounds in a Microstructured Catalytic Reactor," Chem. Eng. J., **135S**, pp. S57-S65.

[145] Spivey, J.J., 1987, "Complete Catalytic Oxidation of Volatile Organics," Ind. Eng. Chem. Res., **26**, pp. 2165-2180.

[146] Liu, S.Y. and Yang, S.M., 2008, "Complete Oxidation of 2-propanol over Gold-based Catalysts Supported on Metal Oxides," Appl. Catal. A-Gen., **334**, pp. 92-99.

[147] Kulkarni, D. and Wachs, I.E., 2002, "Isopropanol Oxidation by Pure Metal Oxide Catalysts: Number of Active Surface Sites and Turnover Frequencies," Appl. Catal. A-Gen., **237**, pp. 121-137.

[148] Luis, G., 2006, "Isopropanol Adsorption-oxidation over V_2O_5 – A Mass Spectrometry Study," J. Mol. Catal. A-Chem., **247**, pp. 31-35.

[149] Ali, A.H. and Zaera, F., 2002, "Kinetic Study on the Selective Catalytic Oxidation of 2-propanol to Acetone over Nickel Foils," J. Mol. Catal. A-Chem., **177**, pp. 215-235.

[150] NIST Chemistry Web Book (http://webbook.nist.gov/chemistry), June, 2010.

[151] Poling, B.E., Prausnitz, J.M., and O'Connell, J.P., 2001, *The Properties of Gases and Liquids*, 5th Edition, McGraw-Hill, New York, NY, USA.

[152] Goldman, S., Gray, C.G., Li, W., Tomberli, B., and Joslin, C.G., 1996, "Predicting Solubilities in Supercritical Fluids," J. Phys. Chem., **100**, pp. 7246-7249.

[153] Magalhaes, A.L., Da Silva, F.A., and Silva, C.M., 2011, "New Tracer Diffusion Correlation for Real Systems over Wide Ranges of Temperature and Density," Chem. Eng. J., **166**, pp. 49-72.

[154] Goericke, F.T. and King, W.P., 2008, "Modeling Piezoresistive Microcantilever Sensor Response to Surface Stress for Biochemical Sensors," IEEE Sensors J., **8**(8), pp. 1404-1410.

[155] Aguilar, A.D., Forzani, E.S., Leright, M., Tsow, F., Cagan, A., Iglesias, R.A., Nagahara, L.A., Amlani, I., Tsui, R., and Tao, N.J., 2010, "A Hybrid Nanosensor for TNT Vapor Detection," Nano Lett., **10**, pp. 380-384.

[156] Pang, P., Guo, Z., and Cai, Q., 2005, "Humidity Effect on the Monolayer-Protected Gold Nanoparticles Coated Chemiresistor Sensor for VOCs Analysis," Talanta, **65**, pp. 1343-1348.

[157] Murray, F.W., 1967, "On the Computation of Saturation Vapor Pressure," J. Appl. Meteorol., **6**, pp. 203-204.

[158] Frenkel, M., Kabo, G.J., Marsh, K.N., Roganov, G.N., and Wilhoit, R.C., 1994, *Thermodynamics of Organic Compounds in the Gas State* (*Vol. I*), TRC (Thermodynamics Research Center) Data Series, College Station, TX, USA.

APPENDIX A

PHYSICAL AND THERMO-CHEMICAL DATA

Table XIII. Specific heat of acetone and 2-propanol in gas phase [150, 158].

Acetone [C_3H_6O]		**2-Propanol [C_3H_7OH]**	
Temperature [*K*]	**$C_{p,gas}$ [*J/kg-K*]**	**Temperature [*K*]**	**$C_{p,gas}$ [*J/kg-K*]**
100	*890.67*	*50*	*587.72*
150	*967.29*	*100*	*766.10*
200	*1053.72*	*150*	*964.78*
273.15	*1224.00*	*200*	*1136.17*
298.15	*1291.67*	*273.15*	*1393.09*
300	*1296.83*	*298.15*	*1486.27*
400	*1585.06*	*300*	*1493.26*
500	*1860.88*	*400*	*1866.16*
600	*2103.99*	*500*	*2195.80*
700	*2314.57*	*600*	*2467.69*
800	*2496.56*	*700*	*2691.50*
900	*2654.10*	*800*	*2879.36*
1000	*2790.81*	*900*	*3039.61*
1100	*2909.09*	*1000*	*3177.72*
1200	*3011.71*	*1100*	*3297.36*
1300	*3100.72*	*1200*	*3401.36*
1400	*3178.03*	*1300*	*3491.88*
1500	*3245.35*	*1400*	*3570.92*
		1500	*3639.97*
		1750	*3777.25*
		2000	*3878.75*
		2250	*3953.63*
		2500	*4010.21*
		2750	*4055.14*
		3000	*4088.42*

Table XIV. Thermal conductivity [*W/m-K*] of species in gas phase [150, 158].

Species		***100 K***	***200 K***	***300 K***	***400 K***	***500 K***	***600 K***
H_2	Hydrogen	*0.0686*	*0.1317*	*0.1869*	*0.2304*	-	-
H_2O	Water Vapor	-	-	*0.0187*	*0.0271*	*0.0357*	*0.0471*
N_2	Nitrogen	*0.0098*	*0.0187*	*0.026*	*0.0323*	*0.0383*	*0.044*
O_2	Oxygen	*0.0093*	*0.0184*	*0.0263*	*0.0337*	*0.041*	*0.0481*
CO	Carbon Monoxide	-	-	*0.025*	*0.0323*	*0.0392*	*0.0457*
CO_2	Carbon Dioxide	-	*0.0096*	*0.0168*	*0.0251*	*0.0335*	*0.0416*
C_3H_6	Propylene	-	*0.0053*	*0.0188*	*0.0323*	*0.0458*	*0.0592*
C_3H_6O	Acetone	-	-	*0.0115*	*0.0202*	*0.0306*	*0.0427*
C_3H_8O	2-Propanol	-	*0.0076*	*0.0168*	*0.0260*	*0.0352*	*0.0444*

APPENDIX B

DISTRIBUTION OF GAS SPECIES

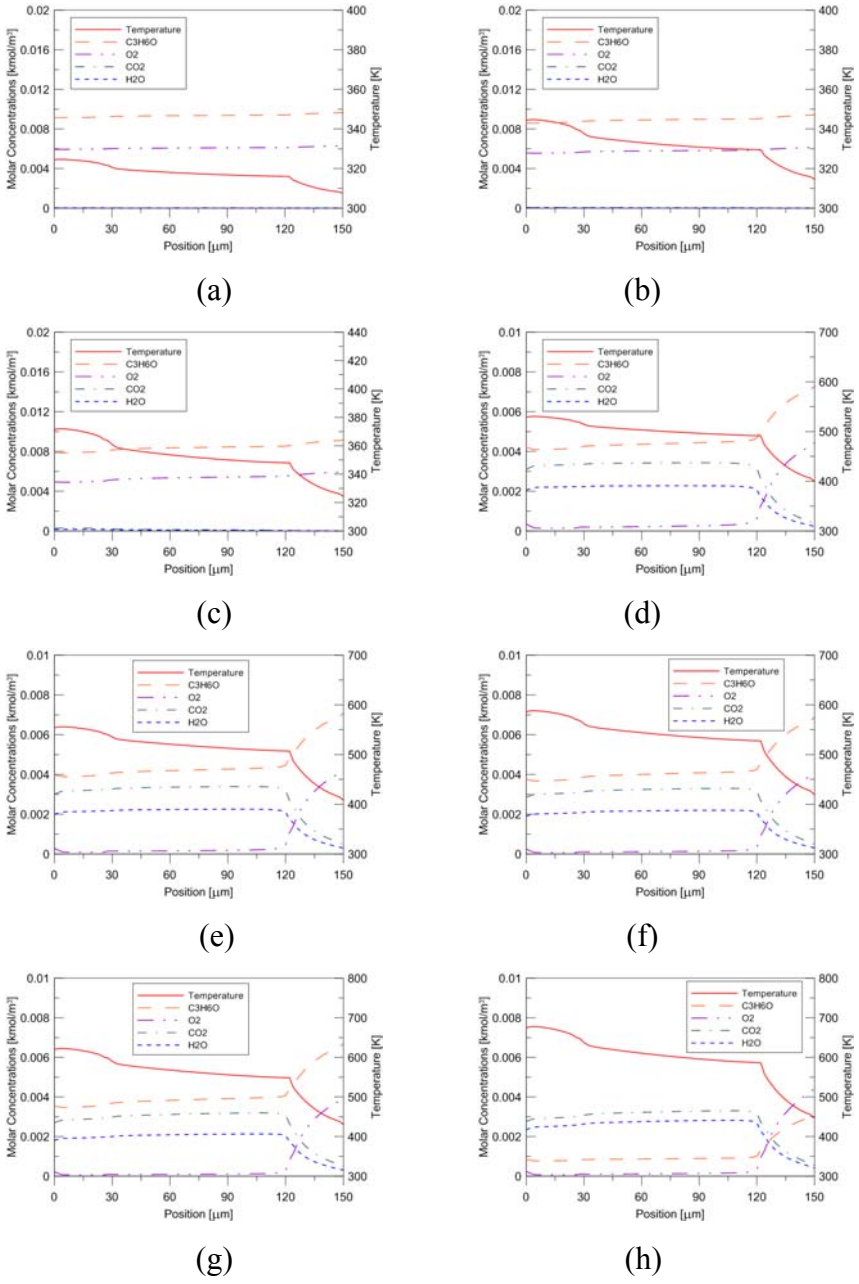

Fig. 58. Surface coverage and wall temperature in different actuation current at room temperature (293.15 *K*) – Explosive vapor: Acetone (C_3H_6O) (a) *6 mA* (b) *8 mA* (c) *10 mA* (d) *12 mA* (e) *14 mA* (f) *16 mA* (g) *18 mA* (h) *20 mA*.

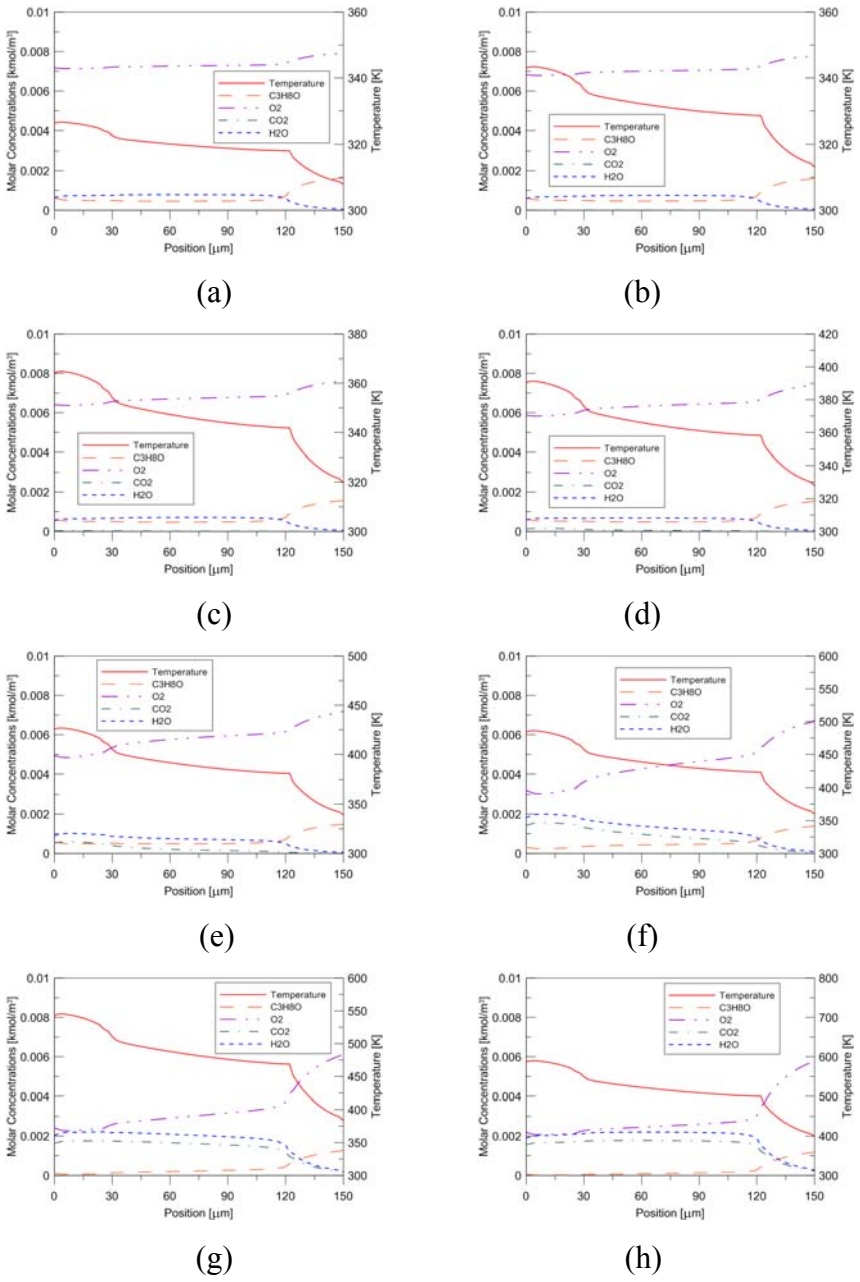

Fig. 59. Surface coverage and wall temperature in different actuation current at room temperature (293.15 *K*) – Explosive vapor: 2-Propanol (C_3H_8O) (a) *6 mA* (b) *8 mA* (c) *10 mA* (d) *12 mA* (e) *14 mA* (f) *16 mA* (g) *18 mA* (h) *20 mA*.

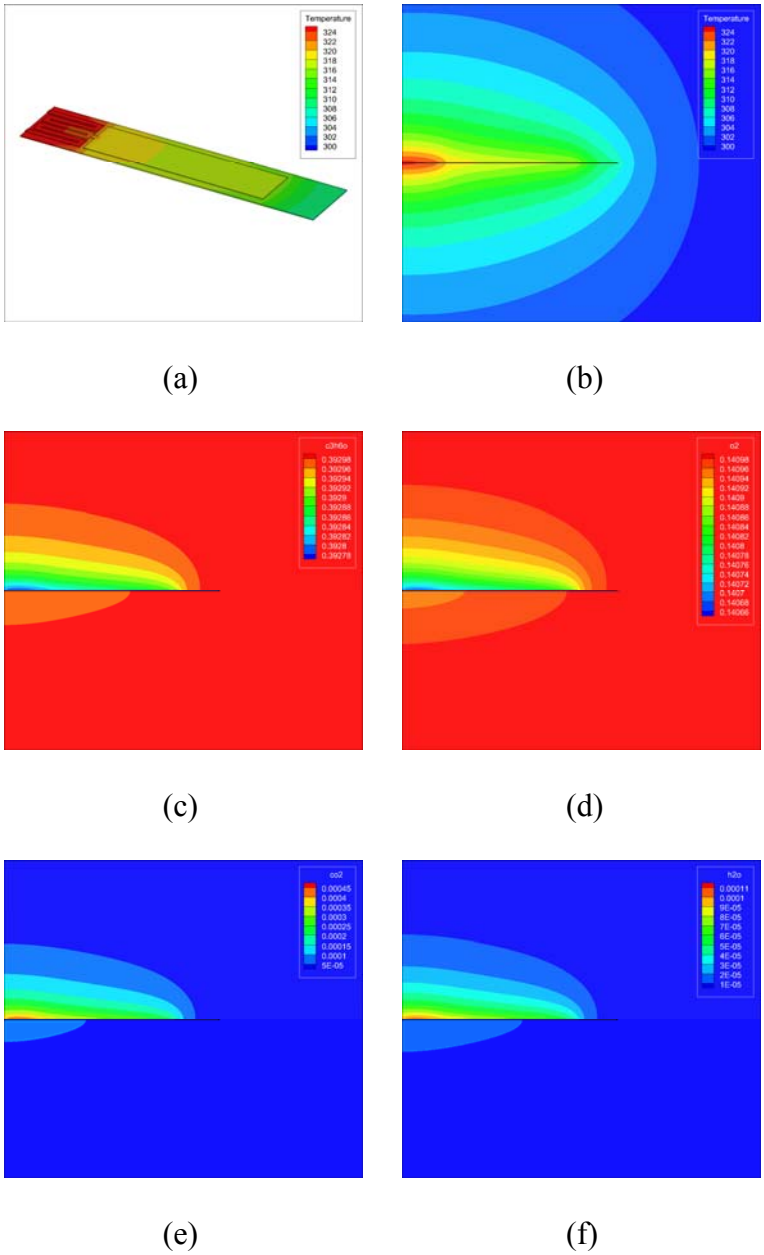

Fig. 60. (a) Simulation results for surface temperature profile; (b) Simulation results for temperature profile within the control volume; Species concentrations distribution for (c) Acetone (C_3H_6O) (d) Oxygen (O_2) (e) Carbon Dioxide (CO_2) (f) Water Vapor (H_2O); Actuation current = *6 mA*.

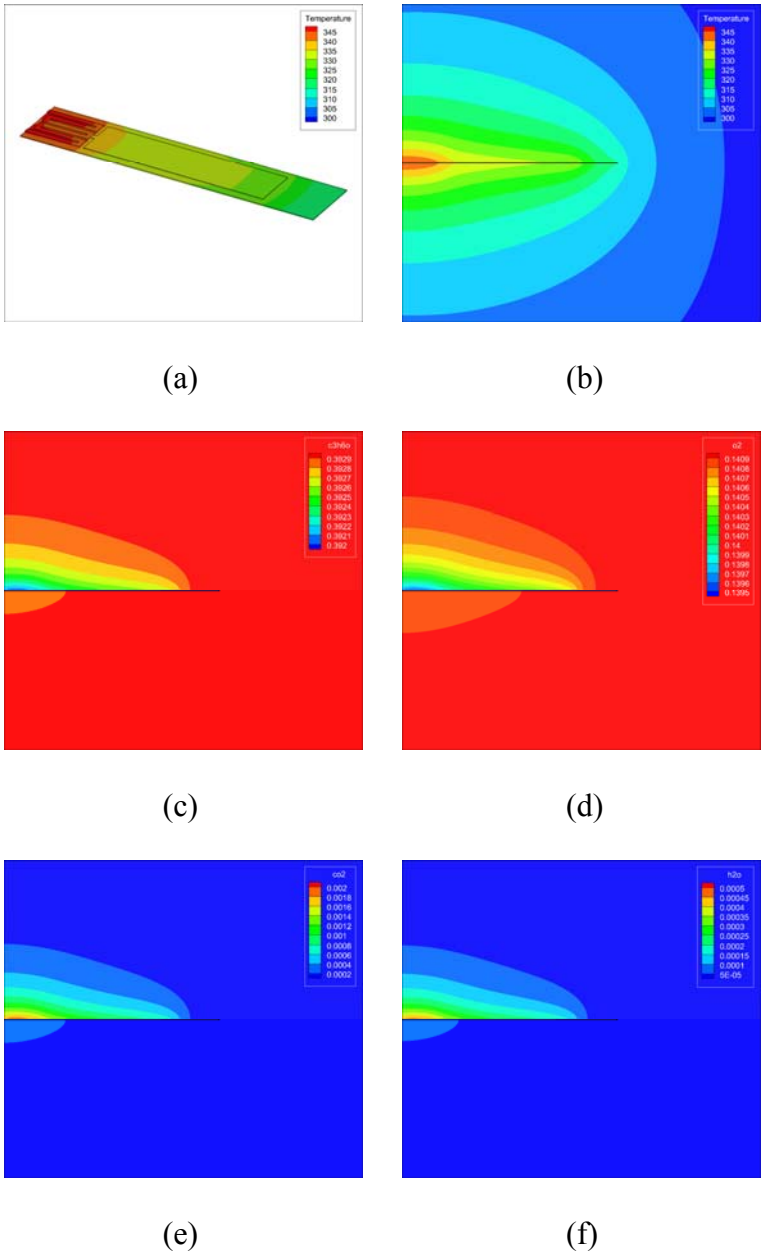

Fig. 61. (a) Simulation results for surface temperature profile; (b) Simulation results for temperature profile within the control volume; Species concentrations distribution for (c) Acetone (C_3H_6O) (d) Oxygen (O_2) (e) Carbon Dioxide (CO_2) (f) Water Vapor (H_2O); Actuation current = *8 mA*.

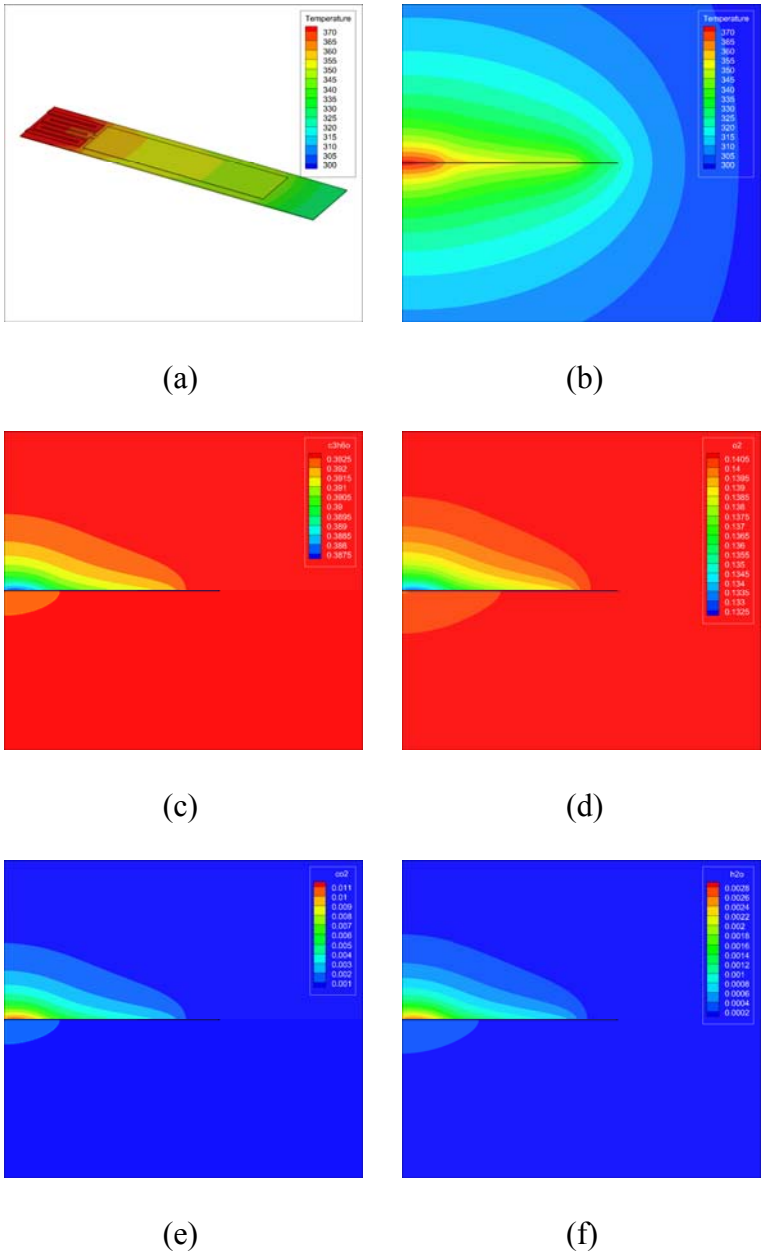

(a) (b)

(c) (d)

(e) (f)

Fig. 62. (a) Simulation results for surface temperature profile; (b) Simulation results for temperature profile within the control volume; Species concentrations distribution for (c) Acetone (C_3H_6O) (d) Oxygen (O_2) (e) Carbon Dioxide (CO_2) (f) Water Vapor (H_2O); Actuation current = *10 mA*.

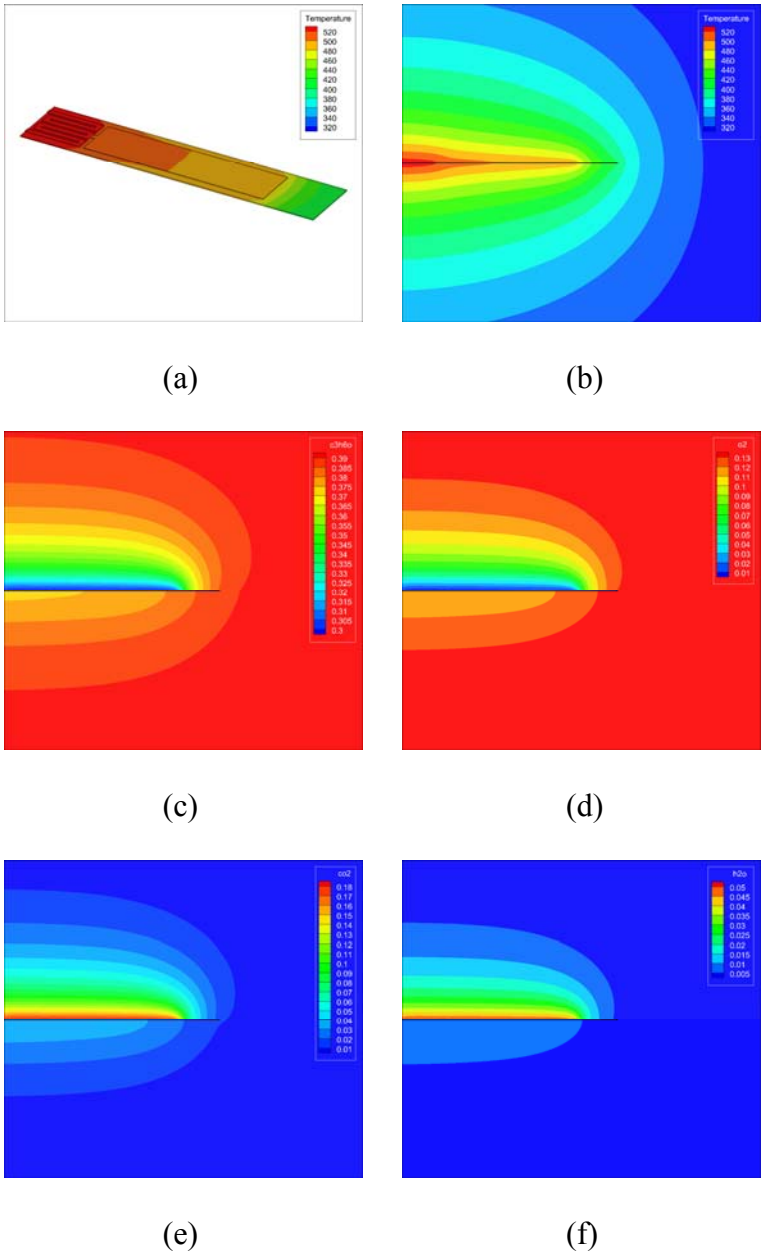

Fig. 63. (a) Simulation results for surface temperature profile; (b) Simulation results for temperature profile within the control volume; Species concentrations distribution for (c) Acetone (C_3H_6O) (d) Oxygen (O_2) (e) Carbon Dioxide (CO_2) (f) Water Vapor (H_2O); Actuation current = *12 mA*.

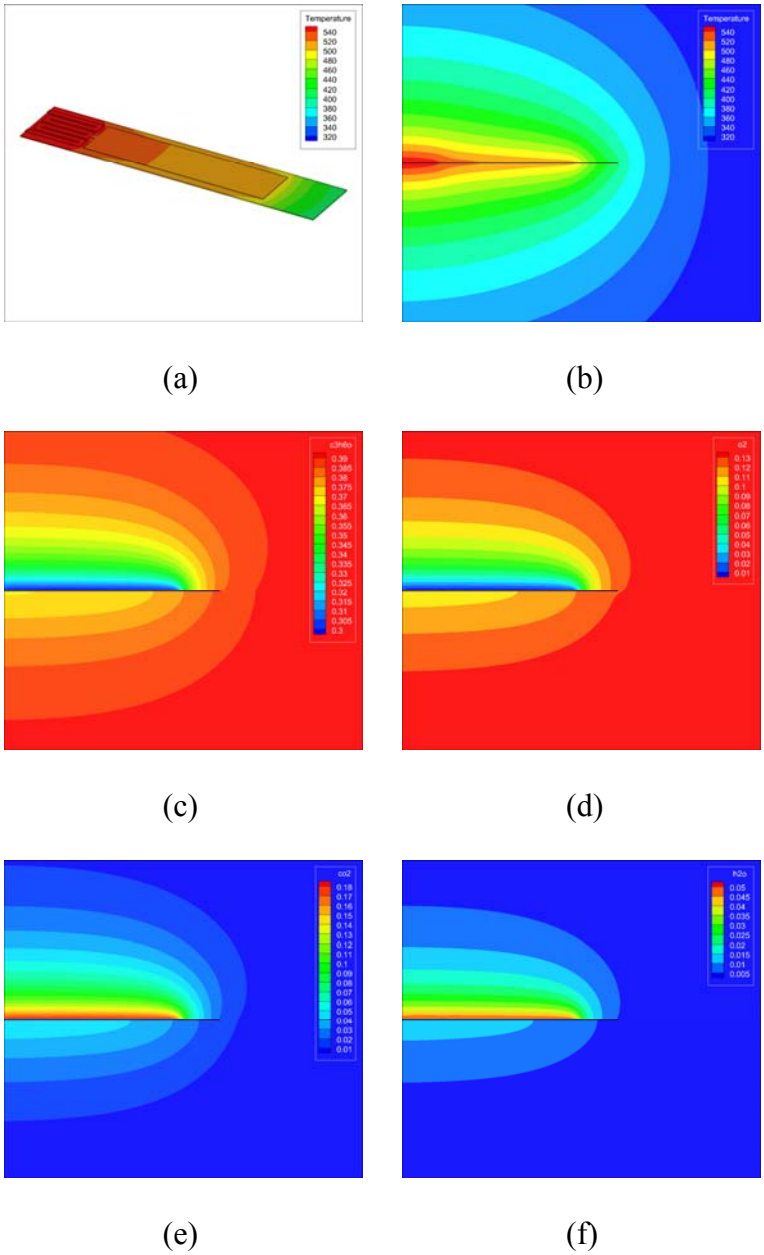

Fig. 64. (a) Simulation results for surface temperature profile; (b) Simulation results for temperature profile within the control volume; Species concentrations distribution for (c) Acetone (C_3H_6O) (d) Oxygen (O_2) (e) Carbon Dioxide (CO_2) (f) Water Vapor (H_2O); Actuation current = *14 mA*.

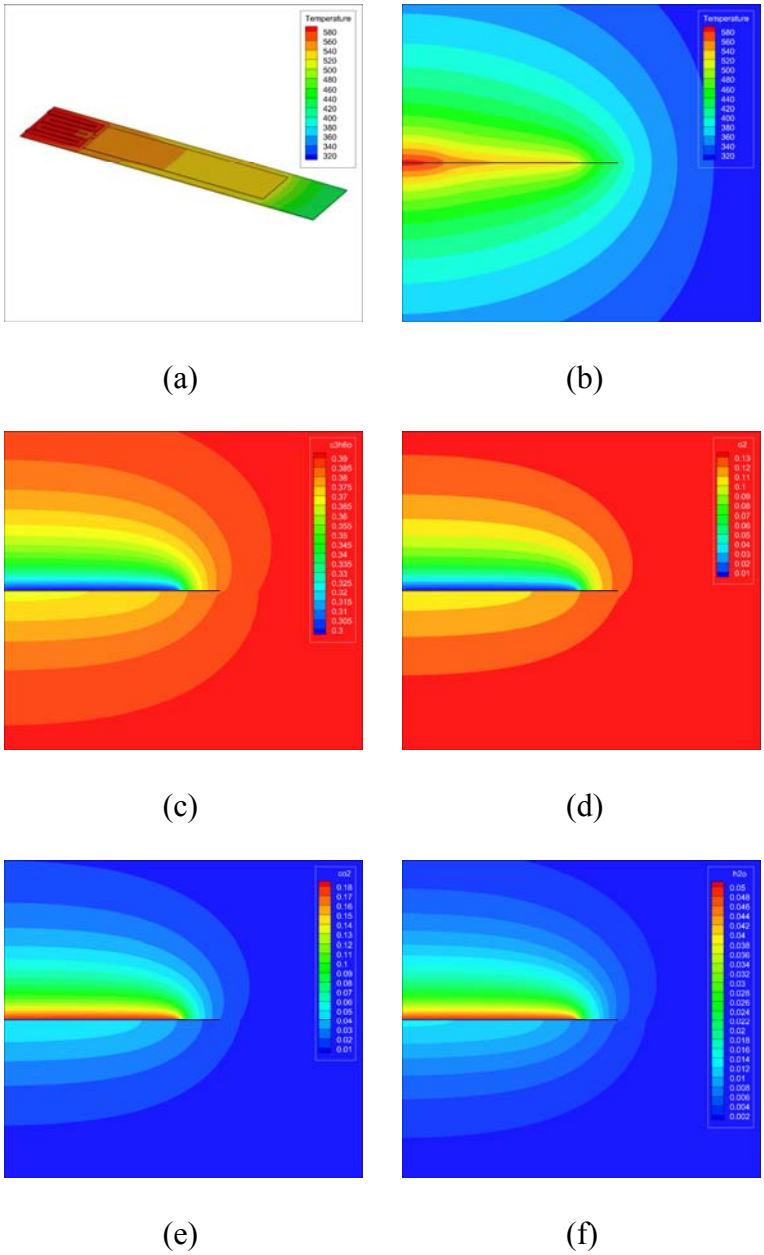

Fig. 65. (a) Simulation results for surface temperature profile; (b) Simulation results for temperature profile within the control volume; Species concentrations distribution for (c) Acetone (C_3H_6O) (d) Oxygen (O_2) (e) Carbon Dioxide (CO_2) (f) Water Vapor (H_2O); Actuation current = *16 mA*.

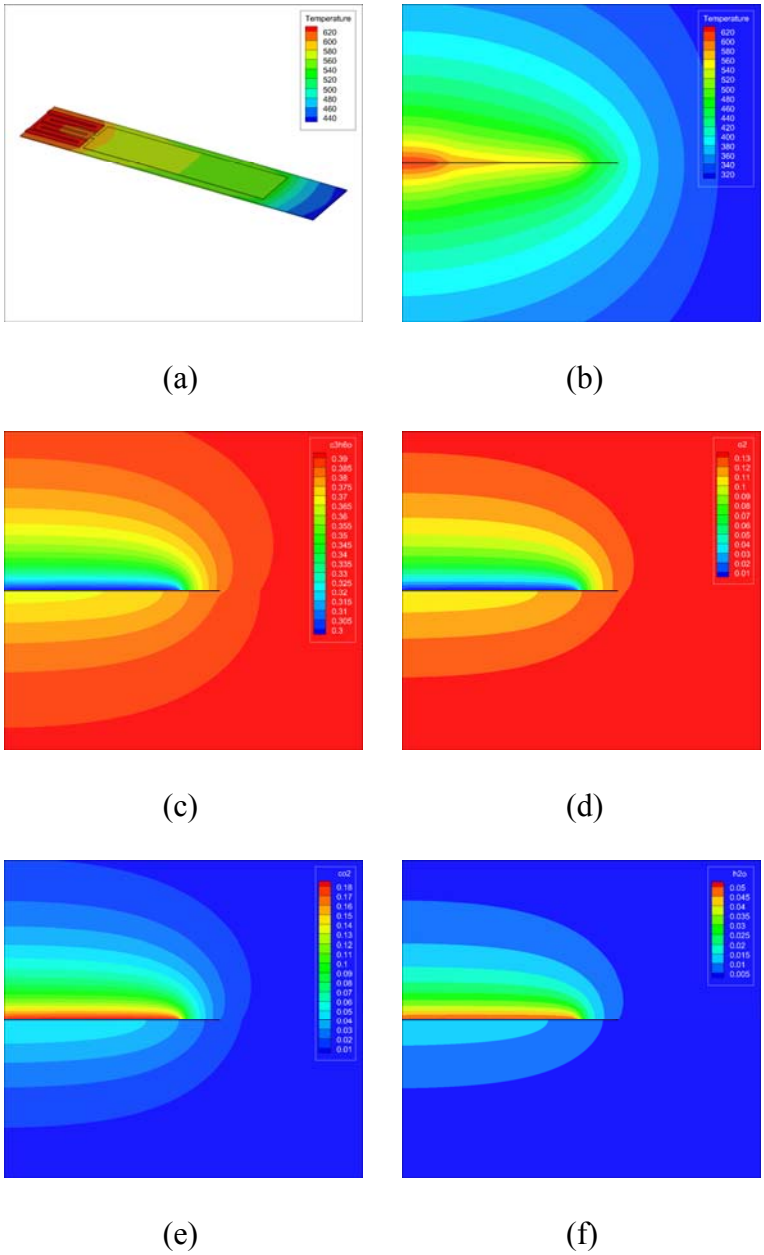

Fig. 66. (a) Simulation results for surface temperature profile; (b) Simulation results for temperature profile within the control volume; Species concentrations distribution for (c) Acetone (C_3H_6O) (d) Oxygen (O_2) (e) Carbon Dioxide (CO_2) (f) Water Vapor (H_2O); Actuation current = *18 mA*.

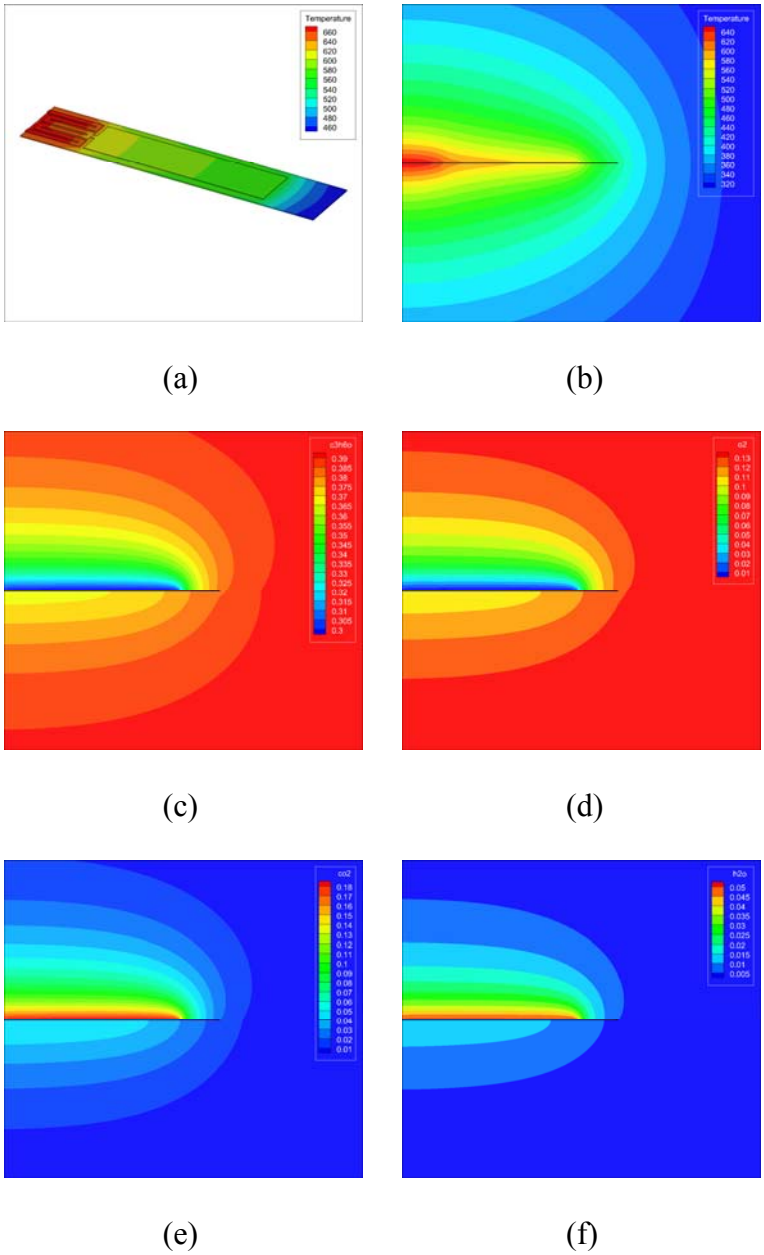

Fig. 67. (a) Simulation results for surface temperature profile; (b) Simulation results for temperature profile within the control volume; Species concentrations distribution for (c) Acetone (C_3H_6O) (d) Oxygen (O_2) (e) Carbon Dioxide (CO_2) (f) Water Vapor (H_2O); Actuation current = *20 mA*.

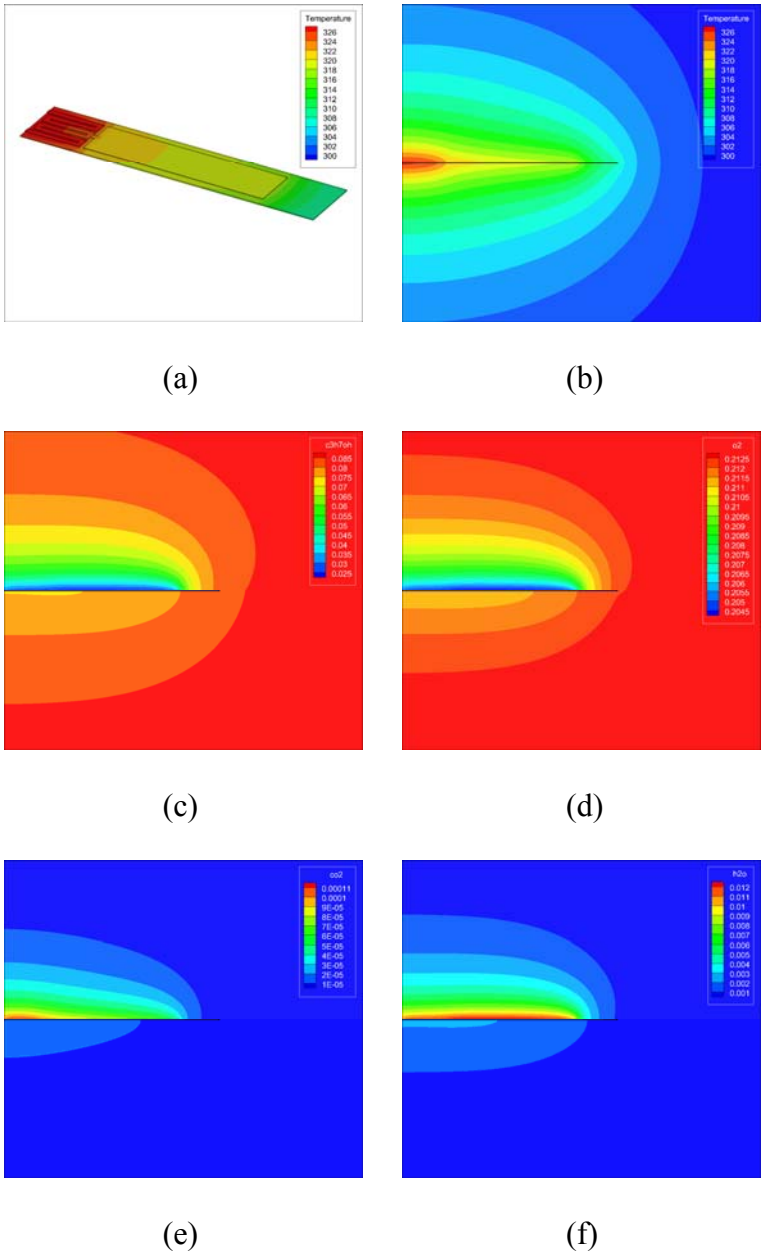

(a) (b)

(c) (d)

(e) (f)

Fig. 68. (a) Simulation results for surface temperature profile; (b) Simulation results for temperature profile within the control volume; Species concentrations distribution for (c) 2-Propanol (C_3H_8O) (d) Oxygen (O_2) (e) Carbon Dioxide (CO_2) (f) Water Vapor (H_2O); Actuation current = *6 mA*.

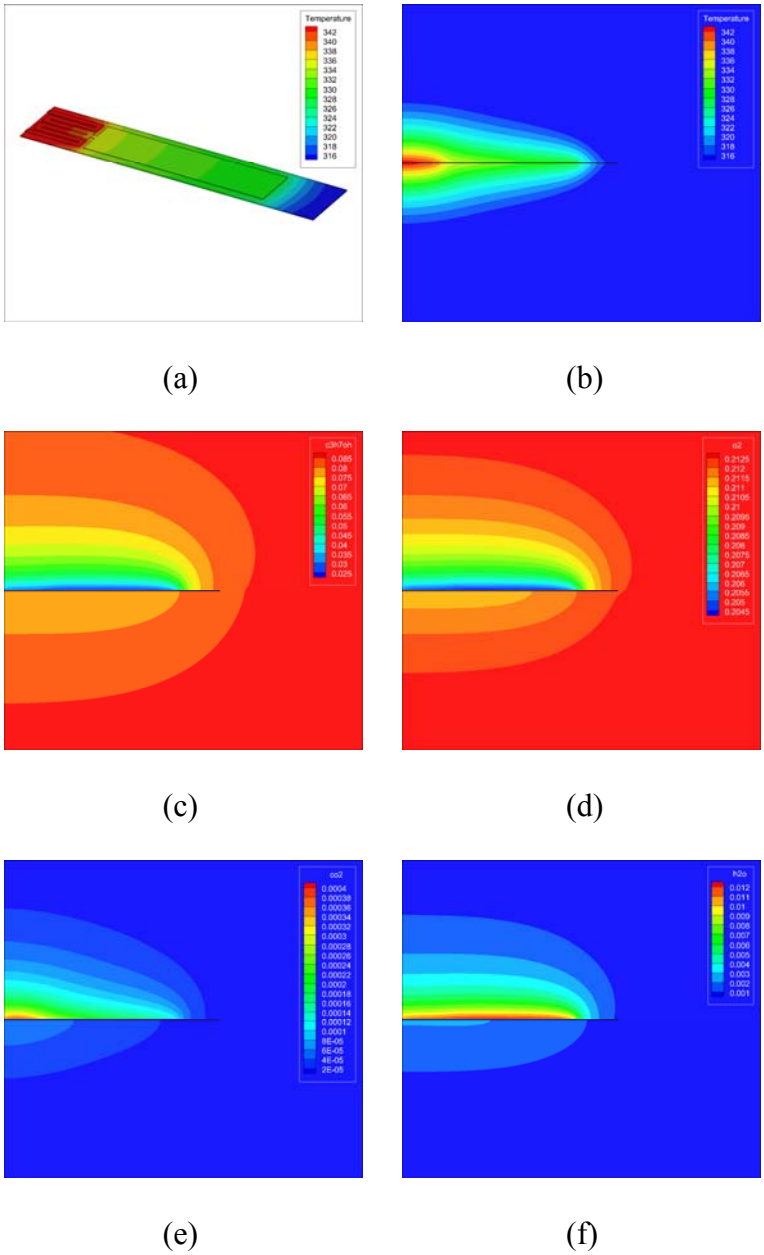

(a) (b)

(c) (d)

(e) (f)

Fig. 69. (a) Simulation results for surface temperature profile; (b) Simulation results for temperature profile within the control volume; Species concentrations distribution for (c) 2-Propanol (C_3H_8O) (d) Oxygen (O_2) (e) Carbon Dioxide (CO_2) (f) Water Vapor (H_2O); Actuation current = *8 mA*.

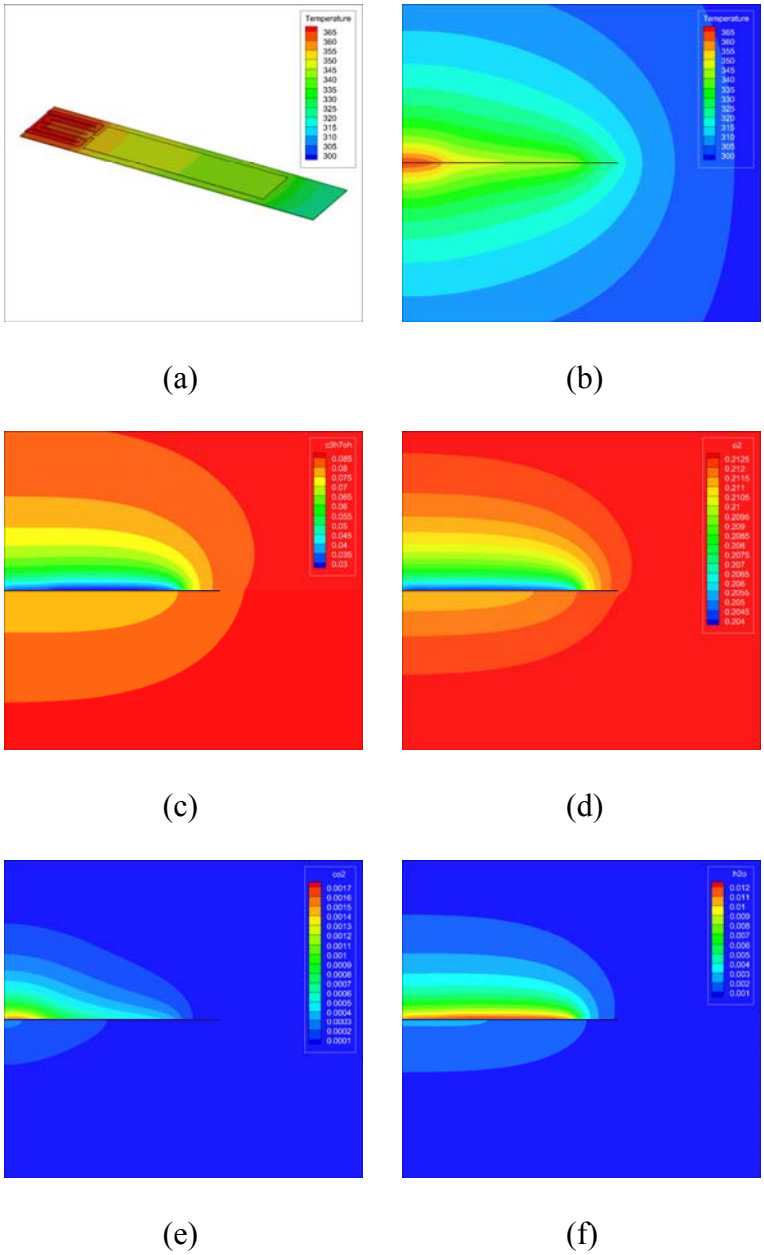

(a) (b)

(c) (d)

(e) (f)

Fig. 70. (a) Simulation results for surface temperature profile; (b) Simulation results for temperature profile within the control volume; Species concentrations distribution for (c) 2-Propanol (C_3H_8O) (d) Oxygen (O_2) (e) Carbon Dioxide (CO_2) (f) Water Vapor (H_2O); Actuation current = *10 mA*.

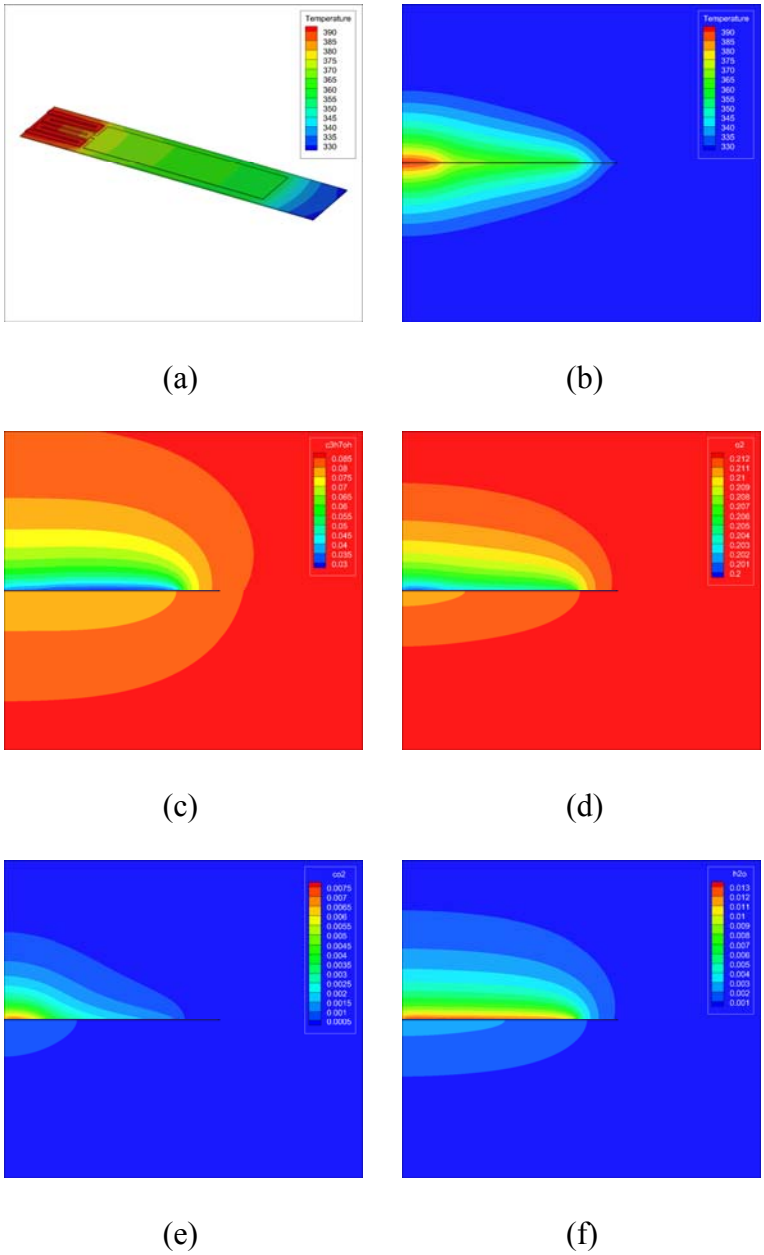

Fig. 71. (a) Simulation results for surface temperature profile; (b) Simulation results for temperature profile within the control volume; Species concentrations distribution for (c) 2-Propanol (C_3H_8O) (d) Oxygen (O_2) (e) Carbon Dioxide (CO_2) (f) Water Vapor (H_2O); Actuation current = *12 mA*.

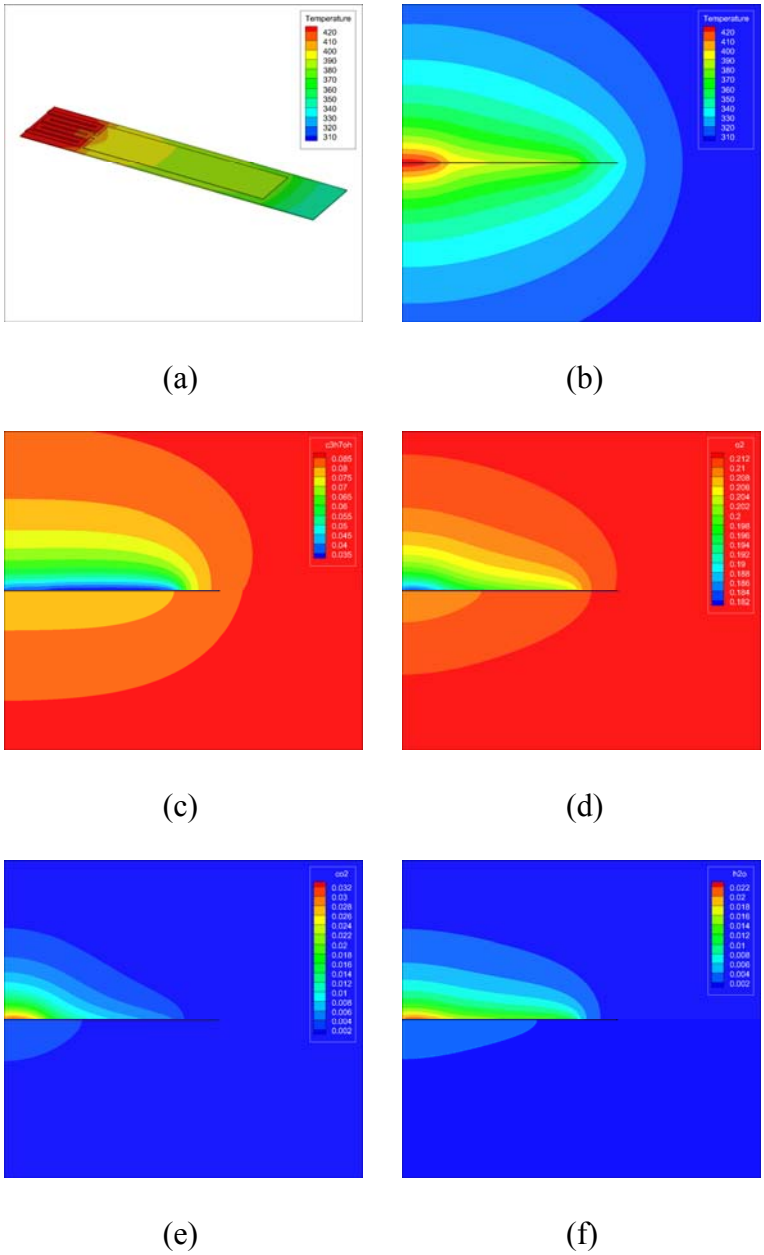

Fig. 72. (a) Simulation results for surface temperature profile; (b) Simulation results for temperature profile within the control volume; Species concentrations distribution for (c) 2-Propanol (C_3H_8O) (d) Oxygen (O_2) (e) Carbon Dioxide (CO_2) (f) Water Vapor (H_2O); Actuation current = *14 mA*.

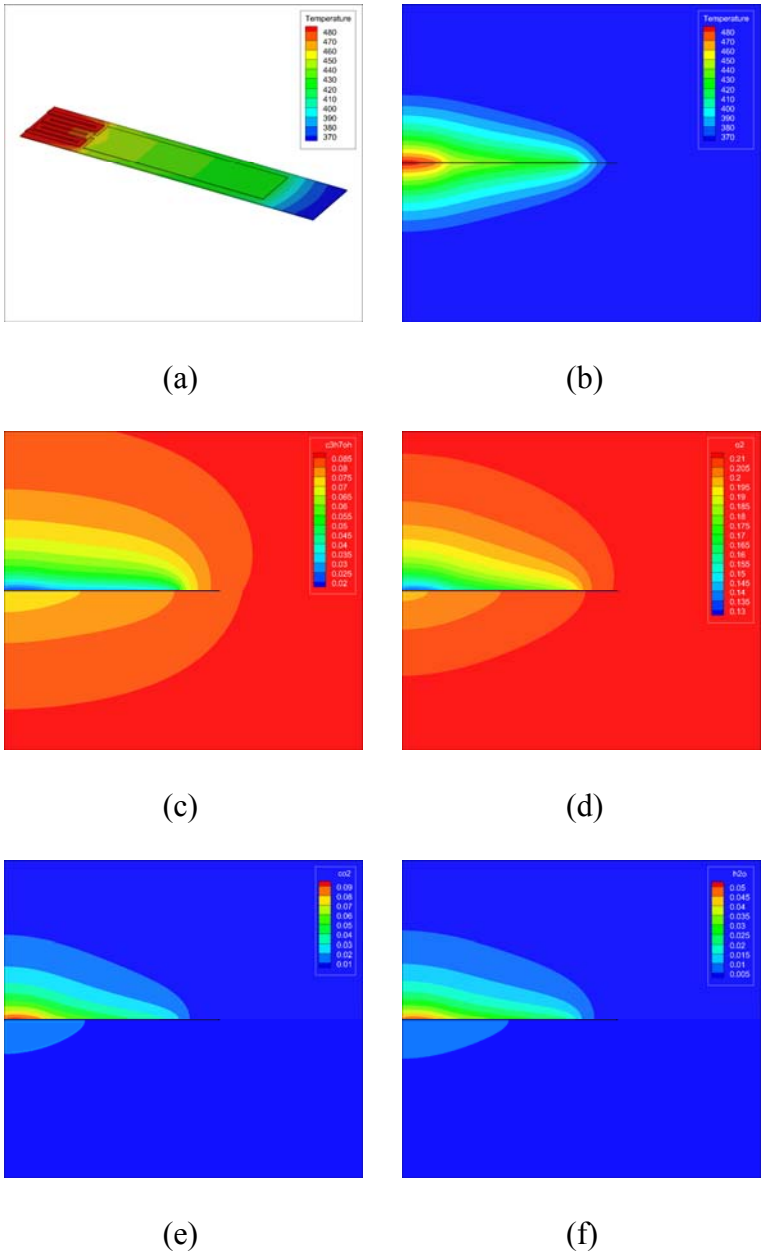

Fig. 73. (a) Simulation results for surface temperature profile; (b) Simulation results for temperature profile within the control volume; Species concentrations distribution for (c) 2-Propanol (C_3H_8O) (d) Oxygen (O_2) (e) Carbon Dioxide (CO_2) (f) Water Vapor (H_2O); Actuation current = *16 mA*.

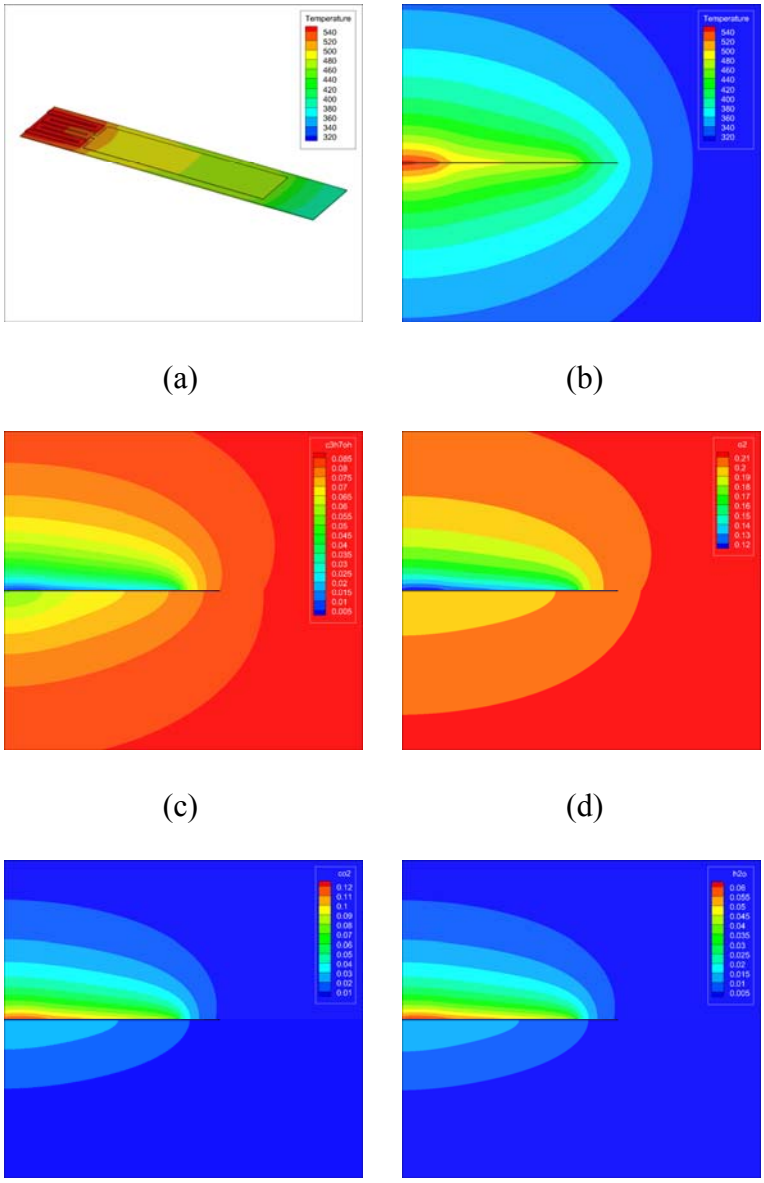

(a) (b)

(c) (d)

(e) (f)

Fig. 74. (a) Simulation results for surface temperature profile; (b) Simulation results for temperature profile within the control volume; Species concentrations distribution for (c) 2-Propanol (C_3H_8O) (d) Oxygen (O_2) (e) Carbon Dioxide (CO_2) (f) Water Vapor (H_2O); Actuation current = *18 mA*.

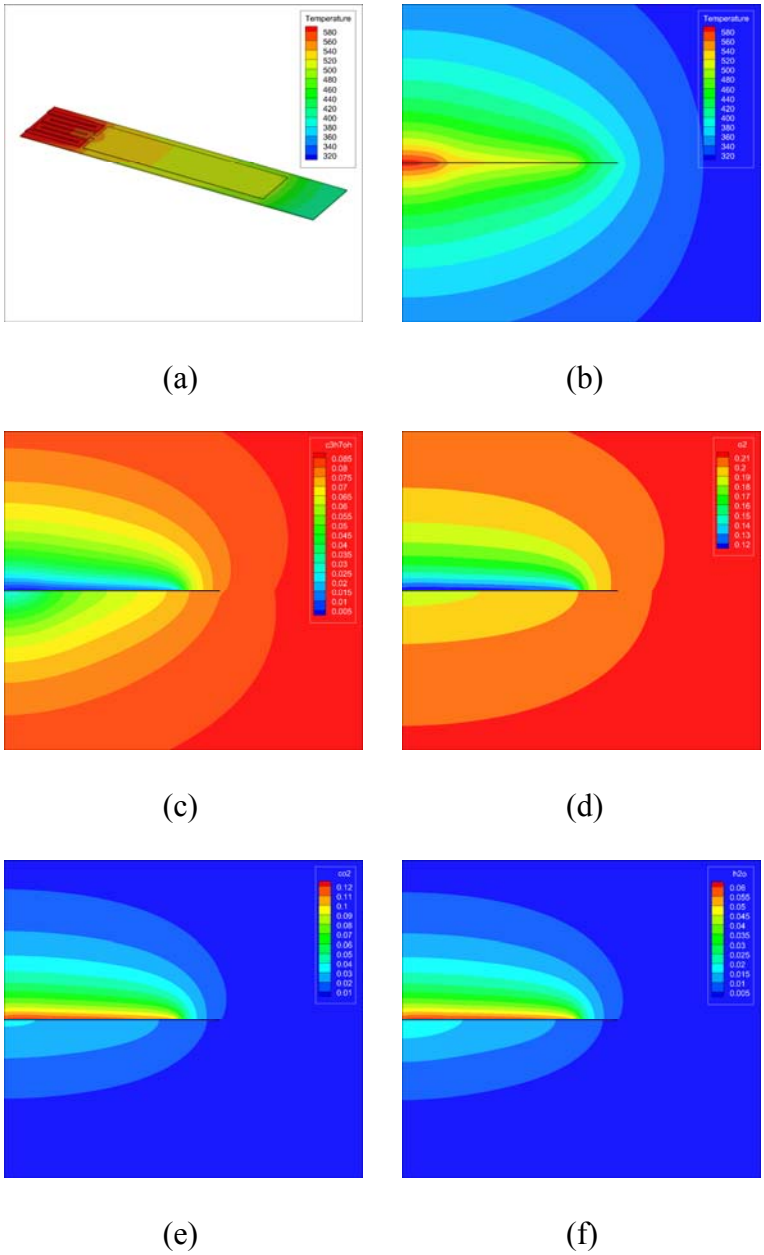

Fig. 75. (a) Simulation results for surface temperature profile; (b) Simulation results for temperature profile within the control volume; Species concentrations distribution for (c) 2-Propanol (C_3H_8O) (d) Oxygen (O_2) (e) Carbon Dioxide (CO_2) (f) Water Vapor (H_2O); Actuation current = *20 mA*.

APPENDIX C

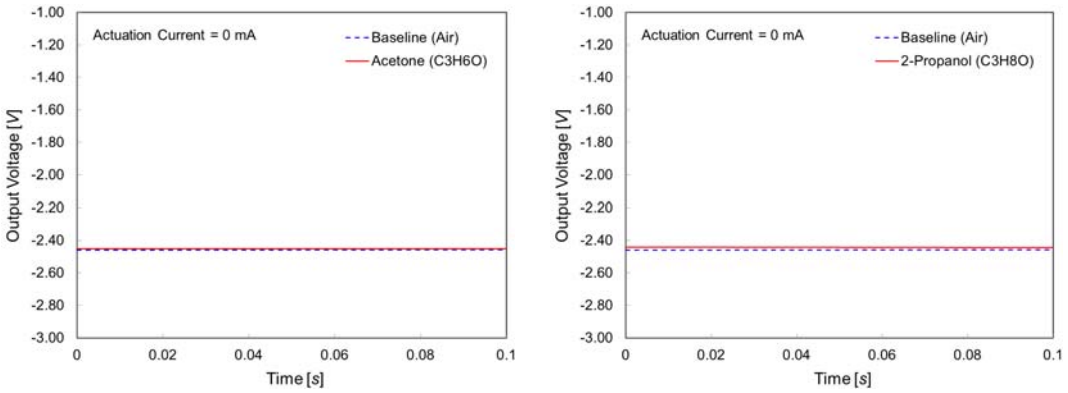

(a)

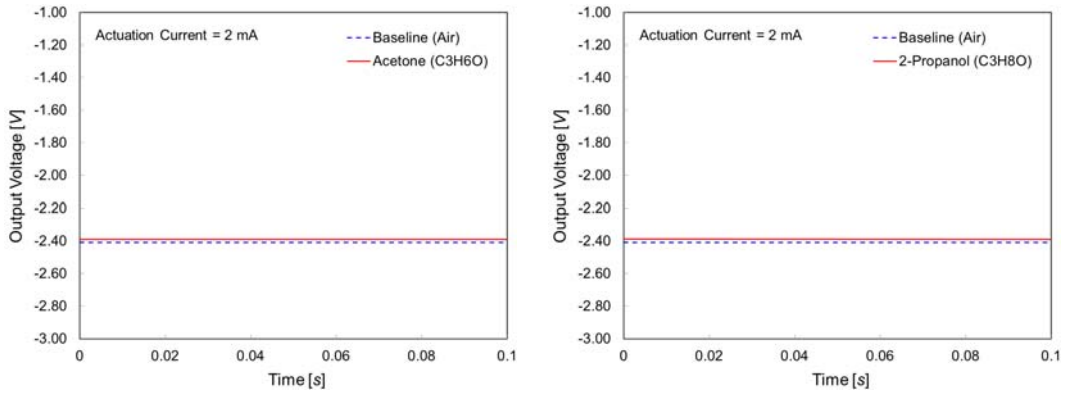

(b)

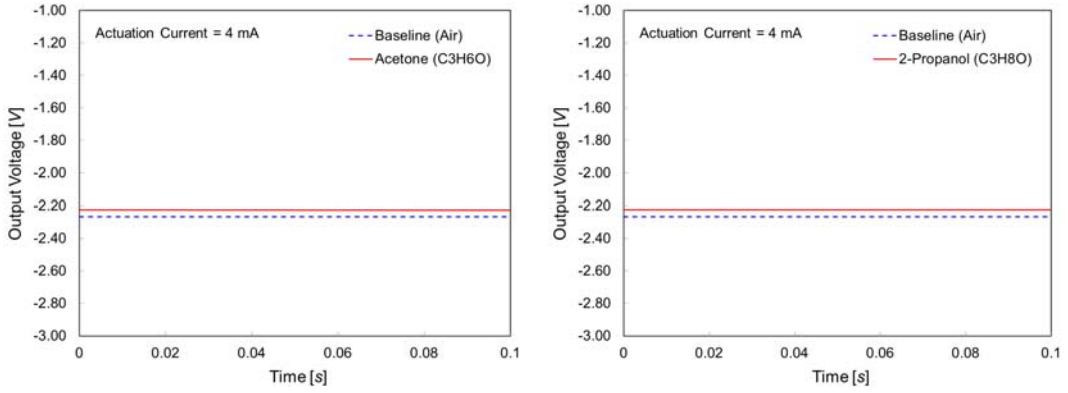

(c)

Fig. 76. Voltage values corresponding to the position of reflected laser spot varying with applied current values: (a) *0 mA* (b) *2 mA* (c) *4 mA* (d) *6 mA* (e) *8 mA* (f) *10mA* (g) *12 mA* (h) *14 mA* (i) *16 mA* (j) *18 mA* (k) *20 mA*.

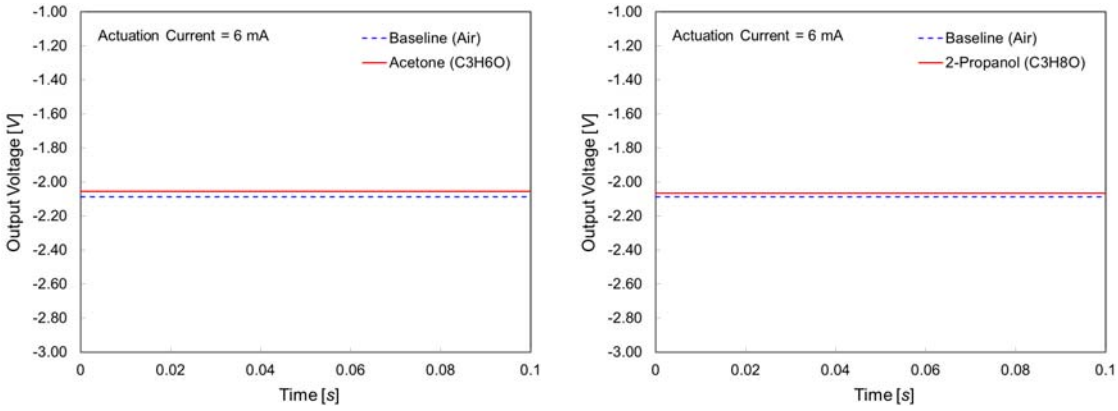

(d)

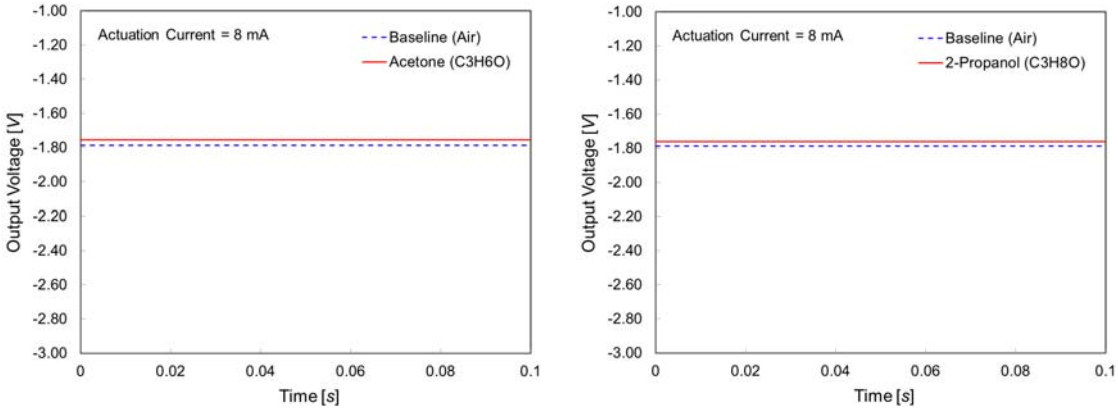

(e)

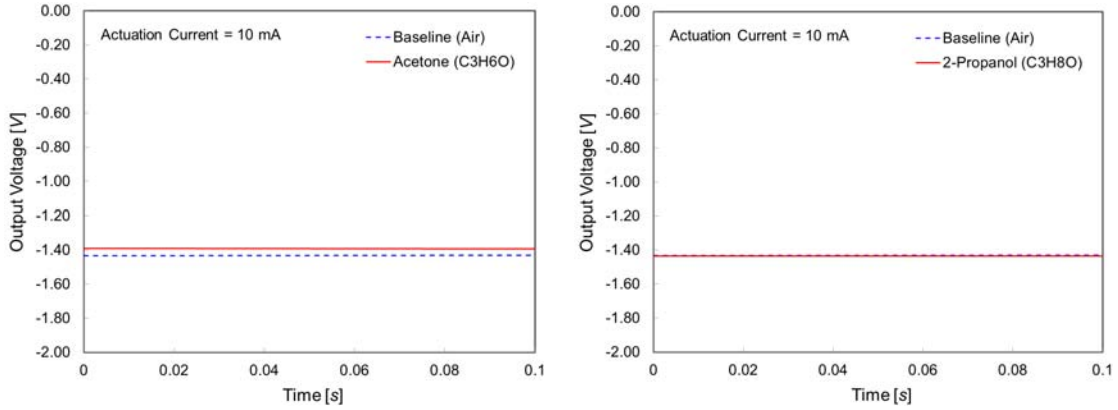

(f)

Fig. 76. Continued

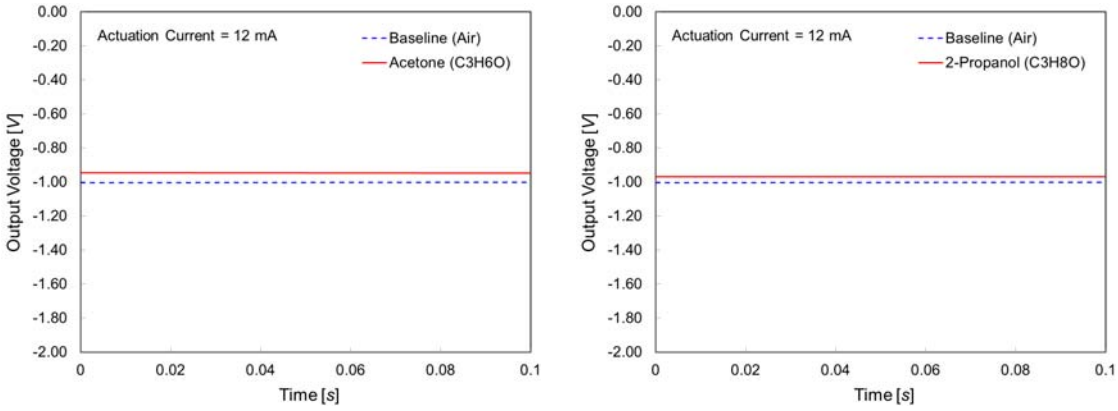

(g)

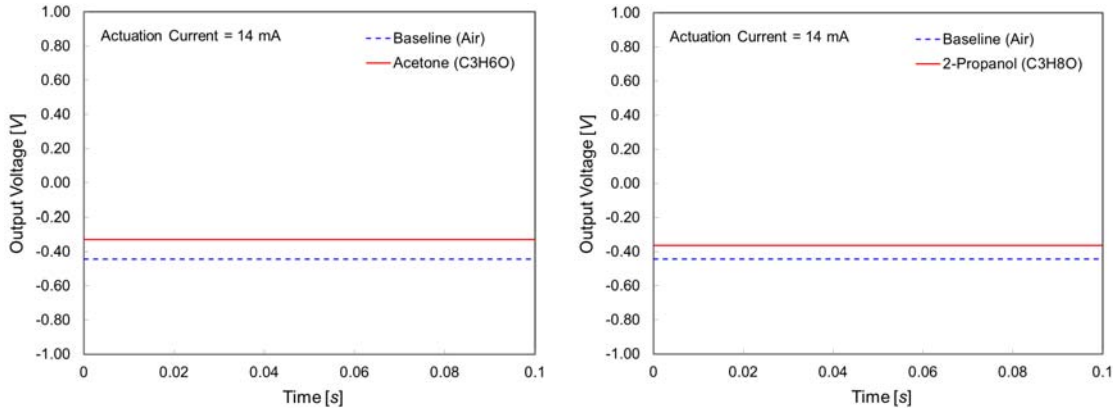

(h)

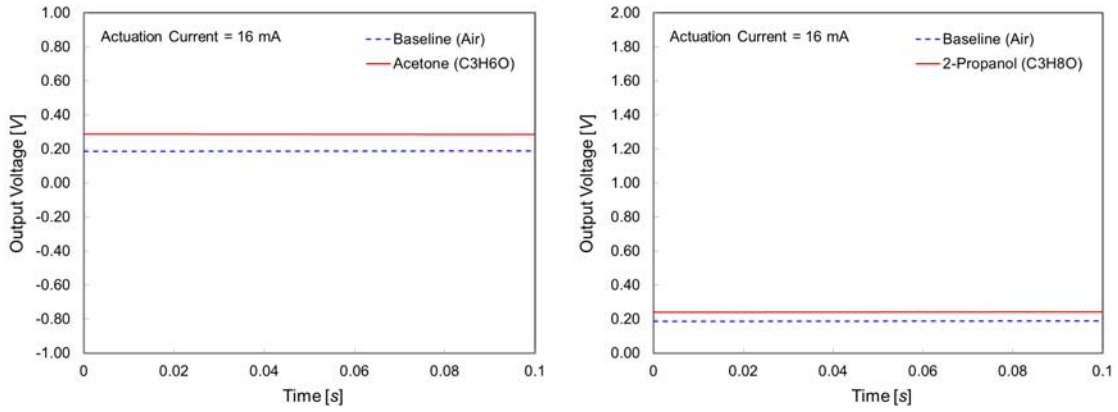

(i)

Fig. 76. Continued

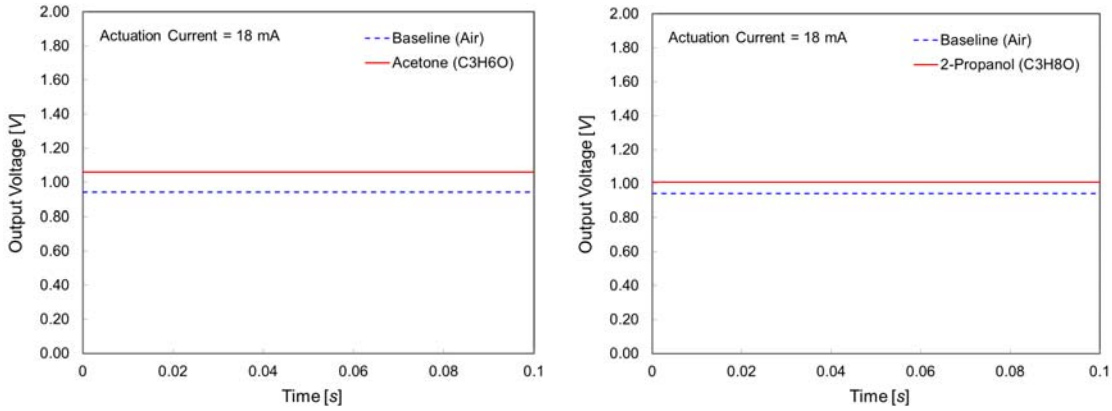

(j)

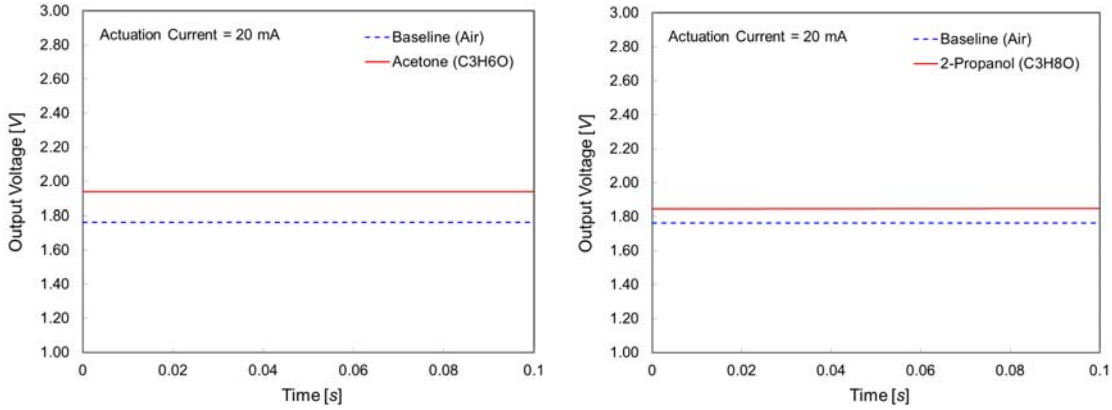

(k)

Fig. 76. Continued

APPENDIX D

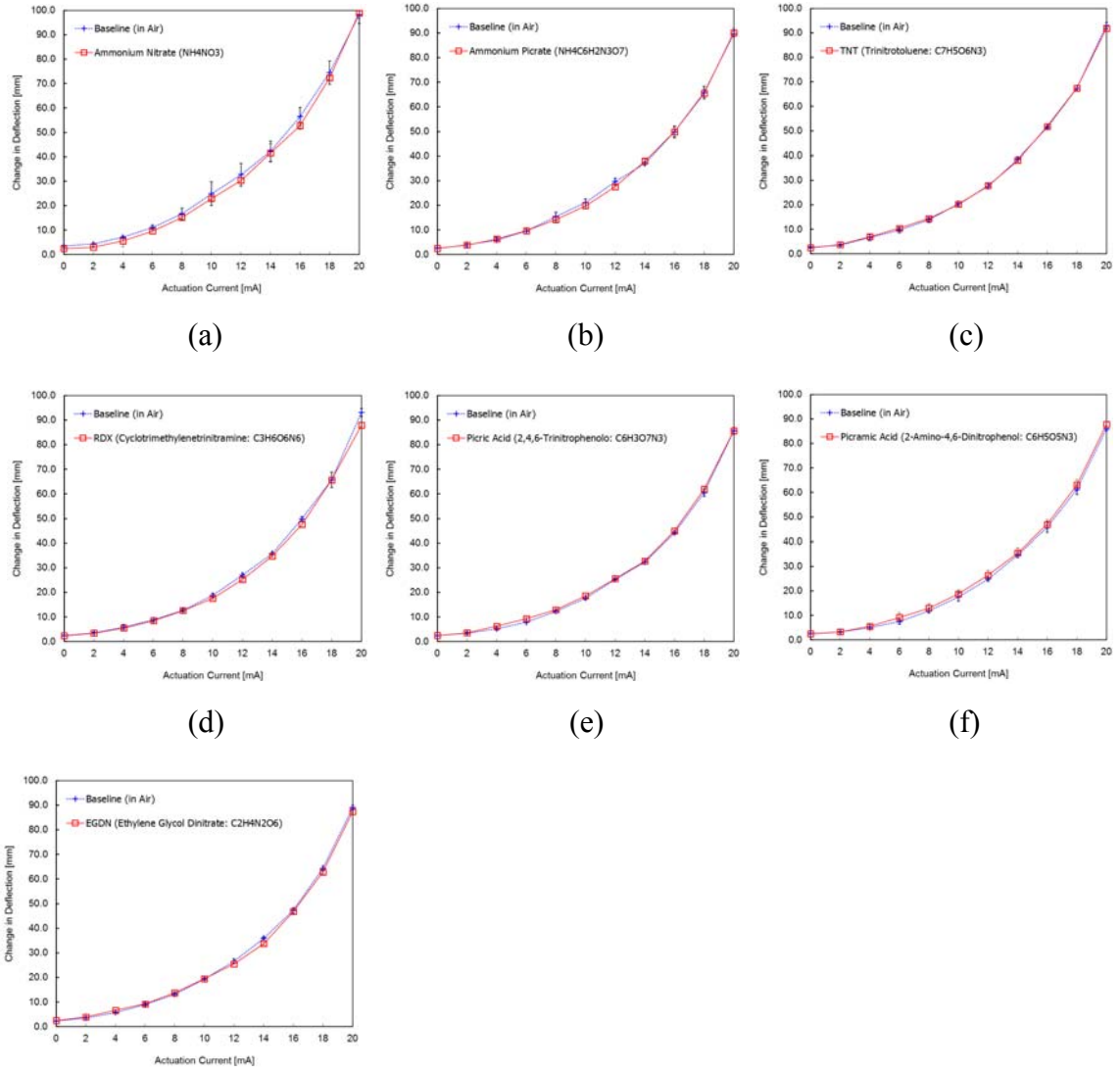

Fig. 77. Bending response of microcantilever to the solid explosives measured by the projection-screen method; (a) Ammonium Nitrate (b) Ammonium Picrate (c) TNT (d) RDX (e) Picric Acid (f) Picramic Acid (g) EGDN.

VITA

Name: Seokwon Kang

Address: Department of Mechanical Engineering
c/o Dr. Debjyoti Banerjee
Texas A&M University
College Station, TX 77843-3123

Email Address: seokwon.kang@gmail.com

Education: Ph.D., Mechanical Engineering,
Texas A&M University, College Station, May 2012

M.S., Mechanical Engineering (Division of Aerospace Engineering),
Korea Advanced Institute of Science and Technology, South Korea, Feb 2007

B.S., Mechanical Engineering (Minor: Electrical & Computer Eng.)
Hanyang University, South Korea, Feb 2005

Experience: CFD Engineer, Renault Samsung Motors, Jan 2007 – Jul 2008

Publications:

- Yu, J., **Kang, S.-W.**, Jeon, S., and Banerjee, D., "Heat Transfer Measurements for Flow of Nanofluids in Microchannels Using Temperature Nano-Sensors," *Frontiers in Heat and Mass Transfer* (Accepted for Publication, December 2011).
- De Los Santos, H.J., **Kang, S.-W.**, and Banerjee, D., 2011, "Lifshitz Localization-Based Reconfigurable Photonic Crystals," *Microwave and Optical Technology Letters*, **53**(12), pp. 2721-2724.
- **Kang, S.-W.** and Banerjee, D., 2011, "Modeling and Simulation of Capillary Microfluidic Networks based on Electrical Analogies," *ASME Journal of Fluids Engineering*, **133**(5), pp. 054502-1-6.
- **Kang, S.-W.** and Banerjee, D., 2011, "Point-Mass Model for Nano-Patterning Using Dip-Pen Nanolithography (DPN)," *Sensors & Transducers Journal*, **11**(Special Issue), pp. 64-73.
- **Kang, S.-W.**, Banerjee, D., Kaul, A.B., and Megerian, K.G., 2010, "Nanopatterning of Catalyst by Dip Pen Nanolithography (DPN) for Synthesis of Carbon Nanotubes (CNT)," *Scanning: The Journal of Scanning Probe Microscopies*, **31**(1), pp. 42-48.